Fall 12-15-2012

Interferometric Synthetic Aperture Sonar Signal Processing for Autonomous Underwater Vehicles Operating Shallow Water

Patricia E. Giardina
University of New Orleans, patricia.stiede@navy.mil

Interferometric Synthetic Aperture Sonar Signal Processing for Autonomous Underwater Vehicles Operating in Shallow Water

A Dissertation

Submitted to the Graduate Faculty of the
University of New Orleans
in partial fulfillment of the
requirements for the degree of

Doctor of Philosophy
in
Engineering and Applied Science
Underwater Acoustics

by

Patricia E. Giardina

B.S. Old Dominion University, 1995
M.S. University of Southern Mississippi, 2001
M.S. University of New Orleans, 2012

December, 2012

Dedication

To My daughter Jodi Ellen Stiede and My Son Kevin Scott Stiede for taking this long journey with me and for all the love, support, encouragement, and all the special moments along the way. The family torch has been passed to them to lead the way as I will in great delight watch as they create their own paths on their magical journey.

To My husband Kurt Alexander Giardina for the unconditional love and support and mostly his calming intellect that helps me see the right path clearly.

Acknowledgements

I wish to express my sincere appreciation and gratitude to my Dissertation Committee at the University of New Orleans, especially my dissertation advisor Dr. Juliette W. Ioup for having the patience and perseverance to guide me with her infinite wisdom on this enduring journey to obtain true knowledge of the natural universe. It is through her love and devotion to teaching science she imparts her knowledge that transcends the academic environment and permeates the mind body and soul so that one can attain an ethereal scholarly posture, and for this I am extremely grateful. I am extremely thankful to my co-chair Dr. Maria T. Kalcic for introducing me to the world of adaptive filter theory and the eloquent matrix inversion lemma. Dr. Stanley Chin-Bing who has nurtured my ability to unravel seemingly insurmountable physics and mathematics problems that I am indebted and grateful. I am thankful to Dr. George E. Ioup for encouraging me to pursue a higher academic posture, and I am thankful to Dr. Gregory Seab for encouraging me to keep going. A special thank you to Zella Huaracha for over a decade handled all the administrative work for my Masters and Doctoral degrees at the University of New Orleans.

I would especially like to thank Dr. Dan D. Sternlicht for mentoring me throughout this process, for giving my research direction, for bringing my research to the forefront, and for connecting me with international experts. It is through him I am now part of the international community in this very specialized field of Interferometric Synthetic Aperture Sonars (InSAS).

I would also like to thank Dr. Kerry Commander, at the Naval Surface Warfare Center (NSWC-PCD) for providing the funding and opportunity to continue my dissertation research. I would especially like to thank my colleague Dr. Gary Sammelmann who developed and provided the InSAS simulations for my research.

I am very fortunate to have the expert technical guidance of Dr. Christophe Sintes and Dr. Gerard Llort-Pujol from Telecom Bretagne in Brest France, whose interferometric research is the current state of the art. I am forever grateful to Dr. Christophe Sintes for his extraordinary efforts in assisting me with my dissertation. Mon cher ami Christophe, je vous remercie beaucoup!

Dr. Peter Gough from the University of Canterbury at Christchurch, New Zealand for sharing his unsurpassed knowledge of InSAS. He has provided me with the technical details and background knowledge necessary to conduct this research.

I will always hold a special place in my heart for the Naval Oceanographic Office (NAVO) for affording me the time, and opportunity to master the art of oceanography and hydrography, and for this I am grateful. It was my work at the Naval Oceanographic Office that inspired me to conduct research in InSAS. It was the friendships at NAVO that made it all worthwhile.

Most importantly I would like to thank my family. Especially my daughter Jodi and my son Kevin to whom I owe everything, they have been with me since my undergrad days and have seen me through to my doctoral days. It is their continuous love and support that made it possible. To my husband Kurt Giardina for his calming intellect and voice of reason that kept me on the right path.

Preface

Original copy
Software:
Microsoft Office Word 2007
Mathworks Matlab R2012a
PC SWAT Version 10 by Gary Sammelman

As synthetic aperture sonar (SAS) systems are transitioned into operational naval applications, there is developing interest in enhancing SAS designs with additional capabilities, including interferometric bottom height determination. Bathymetry, gathered in a single pass with SAS, has the potential to improve mine countermeasure efforts by adding constraints to object dimensions, assisting with seabed characterization, improving SAS imagery through enhanced motion compensation, and improving navigation through enhanced motion estimates found using displaced phase center methods. With the addition of one or two receiver elements, coarse bathymetric solutions can be derived, and with the addition of a second SAS array, full interferometric SAS surveying may be conducted, allowing fine scale seafloor bathymetry and improved resolution of mine-like targets.

While the interferometric technique is relatively mature within the synthetic aperture radar (SAR) community, the transition to sonar poses various technical issues which may require somewhat different approaches in the marine environment. Items of concern include approaches to data filtering and co-registration needed to resolve fine-scale height variations, the mitigation of errors due to sensor motion and medium variations, and the choice of phase unwrapping algorithms which are both effective and efficient for seafloor terrain typically mapped from altitudes of a few dozen meters. To address these topics, we will conduct comparative performance analyses for several interferometric processors using simulated SAS data, allowing direct quantitative comparisons between input depth values and bathymetric solutions. Improvements over existing inter-stave signal co-registration, filtering, phase unwrapping, and height estimation techniques for bathymetry mapping and small object shape identification will be the thrust of this research.

My goal is to present a summary of basic ocean physics to lay the foundation for Interferometric synthetic aperture sonar (InSAS) processing in the shallow water acoustic environment. Ocean acoustic models derived from the previously mentioned physics will be used to predict the acoustic response of the sonar in a large set of ocean environments. Beamforming signal processing techniques are presented to give a basic understanding of what is involved in converting the changes in ocean pressures at the sonar face into meaningful digital electronic data to form images of the ocean bottom. The details of standard practices for synthetic aperture sonar will be presented to build the framework for three dimensional bathymetric imaging. The thrust of this investigation will be to benchmark the methods of InSAS bathymetric height and phase unwrapping techniques. The eloquence of the Matrix Inversion Lemma, the Principle of Stationary Phase and the Principle of Orthogonality are revealed and their usefulness in signal processing is extremely valuable.

History

Synthetic aperture Sonar (SAS) technology originates from the Synthetic Aperture Radar (SAR) community. Walsh ’69 was awarded a patent on high resolution seafloor imaging, which was the beginning of SAS. Cutrona ’75 ported SAR technology to SAS. He pointed out that sensor motion and the ocean media would be limiting factors to SAS capabilities. Spiess & Anderson ’83 were awarded a patent on InSAS. Griffiths ‘94 proposed using three vertically spaced receivers for interferometric bathymetry. Hawkins ’96 and Gough ‘98 provide a historical review of the development of SAR and SAS technologies. Wen Xu ’98 developed a direction of arrival amplitude estimation for multiple row bathymetric side scans. Chatillon ’99 produced bathymetric voxels of $1m^3$ at 2.5 km. Lurton ’00 investigated the significant factors that influence the quality and resolution of swath bathymetry using phase differences. Pinto ’02 showed the motion compensation scheme of displaced phase center antenna is within the theoretical limits. Sintes ’02 presented the vernier method for resolution of phase ambiguities. Hayes ’04 provided a ten year review suggesting the future focus should be on motion estimations and compensation. Hansen ’06 applied coarse and fine motion compensation techniques and produced improved interferometric images and bathymetric height estimations. Hayes & Gough ’09 provide a peer review of the SAS technology and the current state of the art. Tang ’04 stated in the ’90’s China started developing beamforming algorithms that were not pixel based. They moved to range-Doppler, wavenumber and chirp scaling which was good for stop and hop but later went to Image formation algorithm of multi-aperture synthetic aperture sonar. They developed displaced phase center algorithms for motion compensation, modified the phase gradient algorithm (PGA) for stripmap mode and by the end of 2001 they had an operational InSAS system capable of .2 m resolution. Wei Xu ’94 developed phase unwrapping of SAR Interferograms using the vernier multi-frequency and multi-baseline methods. The current literature on InSAS bathymetric height reconstruction indicates that further research is required to obtain a vertical resolution consistent with along-track and across-track resolution.

Table of Contents

List of Figures

List of Symbols

A	area
α	specific gravity
α	attenuation
B	boric acid
B_w	bandwidth
B	grazing angle
b	baseline
C,c	sound speed 1500m/s
d	distance between hydrophones
Δ_{rx}	distance between receiver and transmitter
ξ	particle displacement
ee	received echo
F	force
ff	reflectivity of the scene
f	frequency
f_s	sample frequency
g_{mv}	aperture Vector
H,h	height
I	intensity
I_i	initial intensity
k	wavenumber
λ	wavelength
L	length of array
μ	viscosity
m,n	number of receivers
ρ	density
Ψ	phase angle
Φ	true phase
φ	phase
Π	power
P	pressure
P_0	reference pressure
R_0	reference range
R,r	range
R_{mn}	reflection coefficient
ρ	density
$\rho_{ambient}$	ambient density
σ	scattering function
ss	received signal
σ	backscatter cross section
σ	standard deviation
σ_a	backscatter attenuation
ς	tilt angle
θ	direction of arrival
t	time
τ	time delay
T_{mn}	transmission coefficient
u	along-track position
u	velocity vector
v_0	initial velocity
V_g	group velocity
V_p	phase velocity
W	filter Weight
ω	angular frequency
X	input vector
x_0	position on the seafloor
X	distance perpendicular to the array
y_0	position on the seafloor
y	distance along the array
Z,z	depth

Abstract

There are various processing techniques used with InSAS data to determine bathymetric heights. In this research new methods are tested using synthetic data and compared with existing methods. Improvements come from the use of Chirp-Scaling, a phase preserving beamforming technique to form a SAS image; an interferometric Vernier method to unwrap the phase; and confirming the direction of arrival with the MUltiple SIgnal Channel (MUSIC) estimation technique. The fusion of Chirp-Scaling, Vernier, and MUSIC affords stability in the bathymetric height measurement as well as improved resolution. The methods are computationally faster and use less memory than existing techniques.

Interferometry, Synthetic Aperture Sonar, Signal Processing, Bathymetry, Phase Unwrapping, Autonomous Underwater Vehicles

Introductory

Chapter 1 Physics of Underwater Acoustics

It is an introductory to the theory of an acoustic plane wave traveling through varying ocean mediums constrained by the boundaries of the pressure relief sea surface and the seafloor bottom with a particular emphasis on the phase. This is a brief introduction to lay the ground work for chapters three and four. My recommendation for detailed information on the subject is to read Clay & Medwin 1977, and Apel 1987.

Chapter 2 Vehicle Motion

This is an introductory to the current state of the art of motion estimation, motion compensation, and autofocusing used in SAS processing. Although motion compensation has a major effect on the image it is beyond the scope of this dissertation.

Chapter 3 Sonar Signal Processing

In this chapter I present several beamforming and adaptive beamforming techniques that will be used to produce a SAS image, reduce noise, find the direction of arrival, and eliminate multipath reflections. A fusion of these methods are combined to form a more precise image. This will be the subject of my follow on research.

Chapter4 InSAS and Phase Unwrapping, Bathymetric Height

This is the heart of the research, here the interferometric techniques is detailed with several methods to unwrap the phase. The true phase is then used to obtain the direction of arrival. The direction of arrival is then used to derive the bathymetric height.

Chapter 5 Research

Data analysis, error analysis, performance, and prediction analysis are presented to quantify the quality, and robustness of the InSAS algorithm. In this section I combine the methods of chirp-scaling, vernier interferometry, and MUSIC to produce a bathymetric image. This information has been removed and will appear in subsequent reports.

Chapter 6 Conclusion

This chapter is a summary of this research and describes the research moving forward.

Chapter 1 Physics of Sound

1.1 Plane Wave

A sound wave is a disturbance in the density of the medium caused by an impulsive force. The impulse causes the medium to condense causing peak pressure followed by rarefaction a minimum pressure. The peak pressure wave travels spherically outward. The Helmholtz equation relates the spatial dependence of the disturbance to the temporal dependence of the disturbance.

$$\{\nabla^2 + \frac{\omega^2}{c^2} - \frac{i\omega}{\rho c^2}[\mu\nabla^2 + B(\omega)]\}P(r)e^{-i\omega t} = 0 \qquad (1.1)$$

∇ is the spatial divergence, ω is the angular frequency, ρ is the density, c is the speed of sound $\left(c = \sqrt{\frac{\partial P}{\partial \rho}}\right)$, together ρc is the impedance, μ is the attenuation due to the molecular viscosity of water, B (ω) is the attenuation caused by ionic absorption, P is the amplitude of the sound pressure, and t is the time.

The advancing pressure wave will travel as longitudinal or transverse waves. Longitudinal waves known as compression waves travel parallel to the advancing wave front. Longitudinal waves exist in liquid mediums (ocean) and solid mediums (bottom sediments). Transverse waves also known as shear waves are orthogonal to longitudinal waves. Transverse waves only occur in solid mediums. Wave propagation transfers energy without transporting mass. If the advancing pressure wave front has constant frequency and phase it is considered to be a plane wave. The plane wave approximation expressed as pressure is a solution to Eq. (1.1).

$$P(r,t) = Pe^{i(\omega t - kR - \alpha R)} \qquad (1.2)$$

P is the amplitude of the sound pressure, ω is the angular frequency, t is the time, R is the range, k is the wavenumber $(k = \omega/c = 2\pi/\lambda)$ and α is the attenuation.

The acoustic intensity is the rate in which energy is transmitted in the direction of propagation per unit area of the wave front, also referred to as the energy flux. The average intensity is equal to the power passing through a unit area at a range R which is equal to

$$\langle I \rangle = P_0^2 \frac{R_0^2}{R^2 \rho c} \qquad (1.3)$$

Because the frequency of acoustic oscillation is so high there is no time in one cycle for the heat to flow and temperature to equilibrate, therefore the process is adiabatic. The group velocity is the speed at which the envelope

(amplitude) of the wave travels. The phase velocity is the speed at which the phase travels for a particular frequency. In a non-dispersive medium the phase and the group velocity are the same.

$$V_g = \frac{\partial \omega}{\partial k} \qquad V_p = \frac{\omega}{k} \tag{1.4}$$

V_g is the velocity of the group, ω is the angular frequency, k is the wavenumber, and V_p is the velocity of the phase.

1.2 Interference Patterns

This section covers the guiding principles of beamforming and interferometry, this is the crux of this dissertation and will be expounded upon in more detail in chapter three and chapter four. Interference patterns are used in beamforming multiple receiver arrays and provide information on the changing phase. They are extremely valuable in all aspects of underwater acoustics.

Huygen's principle explains that each point on a spherically advancing wave front acts as a new source of wavelets emanating in a spherical pattern. The envelope of all of these wavelets constitutes the new wave front resulting in longitudinal compression waves. The wavelets spread as if the wave fronts were formed from an equal but opposite source on the other side of the boundary [Clay & Medwin 1977].

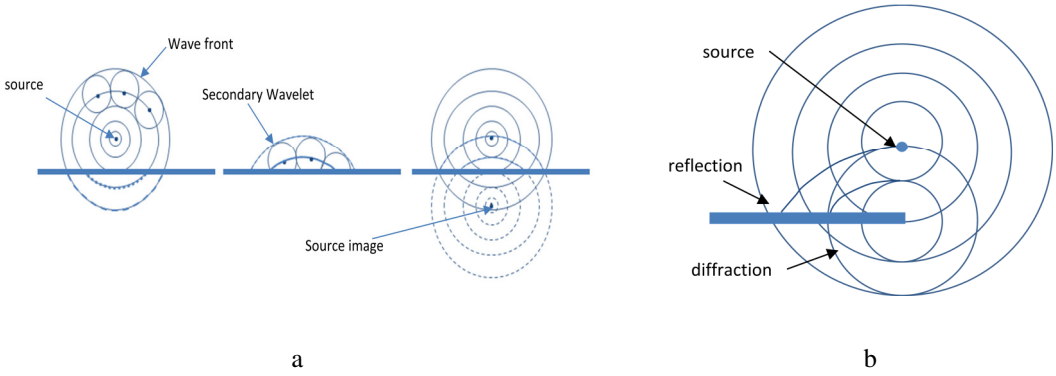

Figure 1.1 Huygen's Principle: (a) Wavelets at a reflecting surface showing the development of the secondary wavelets forming a new wave front. (b) Wavelets at an edge showing diffraction and reflection.

Similiarly, Lloyd's Mirror Effect is an interference of the direct path by a path that bounces off of a flat smooth surface. Reflected waves follow a direct path as if they originated at an imaginary source that is equidistant from the surface. The direct path and the reflected path coherently combine to form an interference pattern with deep nulls where destructive interference has occurred. The result is an asymmetric pattern of fringes where the phase at the mirror experiences a 180º shift resulting in a null at the center of the image.

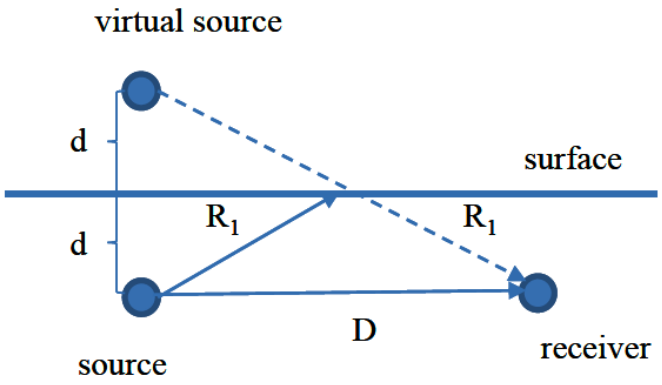

Figure 1.2 Lloyds Mirror Effect: *D* is the distance between the source and the receiver, *d* is the distance between the source and the reflecting surface, and R_1 is the slant range to the reflecting surface.

The distance between fringes is

$$x_n = \left(n - \frac{1}{2}\right)\lambda D/d \tag{1.5}$$

D is the distance between the source and the receiver, *d* is the distance between the source and the mirror (reflecting surface), and λ is the wavelength.

The interference pattern caused by multiple transmit or receive acoustic arrays can easily be extrapolated from the Young's double slit experiment were a light wave from a coherent source emanates spherically outward through a double slit causing the wave to interfere constructively or destructively creating an interference pattern.

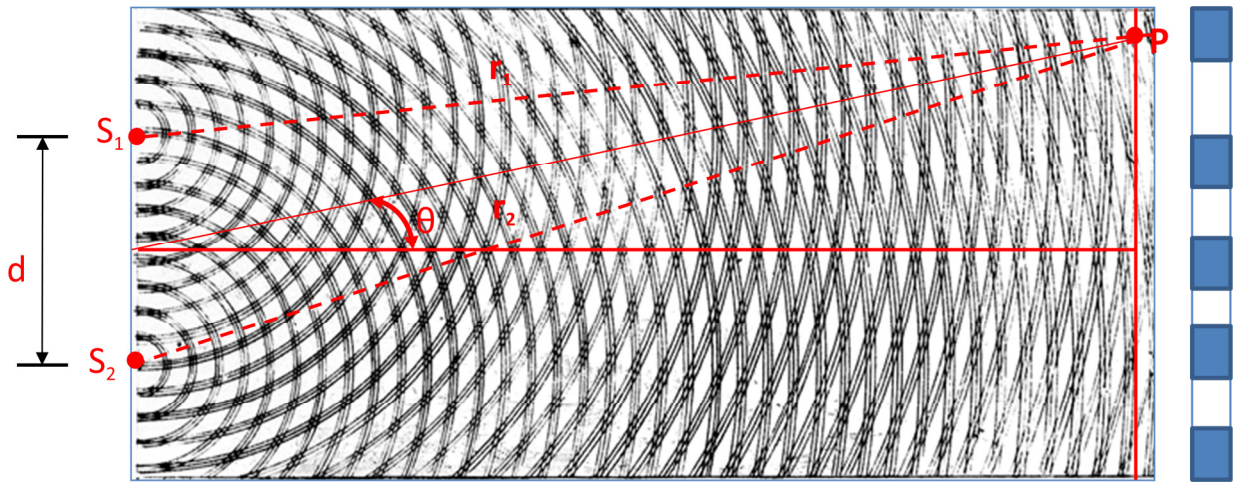

Figure 1.3 Young's double slit experiment showing the interference pattern and positions of maxima and minima light intensities (blue squares on the left represent maximum intensities). S_1 and S_2 are coherent sources of the wave, d is the distance between slits, r_1 and r_2 are the range from the source to the receiver, and P is the point of measurement.

The Interference pattern has a maximum amplitude when the phase difference between r_2 and r_1 are integer multiples of the wavelength and a minimum when the difference is a1/2 multiple of the wavelength.

maximum $$|r2 - r1| = n\lambda \quad (1.6)$$

minimum $$|r2 - r1| = (n + 1/2)\lambda \quad (1.7)$$

r_2 and r_1 are the ranges from their respective sources, n is the wavenumber, and λ is the wavelength.

The intensity pattern from the Young's double slit experiment results in a Sinc function, as will the beam pattern presented in chapter 3.

$$Sinc\ x = \frac{\sin(\pi x)}{(\pi x)} \quad (1.8)$$

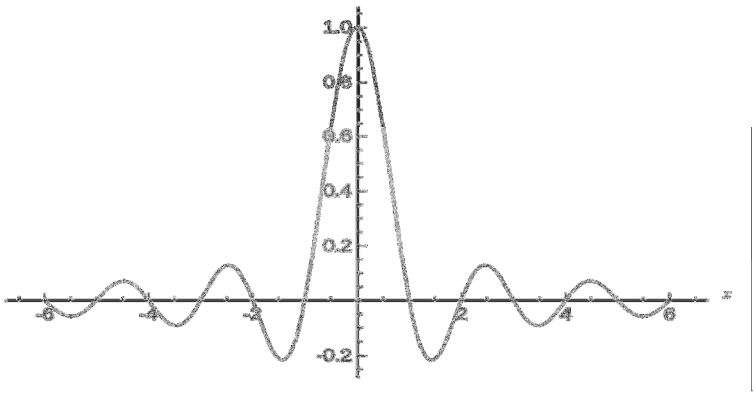

Figure 1.4 The Sinc function [Bracewell 2000]

The peaks in Figure 1.4 correspond to the maximum intensities in Eq. (1.6). The phase difference between the two sources often referred to as Bragg's Diffraction is

$$\Delta\Phi = \frac{2\pi d}{\lambda} sin\theta \tag{1.9}$$

d is the distance between slits, λ is the wavelength, and θ is the direction of arrival of the transmitted or received acoustic plane wave. This is only valid in a non-dispersive medium in which both group and phase velocities are the same. In chapter 4, the phase difference between two elements will be exploited to derive the bathymetric height of the seafloor and height of objects on the seafloor.

Fresnel diffraction is a near-field approximation to the Kirchhoff -Fresnel diffraction pattern for a circular aperture based on Huygen's principle. It explains how a plane wave diffracts causing the distant image to display a pattern of maximum and minimum intensities. Figure 1.5 shows the Fresnel zones, consider a point source at Q a height h from the seafloor producing spherically emanating zones of maximum and minimum intensities.

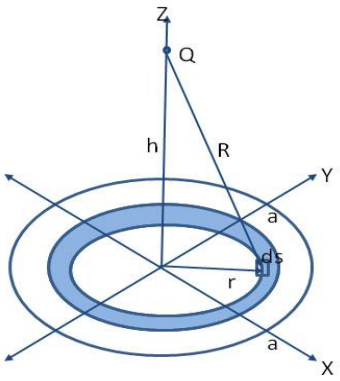

Figure 1.5 Fresnel diffraction: *Q* is the point source, *ds* is an area on the seafloor, *R* is the slant range, *h* is the height of the vehicle, and *r* is the horizontal range to the target.

The phase of a wave traveling from *Q* to *ds* and back to *Q* is

$$\Phi = \omega t - 2kR \tag{1.10}$$

ω is the angular frequency, *t* is time, *k* is the wavenumber, and 2*R* is the slant range there and back.

To obtain the change in phase from nadir *(r = 0)* to element *ds*, choose the spatial part of the reference phase to be *2kh* then the change in phase from nadir to element *ds* is

$$\Delta\Phi = 2kR - 2kh \tag{1.11}$$

k is the wavenumber, *R* is the slant range, *h* is the height of the source. Thus, the slant range *R* to the patch of seafloor *ds* is

$$R = \frac{\lambda\Delta\Phi}{4\pi} + h \tag{1.12}$$

Fresnel diffraction occurs in the near field when the Fresnel number is greater than 1

$$F = \frac{a^2}{R\lambda} \geq 1 \tag{1.13}$$

a is the characteristic size of the aperture, *R* is range, and λ is wavelength. Pythagorean's Theorem can then be used to obtain the horizontal range of the first Fresnel zone.

$$r^2 = \frac{h\lambda\Delta\Phi}{2\pi} + \left(\frac{\lambda\Delta\Phi}{4\pi}\right)^2 \tag{1.14}$$

Fraunhofer diffraction is the far-field approximation to Fresnel diffraction. It can be used, when the range is much greater than the wavelength r >> λ. Fraunhofer diffraction occurs when the Fresnel number is less than one.

$$F = \frac{a^2}{R\lambda} \ll 1 \tag{1.15}$$

a is the characteristic size of the aperture, *R* is range, and λ is wavelength. The approximation assumes the squared term $\left(\frac{\lambda\Delta\Phi}{4\pi}\right)^2$ in the Fresnel diffraction range Eq. (1.14) is negligible and the range is

$$r^2 \cong \frac{h\lambda\Delta\Phi}{2\pi} \tag{1.16}$$

Therefore, the approximation to the change in phase becomes

$$\Delta\Phi \cong \frac{2\pi r^2}{h\lambda} \tag{1.17}$$

The first phase zone: $0 \leq \Delta\Phi \leq \pi$, gives a positive contribution to the phase. The second phase zone: $\pi \leq \Delta\Phi \leq 2\pi$, gives a negative contribution to the phase. Subsequently, the nth phase zone: $n\pi \leq \Delta\Phi \leq (n+1)\pi$ and the change in phase for the n^{th} phase zone is

$$\Delta\Phi = n\pi \cong \frac{2\pi r_n^2}{h\lambda} \tag{1.18}$$

The range for the n^{th} phase zone is

$$r_n \cong \sqrt{\frac{h\lambda n}{2}} \tag{1.19}$$

1.3 Ocean Medium

Snell's law is used to describe the reflection and diffraction of the wave as it interacts at different boundaries (surface, sediment, fronts and eddies). Snell's Law states that the ratio of the sines of the angle of incidence and refraction at the boundary of two mediums are equivalent to the ratio of phase velocities in two different isotropic mediums.

$$\frac{\sin\theta_1}{c_1} = \frac{\sin\theta_2}{c_2} = n \tag{1.20}$$

θ_1 is the incident angle, θ_2 is the refracted angle in the new medium. c_1 is the phase speed in the first medium, c_2 is the phase speeds in the second medium, n is the index of refraction. The impedance at the boundary is the ratio of the pressure to the velocity or equivocally the density times the speed of sound. Due to the continuity equation the pressure and velocity at the interface must be equal.

Attenuation is the loss of acoustic energy per unit path length due to both absorption and scattering. The Stokes-Kirchhoff classical theory of attenuation attributed propagation losses to the thermal conductivity and the viscosity of the medium. The thermal conductivity loss for water turns out to be negligible. The significant losses in water are caused by shear viscosity and bulk viscosity. Shear viscosity is due to frictional forces during relative motion between adjacent layers of the liquid. The bulk viscosity is due to the molecular rearrangements that take place during a sound wave cycle. It is even more important than the shear viscosity in water [Clay & Medwin1977]. Attenuation is dependent on frequency, temperature, salinity, pressure and pH. In order of increasing frequency the major contributors of attenuation $\alpha(\omega)$ are: volume scattering by inhomogeneities, boric acid, magnesium sulfate and molecular viscosity [Apel 1987] . The change in average intensity due to the attenuation is

$$\langle I_{(r)} \rangle = I_0 \left(\frac{R}{R_0}\right)^2 e^{-\alpha(R-R_0)} \tag{1.21}$$

I_0 is the reference intensity, R_0 is the reference range, R is the range from the source to the receiver, and α is the total attenuation. The change in pressure due to the attenuation is

$$\langle P_{(r)} \rangle = P_0 \left(\frac{R_0}{R}\right)^2 e^{-\alpha(R-R_0)} \tag{1.22}$$

P_0 is the reference Pressure at reference range R_0, R is the range from the source to the receiver, and α is the total attenuation.

1.4 Reflection & Transmission

Boundary conditions occur in the ocean when there is a change in impedance ρc of the medium. This occurs in the water column, in the vertical due to the change in temperature, salinity, pressure, and in the horizontal caused by fronts, eddies and internal waves. Boundary conditions also occur at the surface where the pressure is equal to zero and the bottom which is dependent on the sediment characteristics.

1. At the boundary interface pressure is equal on both sides due to conservation of mass. The pressure incident P_i plus the pressure reflected P_r is equal to the total pressure transmitted P_t.

$$P_i + P_r = P_t \tag{1.23}$$

2. At the boundary interface the normal component of particle velocity is equal on both sides due to conservation of momentum. The particle velocity incident u_i plus the particle velocity reflected u_r is equal to the total particle velocity transmitted u_t. θ_i is the direction of incident plane wave, θ_r is the direction of reflected plane wave, and θ_t is the direction of the transmitted plane wave into the next medium.

$$u_i \cos\theta_i + u_r \cos\theta_r = u_t \cos\theta_t \tag{1.24}$$

3. The relationship between pressure and particle velocity is

$$P_i = \rho_1 c_1 u_i \cos\theta_i \tag{1.25}$$

$$P_r = \rho_1 c_1 u_r \cos\theta_r \tag{1.26}$$

$$P_t = \rho_2 c_2 u_t \cos\theta_t \tag{1.27}$$

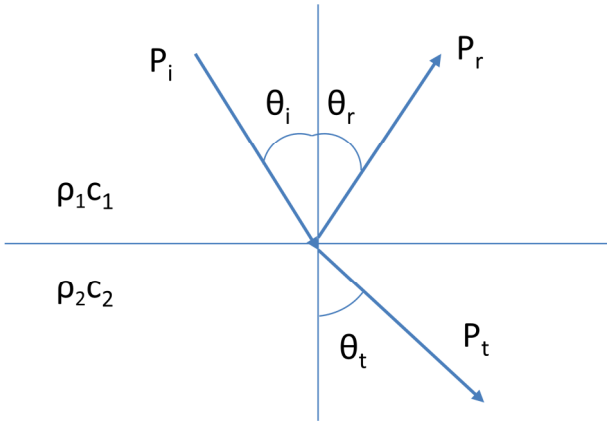

Figure 1.6 Reflection and transmission at a boundary: P_i is the incident pressure, θ_i is the direction of incident, P_r is the reflected pressure, θ_r is the direction of reflection, ρ_1 is the density of the first medium, c_1 is the speed in the first medium, ρ_2 is the density of the second medium, c_2 is the speed in the second medium, P_t is the transmission pressure, θ_t is the direction of transmission.

The pressure reflection coefficient is

$$R_{12} = \frac{P_r}{P_i} = \frac{\rho_2 c_2 \cos\theta_i - \rho_1 c_1 \cos\theta_t}{\rho_2 c_2 \cos\theta_i + \rho_1 c_1 \cos\theta_t} \tag{1.28}$$

The pressure transmission coefficient is

$$T_{12} = \frac{P_2}{P_1} = \frac{2\rho_2 c_2 \cos\theta_i}{\rho_2 c_2 \cos\theta_i + \rho_1 c_1 \cos\theta_t} \tag{1.29}$$

Recalling Snell's Law

$$\frac{\sin\theta_i}{c_1} = \frac{\sin\theta_t}{c_2} \tag{1.30}$$

The angle the plane wave is transmitted into the next medium is

$$\theta_t = \sin^{-1}\left(\frac{c_2}{c_1}\sin\theta_i\right) \tag{1.31}$$

The critical angle occurs when the transmitted angle ($\theta_t = 90°$) creating an evanescent wave that travels parallel to the boundary loosing energy exponentially in both mediums.

$$\sin\theta_c = \frac{c_1}{c_2} \tag{1.32}$$

Below the critical angle $(c_2 < c_1)$, $(c_2/c_1 \sin\theta_i < 1)$ for all angles of incidence, in the case for a hard bottom where $(c_2 >> c_1)$ the total incident wave is internally reflected. Above the critical angle the reflection coefficient is

$$R_{12} = \frac{\rho_2 c_2 \cos\theta_i + i\rho_1 c_1 \sqrt{\left(\frac{c_2}{c_1}\right)^2 \sin^2\theta_i - 1}}{\rho_2 c_2 \cos\theta_i - i\rho_1 c_1 \sqrt{\left(\frac{c_2}{c_1}\right)^2 \sin^2\theta_i - 1}} \tag{1.33}$$

The beauty of this lies in the fact that the denominator is the complex conjugate of the numerator, therefore the absolute square of the reflection coefficient is one, and therefore total reflection occurs, and the signal has a phase lag of $e^{i2\Phi}$ [Clay & Medwin 1977].

$$\tan\Phi = \frac{\rho_1 c_1 \sqrt{\left(\frac{c_2}{c_1}\right)^2 \sin^2\theta_i - 1}}{\rho_2 c_2 \cos\theta_i} \tag{1.34}$$

Scattering is the random incoherent reflection of the acoustic plane wave. As the surface becomes rougher the energy will be scattered and become more random. There are many methods for handling the reflections caused by the roughness of two surfaces. Two significant methods are the Rayleigh's formula for a plane wave scattering on a sinusoidal surface and the Helmholtz- Kirchhoff (H-K) integral which is a mathematical description of Huygen's principle. H-K is derived from Green's theorem which subsequently is derived from Gauss's theorem (see appendix 1 for details). The H-K integral field at point Q

$$U(Q) = \frac{1}{4\pi}\int_s U_1 \frac{\partial}{\partial n}\frac{e^{-ikR}}{R} - \frac{e^{-ikR}}{R}\frac{\partial U_1}{\partial n}\,ds \tag{1.35}$$

U_1 is the field at point Q, n is normal to the surface, k is wavenumber and R is the range. Figure 1.7 is a closer look at point Q.

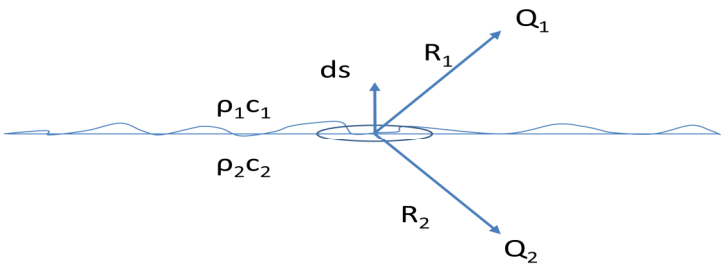

Figure 1.7 Small area on the H-K surface. ρ_1 is the density of the exterior medium, c_1 is the speed in the exterior medium, ρ_2 is the density of the interior medium, c_2 is the speed in the interior medium, R_1 is the range to point Q_1, and R_2 is the range to point Q_2.

The pressure is related to the greens function as follows

$$P_1 = U_1(Q)P_0R_0e^{-i\omega t} \tag{1.36}$$

$$P_2 = U_2(Q_2)P_0R_0e^{-i\omega t} \tag{1.37}$$

U_1 is the reflection wave field of the incident wave, U_2 is the transmitted wave field, P_0 is the reference pressure at range R_0, ω is the angular frequency, and t is time.

Kirchhoff Approximation states if the reflection coefficient and the transmission coefficient are slowly varying then they can be removed from the integral.

$$U_1(Q) \cong \frac{R_{12}}{4\pi}\int_s \frac{\partial}{\partial n}\left(U_s\frac{e^{-ikR}}{R}\right)ds \tag{1.38}$$

$$U_2(Q) = \frac{T_{12}}{4\pi}\int_s \left[U_s\frac{\partial}{\partial n}\frac{e^{-ik_2R_2}}{R_2} - \frac{e^{-ik_2R_2}}{R_2}\frac{\partial U_s}{\partial n}\right]ds \tag{1.39}$$

This is a very good estimate of primary scattering. A more detailed approach would be necessary for secondary scattering.

Eckart's procedure is used to determine the average reflection coefficients for a randomly rough surface. Echkart's procedure is dependent on the: RMS roughness σ of the surface, Probability Distribution Function (PDF) for the change in depth, and spatial correlation function of the surface heights.

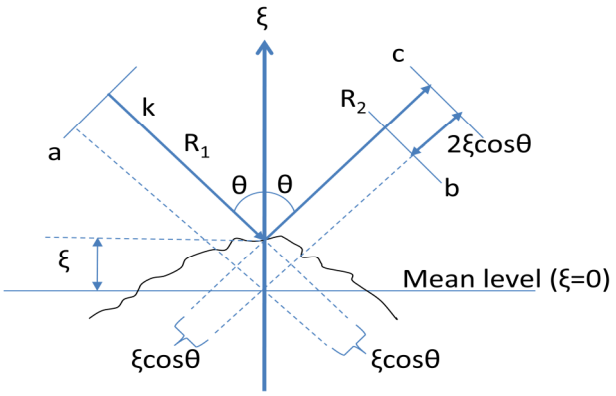

Figure 1.8 Eckart's procedure for a randomly rough local surface. a is the position of the source, k is the wavenumber, R_1 is the distance from the source to a point on the seafloor and R_2 is the distance from the point to the receiver, ξ is the mean bottom level, and θ is the direction of arrival.

The scattering coefficient is

$$S(\theta_1, \phi_1, \theta_2, \phi_2, f) = \frac{\int_{T_2} P^2 \, dt}{R_0^2 \int_{T_1} P_0^2 \, dt} \frac{R^2 \cos\theta}{\pi \Delta x \Delta \varphi} \tag{1.40}$$

The backscatter cross section is the scattering function times the area.

$$\sigma_{bs} = SA = \frac{I_{bs} R^2}{I_i} = \left(\frac{P_{bs}}{P_i}\right)^2 R^2 \tag{1.41}$$

I_i is the inicident intensity, S is the scattering function, A is the ensonified area, together SA form the backscattered cross section, and R is the range. The target strength is the backscattered cross section divided by the area.

$$TS = 10\log\left(\frac{\sigma_{bs}}{A}\right) = 10\log\left(\frac{P_{bs}}{P_i}\right)^2 \frac{R^4}{R_1^2 R_0^2} \frac{\sigma_{bs}}{A} \tag{1.42}$$

Scattering parameters are exploited further to determine the materials objects are made of. It is a very important parameter in automatic recognition algorithms. In this chapter I covered the acoustic plane wave, interference patterns, boundary conditions, reflection, transmission, scattering and their effects on phase.

Chapter 2 Moving Vehicle

2.1 Industry Standards

The purpose of this chapter is to present an introductory to the current state of the art for motion compensation, motion estimation and autofocus. It is essential to understand the motion of the vehicle and transfer the information into the processing of the bathymetric image. Figure 2.1 is a flowchart for bathymetric reconstruction.

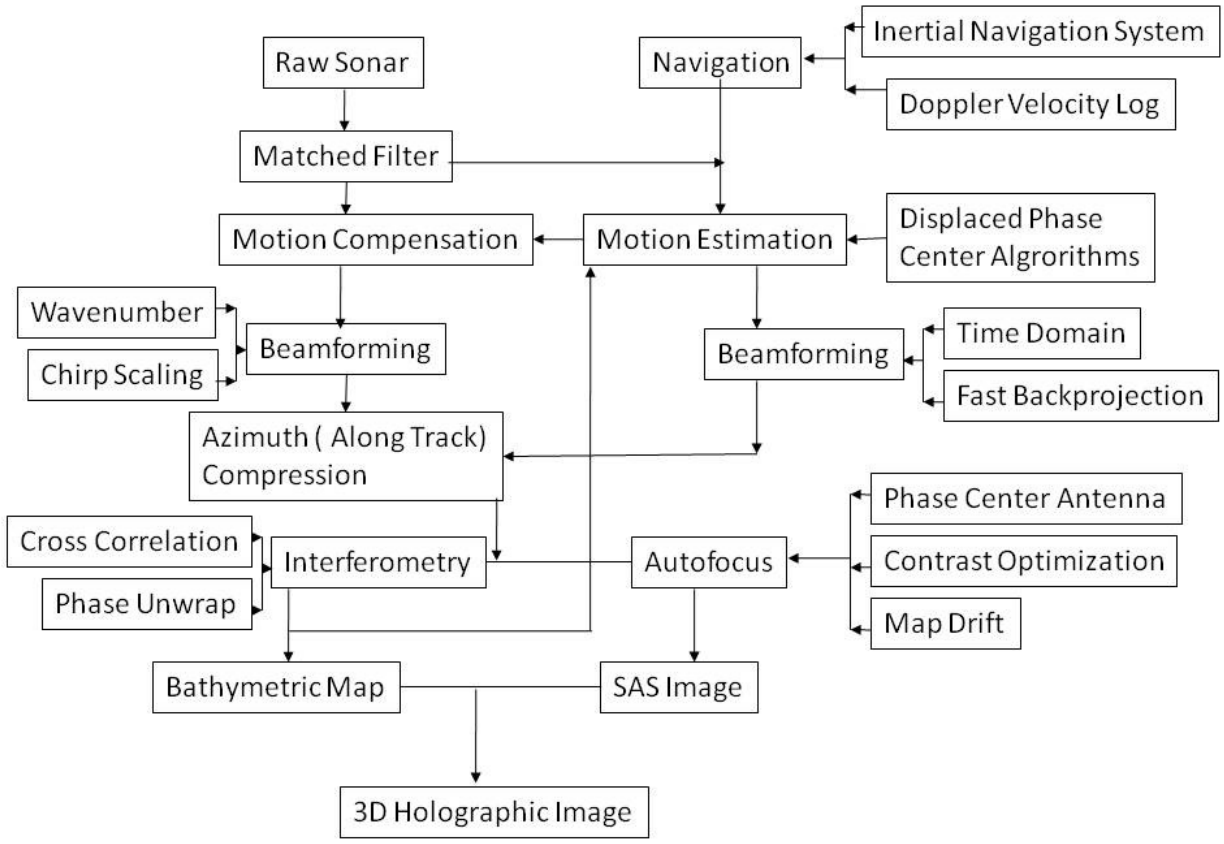

Figure 2.1 InSAS three dimensional bathymetric reconstruction flowchart [Hansen et al. 2003].

2.2 Motion Estimation

One of the biggest challenges working with a moving platform is to stabilize the motion and precisely calculate its position. An underwater vehicle is subjected to currents, tides, and waves. It has six degrees of freedom: three rotations (roll, pitch, and yaw), and three displacements (surge, sway, and heave), as shown in Figure 2.2.

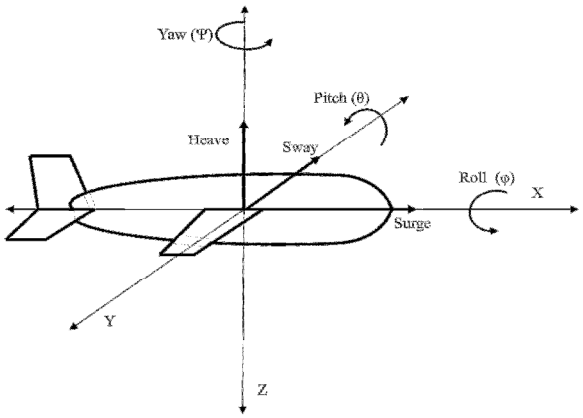

Figure 2.2 Six degrees of freedom for a freely moving underwater vehicle.

The goal of motion compensation is to account for the six degrees of freedom of motions and derive a nominal path for the vehicle's trajectory. Underwater vehicles can be equipped with Internal Motion Units (IMU), Inertial Navigation Systems (INS), Doppler Velocity Logs (DVL), Global Positioning Systems (GPS) with surface fixes, Digital GPS with Ultra Short Baseline (DGPS_USBL), Underwater Transponder Positioning (UTP), altimeters, and depth sensors. The measurements of the vehicle motion from these navigation sensors are combined and filtered usually Kalman filtered to provide the best estimate of the vehicle's position. This information is then used to coarse-motion compensate the platform's position to a straight-line trajectory using either Redundant Phase Center (RPC) [Marx et al. 2000] or similarly the Displaced Phase Center Antenna (DPCA) technique [Putney et al. 2001] [Pinto et al. 2000, 2001, 2006] [Hagen et al. 2001] [Hansen et al. 2003] [Callow et al. 2005, 2009] [Heremans et al. 2006] [Bellettini et al 2006, 2007]. After beamforming autofocus techniques such as: Phase Center Antenna (PCA), contrast-optimization, and map-drift are used to fine tune (micronavigation) the motion compensation and minimize the effects of medium variation to improve the final image.

2.2.1 Rotational Matrix

The rotational matrix is derived from the Euler angles. The right-hand rule is used to determine the positive directions for the rotational matrix. Roll and pitch information are obtained from the IMU, and yaw is usually derived from a ring laser gyro (heading less nominal heading).

$R_1\varphi$ is the rotation about the X-axis referred to as roll.

$$R_{1\varphi} = \begin{pmatrix} 1 & 0 & 0 \\ 0 & cos(\varphi) & sin(\varphi) \\ 0 & -sin(\varphi) & cos(\varphi) \end{pmatrix} \tag{2.1}$$

$R_2\theta$ is the rotation about the Y-axis referred to as pitch.

$$R_{2\theta} = \begin{pmatrix} cos(\theta) & 0 & -sin(\theta) \\ 0 & 1 & 0 \\ sin(\theta) & 0 & cos(\theta) \end{pmatrix} \quad (2.2)$$

$R_{3}\psi$ is the rotation about the Z-axis referred to as yaw.

$$R_{3\psi} = \begin{pmatrix} cos(\psi) & sin(\psi) & 0) \\ -sin(\psi) & cos(\psi) & 0 \\ 0 & 0 & 1 \end{pmatrix} \quad (2.3)$$

The Rotation Matrix is a combination of the roll, pitch and yaw.

$$R_{IMU}(t) = R_{1\varphi} R_{2\theta} R_{3\psi}$$

$$R_{IMU}(t) = \begin{pmatrix} 1 & 0 & 0 \\ 0 & cos(\varphi) & sin(\varphi) \\ 0 & -sin(\varphi) & cos(\varphi) \end{pmatrix} \begin{pmatrix} cos(\theta) & 0 & -sin(\theta) \\ 0 & 1 & 0 \\ sin(\theta) & 0 & cos(\theta) \end{pmatrix} \begin{pmatrix} cos(\psi) & sin(\psi) & 0) \\ -sin(\psi) & cos(\psi) & 0 \\ 0 & 0 & 1 \end{pmatrix} \quad (2.4)$$

R is the total rotation of the vehicle

$$R = R_{IMU}(t) + \Phi(t) d_m \quad (2.5)$$

R_{IMU} is the rotational matrix Eq. (2.4) from the IMU, $\Phi(t)$ is the rotational matrix from the body coordinate axis to the external coordinate axis, and d_m is the distance from the body center of mass to the receiver.

2.2.2 Displacement Matrix

Surge, sway, and heave are also derived from the IMU and multiplied by the displacement matrix P. The change in range is converted to a time delay and added to the data for each receiver. The goal here is to preserve the phase for InSAS processing. The method of least squares is then used to smooth the displacement.

P_1 is the surge displacement in the X – direction

$$P_1 = \begin{pmatrix} -1 & 0 & 0 \\ 0 & 1 & 0 \\ 0 & 0 & 1 \end{pmatrix} Surge \quad (2.6)$$

P_2 is the sway displacement in the Y – direction

$$P_2 = \begin{pmatrix} 1 & 0 & 0 \\ 0 & -1 & 0 \\ 0 & 0 & 1 \end{pmatrix} Sway \tag{2.7}$$

P_3 is the heave displacement in the Z – direction

$$P_3 = \begin{pmatrix} 1 & 0 & 0 \\ 0 & 1 & 0 \\ 0 & 0 & -1 \end{pmatrix} Heave \tag{2.8}$$

The total displacement of the vehicle is

$$P = P_1 + P_2 + P_3 \tag{2.9}$$

IMU's in general are not precise enough for SAS systems that require the motion to be known within an eighth of a wavelength over the entire aperture, but it is a good starting point. Vehicle motion compensation is essential because the vehicle traverses the aperture, causing the range to a given object on the seafloor to follows a parabolic curve. This is referred to as range migration in space-time. In this chapter Displaced Phase Center Antenna (DPCA) and Stripmap Phase Gradient Autofocus (SPGA) motion compensation techniques will be presented.

2.3 Motion Compensation

2.3.1 Displaced Phase Center Antenna or Redundant Phase Center

Displaced Phase Center Antenna (DPCA) or Redundant Phase Center (RPC) is a technique for motion compensation. It is used to focus the SAS image by accurately measuring the displacement in the image. This method correlates two signals from consecutive pings from overlapping receivers to estimate the time delay. The equivalent phase center assumption of the transmit receiver pair is the midpoint between both the transmitter and receiver. Figure 2.3 shows the configuration for a DPCA system for an eighteen receiver array moving along the vehicle trajectory *Y* for two consecutive transmit receive cycles[Cook 2007] [Bonifant 1999].

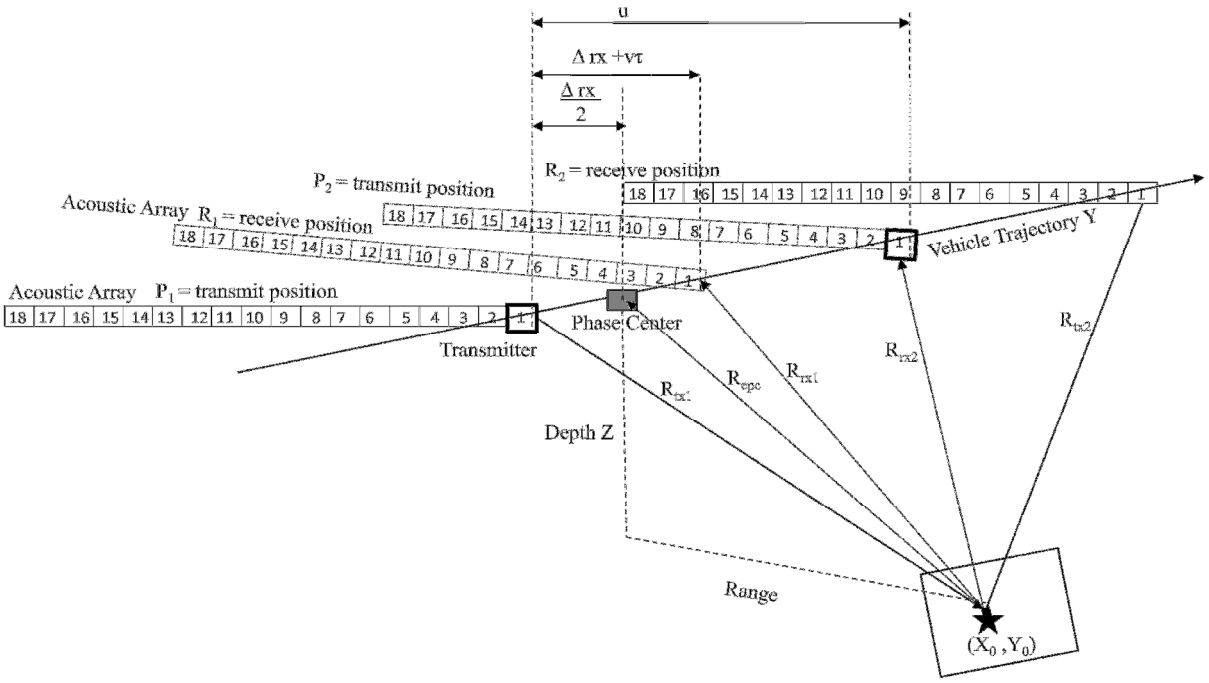

Figure 2.3 DPCA : (x_o, y_o) is a patch on the seafloor, Δ_{rx} is the distance between transmitter and receiver, R_{tx1} is the range from the transmitter to the patch on the seafloor, R_{rx1} is the range from the patch on the seafloor to the receiver, R_{epc} is the equivalent phase center between the transmitter and the receiver, R_{tx2} is the range from the transmitter to the patch on the seafloor for the second ping, and R_{rx2} is the range from the patch on the seafloor to the receiver for the second ping.

Range R_{tx} from transmitter to the patch on the seafloor is

$$R_{tx} = \sqrt{(x_0^2+(y_0 - u)^2} \tag{2.10}$$

(x_o, y_o) is a patch on the seafloor, and the transmitter is located at the along track position u. Range R_{rxs} from target to receiver for a stationary vehicle is

$$R_{rxs} = \sqrt{x_0^2+(y_0 - u - \Delta_{rx})^2} \tag{2.11}$$

Δ_{rx} is the distance between the transmitter and the receiver. Range R_{rx} from the patch on the seafloor (x_o, y_o), to the receiver with the vehicle moving at velocity v is

$$R_{rx} = \sqrt{x_0^2 + (y_0 - u - \Delta_{rx} - v\tau)^2} \tag{2.12}$$

$v\tau$ is the range the vehicle traveled from the time of the ping to the time of receipt. Range R_{epc} for the equivalent phase center is

$$R_{epc} = \sqrt{x_0^2 + \left(y_0 - u - \frac{\Delta_{rx}}{2}\right)^2} \tag{2.13}$$

Range error ΔR for the equivalent phase center is

$$\Delta R = R_{tx} + R_{rx} - 2R_{epc} \tag{2.14}$$

Phase difference φ_e caused by range difference is

$$\varphi_e = e^{ik\Delta R} \tag{2.15}$$

k is the wavenumber $(k = \omega/c)$, and ΔR is the range error.

$$\Delta R = \sqrt{x_0^2 + (y_0 - u)^2} + \sqrt{x_0^2 + (y_0 - u - \Delta_{rx})^2} - 2\sqrt{x_0^2 + \left(y_0 - u - \frac{\Delta_{rx}}{2}\right)^2} \tag{2.16}$$

Using a Taylor series expansion for square roots, neglecting the higher order terms and keeping only the second order terms the range can be simplified to

$$\Delta R \approx \frac{\Delta_{rx}^2}{4x_0} \tag{2.17}$$

The equivalent time delay is

$$\tau_{pc} = \frac{\frac{\Delta_{rx}^2}{4x_0}}{C} \tag{2.18}$$

Ideally the advance per ping should be set to be an integer number of phase center spacings that is less than the total number of receivers in the SAS array to have equivalent phase center pairs. The velocity of the vehicle *v* should be

$$v = \left(\frac{N-M}{2}\right) D \times ping\ rate \tag{2.19}$$

N is the number of receivers in the array, *M* is the number of overlapping receivers, and *D* is the distance between receivers (see Figure 2.3). The phase center of the second ping will be displaced by the amount $\frac{2\Delta_x}{c}$ from the first ping

$$S_n(t) \rightarrow S_{n+1}\left(t - \frac{2\Delta_x}{c}\right) \tag{2.20}$$

The expectation *E[]* of the cross-correlation $R_{n,n+1}$ of the received signal from the first ping $S_n(t)$, and the second ping $S_{n+1}(t-k)$, ($k=n-m$) is

$$R_{n,n+1}(k) = E\left[\sum S_n(t)\, S_{n+1}^H(t-k)\right] \tag{2.21}$$

The complex reflectivity distribution is a zero mean, spatially white, complex Gaussian random function, therefore the cross correlation results in a Dirac delta function.

$$R_{n,n+1}(k) = E\left[\sum S_n(t)\, S_n^H\left(t - k + \frac{2\Delta_x}{c}\right)\right] = \delta\left[k - \frac{2\Delta_x}{c}\right] \tag{2.22}$$

In Figure 2.3 the AUV is traveling at a velocity *v*, receivers 1 through 3 from the first ping align with receivers 16 through 18 for the second ping. The three overlapping phase center pairs provide a good estimate of the AUV's motion. The non-overlapping receivers are used for imaging. The time delay $\Delta\tau$ between the first ping (*p*), and second ping (*p+1*), for hydrophone *n (1,2,3)* and *m (16,17,18)* is

$$\Delta\tau = t_{p+1}^m - t_p^n \tag{2.23}$$

The time delay for hydrophone *n* is

$$\tau_p^n = \frac{1}{c}\left[\left|R_{tx}(t_p)\right| + \left|R_{rx}^n(t_p + \tau_p^n)\right|\right] \tag{2.24}$$

R_{tx} is the range from the transmitter to the patch on the seafloor (x_0, y_0), R_{rx} is the range from the patch on the seafloor (x_0, y_0) to the receiver, and c is the speed of sound in the water. The range of the transmit signal is expanded to include the position on the patch of the seafloor, vehicle position, and vehicle rotation.

$$R_{tx}(t_p) = S(t_p) - X(t_p) - \Phi(t_p)d_{tx} \tag{2.25}$$

$S_{(tp)}$ is the range to the position of the patch of seafloor, $X_{(tp)}$ is the vehicle position, and $\Phi_{(tp)}$ is the rotational matrix, and d_{tx} is the distance from the body center of mass to the transmitter. Similarly to Eq. (2.25) the range for the received signal is expanded to include the rotation matrix.

$$R_{rx}^n(t_p + \tau_p^n) = S(t_p + \tau_p^n) - X(t_p + \tau_p^n) - \Phi(t_p + \tau_p^n)d_{rx}^n \tag{2.26}$$

$S_{(tp+\tau p^n)}$ is the range to the position of the patch of seafloor, $X_{(tp+\tau p^n)}$ is the vehicle position at receipt of the signal and $\Phi_{(tp+\tau p^n)}$ is the rotational matrix at the time of receipt, and d_{rx} is the distance from the body center of mass to the receiver. The total time delay from transmit to receipt is

$$\tau_p^n = \frac{1}{c}\left[\left|S - X(t_p) - \Phi(t_p)d_{tx}\right| + \left|S - X(t_p + \tau_p^n) - \Phi(t_p + \tau_p^n)d_{rx}^n\right|\right] \tag{2.27}$$

Similarly for the second ping and second set of hydrophones the delay is

$$\tau_{p+1}^m = \frac{1}{c}\left[\left|R_{tx}(t_{p+1})\right| + \left|R_{rx}^m(t_{p+1} + \tau_{p+1}^m)\right|\right] \tag{2.28}$$

R_{tx} is the range from the vehicle to the patch on the seafloor (x_0, y_0), R_{rx} is the range from the patch on the seafloor (x_0, y_0) to the receiver after the second ping, and c is the speed of sound in water. Including the vehicle rotation Eq. (2.28) becomes

$$\tau_{p+1}^m = \frac{1}{c}\left[\left|S - X(t_{p+1}) - \Phi(t_{p+1})d_{tx}\right| + \left|S - X(t_{p+1} + \tau_{p+1}^m) - \Phi(t_{p+1} + \tau_{p+1}^m)d_{rx}^m\right|\right] \tag{2.29}$$

S is the range to the position of the patch of seafloor, *X* is the position of the vehicle center of mass, $\Phi(t)$ is the vehicle rotational matrix, d_{tx} is the distance from the vehicle center to transmitter, and $d_{rx}^{\ n}$ is the distance from the vehicle center to the n^{th} hydrophone. The position of the vehicle in the external coordinate system is

$$X(t_p+\tau_p^n) \approx X(t_p) + \tau_p^n v(t_p) \tag{2.30}$$

X is the vehicle center of mass, τ is the time between pings, and $v(t_p)$ is the velocity of the vehicle. The rotation of the vehicle from time of transmission to time of reception can be factored into two subsequent rotations.

$$\Phi(t_p+\tau_p^n) = \Psi(\tau_p^n)\Phi(t_p) \tag{2.31}$$

$\Psi_{(\tau p^{n})}$ is the rotation during flight, and $\Phi_{(tp)}$ is the rotation at the time of transmission. The Taylor expansion of Eq. (2.31) is

$$\Phi(t_p+\tau_p^n) \approx \Phi(t_p)+\tau_p^n \frac{\partial}{\partial \mathrm{t}}\Psi(t_p)\Phi(t_p) \tag{2.32}$$

Since $\frac{\partial \psi}{\partial t}$ is equivalent to $\frac{\partial \varphi}{\partial t}$ Eq. (2.32) becomes

$$\Phi(t_p+\tau_p^n) \approx \Phi(t_p)+\tau_p^n \frac{\partial}{\partial \mathrm{t}}\Phi(\tau_p^n)\Phi(t_p) \tag{2.33}$$

Substituting Eq. (2.33) into Eq. (2.25) and Eq. (2.26) yields a range of

$$c\tau_p^n = \left[\left|S - X(t_p) - \Phi(t_p)d_{tx}\right| + \left|S - X(t_p) + \tau_p^n v(t_p) - \left(\Phi(t_p)d_{rx}^n + \tau_p^n \omega(t_p) \times \Phi(t_p)d_{rx}^n\right)\right|\right] \tag{2.34}$$

$$\begin{aligned} c\tau_{p+1}^m = \big[&\left|S - X(t_{p+1}) - \Phi(t_{p+1})d_{tx}\right| \\ &+ \left|S - X(t_{p+1}) + \tau_{p+1}^m v(t_{p+1}) - \left(\Phi(t_{p+1})d_{rx}^m + \tau_p^m \omega(t_{p+1}) \times \Phi(t_{p+1})d_{rx}^m\right)\right|\big] \end{aligned} \tag{2.35}$$

The linear and angular velocity change is insignificant between the two pings. The above equations can be simplified to the linear translation

$$X(t_{p+1}) \approx X(t_p) + \Delta t v(t_p) \tag{2.36}$$

$$X(t_{p+1}+\tau_{p+1}^m) \approx X(t_p) + (\Delta t+\tau_{p+1}^m) v(t_p) \tag{2.37}$$

and the rotational translation is

$$\Phi(t_{p+1}) \approx \Phi(t_p) + \Delta t \omega(t_p) \times \Phi(t_p) \tag{2.38}$$

$$\Phi(t_{p+1}+\tau_{p+1}^m) \approx \Phi(t_p) + (\Delta t+\tau_{p+1}^m) \omega(t_p) \times \Phi(t_p) \tag{2.39}$$

The range for the observed time delay for the Redundant Phase Center Pair is

$$c\Delta\tau = (\tau_{p+1}^m - \tau_p^n) \tag{2.40}$$

$$\begin{aligned} c\Delta\tau = \big[& \big| S - \{X(t_p) + \Delta t v(t_p)\} - \{\Phi(t_p) d_{tx} + \Delta t \omega(t_p) \times \Phi(t_p) d_{tx}\} \big| \\ & - \big| S - X(t_p) - \Phi(t_p) d_{tx} \big| \\ & + \big| S - \{X(t_p) + (\Delta t + \tau_{p+1}^m) v(t_p)\} \\ & - \{\Phi(t_p) d_{rx}^m + (\Delta t + \tau_f^m) \omega(t_p) \times \Phi(t_p) d_{rx}^m\} \big| \\ & - \big| S - \{X(t_p) + \tau_p^n v(t_p)\} \\ & - \{\Phi(t_p) d_{rx}^n + \tau_p^n \omega(t_p) \times \Phi(t_p) d_{rx}^n\} \big| \big] \end{aligned} \tag{2.41}$$

Time delay for the vehicle motion is

$$\Delta\tau = \frac{1}{c} \left[R_{tx}(t_{p+1}) - R_{tx}(t_p) + R_{rx}(t_{p+1} + \tau_{p+1}^m) - R_{rx}(t_p + \tau_p^n) \right] \tag{2.42}$$

2.4 Autofocus

Autofocusing techniques fine tune the image by correcting for uncompensated motion errors and variations in the medium. There are two classes of autofocusing, one relying on space unstationarity of the backscattered strength

(scatter) and the second using the backscattering space modulation caused by the transmit directivity pattern (directivity) [Billion & Pinto 1995]. Autofocus techniques currently in practice are phase center antenna (PCA), phase gradient algorithm (PGA) [Hawkins 1996] [Gough & Lane 1998] [Callow et al. 2001] [Callow et al. 2003], Shear Averaging [Callow et al. 2001], contrast optimization [Griffith 1993] [Gough 1998] [Banks 2000] [Silva et al. 2009], Map drift [Gough 2003] [Hansen et al. 2005] and multilook image registration [Griffith 1997]. Autofocus is sometimes performed separate from or after the interferometry. The Stripmap Phase Gradient Autofocus (SPGA) is presented here for completeness.

2.4.1 Stripmap Phase Gradient Autofocus Algorithm SPGA

The phase gradient algorithm PGA is based on the assumption that the phase error function is constant in the range dimension and has the same effect on each scatterer [Hayes et al. 2003]. The motion affected pulse compressed data is

$$\widehat{ss}(t,u) = \mathcal{M}(ss(t,u); X(u)) \tag{2.43}$$

Where *X(u)* is the unknown position error as a function of the along track position, *u, t* is time delay of the range. *M* is the motion induced transformation. The goal is to estimate *X(u)* from $\widehat{ss}(t,u)$ and recover *ss (t,u)*, the basebanded received signal in the temporal-spatial domain. The proposed autofocus algorithm operates on regions of the distorted reconstructed image.

$$\widehat{ff}(x,y) = \mathcal{A}\{ss_b(t,u)\} \tag{2.44}$$

A is an operator that represents the azimuth compression performed by the image reconstruction algorithm (see chapter 3). The pulse compressed signal may be described using a two dimensional convolution of the target distribution with a range variant point spread function.

$$\widehat{Ss_b}(\omega_b,u) = |P_b(\omega_b)|^2 \iint ff(x_1,y_1)\, H(X(u)-x_1, u-y_1, \omega)\, e^{-i2k\sqrt{(X(u)-x_1)^2+(u-y_1)^2}}\, dx_1 dy_1 \tag{2.45}$$

P_b is the basebanded transmit pulse, *ff* is the reflectivity of the patch of seafloor at point (x_1,y_1), H is the point spread function, where the point spread function is the squared free space of the three-dimensional Green's function weighted by the beam pattern.

$$H(X(u)-x_1, u-y_1, \omega) = \frac{e^{-ik\sqrt{(X(u)-x)^2+(u-y_1)^2}}}{4\pi^2(X(u)-x)^2+(u-y_1)^2} \times B^2 \frac{\omega(u-y_1)D_y}{\sqrt{(X(u)-x)^2+(u-y_1)^2}} \tag{2.46}$$

Ignoring elevation and assuming a three-dimensional point scatterer from the target and using the stop and hop method. Assume the sway is small compared to the across-track target position the point spread function can be approximated.

$$H(X(u)-x_1,u-y_1,\omega) \approx e^{-i2kX(u)\frac{x_1}{\sqrt{x_1{}^2+(u-y_1)^2}}} \times H(x_1,u-y_1,\omega) \tag{2.47}$$

Let θ be the angle from the sonar to the target at (x_1, y_1)

$$cos\theta(u) = \frac{x_1}{\sqrt{x_1{}^2+(u-y_1)^2}} \tag{2.48}$$

Point spread function becomes

$$H(X(u),u-y_1,\omega) \approx e^{-i2kX(u)cos\theta(u)} H(x_1,u-y_1,\omega) \tag{2.49}$$

The pulse compressed echo with motion $X(u)$ can be written as

$$\widehat{Ss_b}(\omega_b,u) \approx Ss_b(\omega_b,u)\, e^{-i2kX(u)} \tag{2.50}$$

$X(u) = X$ in the presence of a small constant sonar sway. The image is displaced in range when there is a small constant linear sway. $X(u) = \sigma u$ for a very small linear sway gradients σ and large offsets x_0. It can be approximated by an along-track shear in the along-track direction.

$$ff(x,y) \approx ff(x-\sigma y, y+\sigma x) \tag{2.51}$$

The effects of a linear sway in the spatial frequency domain appears as a rotation. It is found by taking a two-dimensional FFT of Eq. (2.51).

$$\widehat{FF}\left(k_x,k_y\right) \approx FF\left(k_{x_x}-\sigma k_y, k_y+\sigma k_x\right) \tag{2.52}$$

The FFT of the pulse compressed echo data is

$$\widehat{Ss}(\omega,u) \approx \int \widehat{Ss}(t,u)\, e^{-i\omega t}\, dt \tag{2.53}$$

Corrected for the known sway *X(u)* is

$$\widehat{Ss}(\omega_b,u) \approx \widehat{Ss}(\omega,u)\, e^{-i2kX(u)} \tag{2.54}$$

Reconstruct the image *ff(x,y)* from the above equation using the wavenumber algorithm. Find a prominent point in *ff(x,y)* and its coordinates (x_m,y_m). Create masks W_m centered on (x_m,y_m).

$$W_m(x,y) = rect\left(\frac{x-x_m}{W_x}\right) rect\left(\frac{y-y_m}{W_y}\right) \tag{2.55}$$

Form images containing regions of interest

$$\widehat{ff_m}(x,y) = W_m(x,y)\widehat{ff}(x,y) \tag{2.56}$$

The two-dimensional FFT is

$$\widehat{FF}\left(k_x,k_y\right) = \widehat{ff_m}(x,y) \tag{2.57}$$

Determine the average along-track spatial energy density

$$\beta_m\left(k_y\right) = \int \left|\widehat{FF}\left(k_x,k_y\right)\right|^2 dk_x \tag{2.58}$$

Calculate the centroid of the along-track spatial energy density spectrum allowing for circular wrapping using.

$$\Delta k_y = \frac{k_{ymax}}{\pi}\, phase \iint \left|\widehat{f_m}\left(k_x,k_y\right)\right|^2 dk_x \times e^{\frac{\pi k_y}{k_{ymax}}} dk_y \tag{2.59}$$

Estimate the local linear sway gradient

$$\sigma_m = \frac{\Delta k_y}{2k_0} \tag{2.60}$$

Estimate the true target position *(x'$_m$, y'$_m$)*.

$$x'_m = x_m \tag{2.61}$$

$$y'_m = y_m - \sigma_m x_m \tag{2.62}$$

Phase correct the spatial spectrum to account for the estimated target position

$$\widehat{FF}'(k_x, k_y) = \widehat{FF}(k_x, k_y) e^{-ik_x(x'_m - x_m)} e^{-ik_x(y'_m - y_m)} \tag{2.63}$$

Apply the wavenumber transform to form

$$\chi_m(k_x, u) = \widehat{FF}\left(k_x \frac{y_m - u}{x_m}, k_x\right) \tag{2.64}$$

Calculate the complex error gradient using a sheared product

$$\psi_m(k_x, u) = \chi_m(k_x, u + \Delta u)\chi_m^H(k_x, u) \tag{2.65}$$

Average the phase error gradients with an amplitude weighting using

$$\Delta\varphi(u) = phase\{\Psi(u)\} \tag{2.66}$$

$$\Psi(u) = \int \sum_{m=1}^{M} \psi_m(k_x, u) dk_x \tag{2.67}$$

Integrate the average phase error gradient

$$\varphi(u) = \varphi(y - \Delta u) + \Delta\varphi(y - \Delta u) \tag{2.68}$$

Scale the phase error estimate by the wavelength of the center frequency and estimate the residual sway

$$\hat{X}_\iota(u) = \frac{\varphi(u)}{2k_0} \tag{2.69}$$

Iterate algorithm until the residual sway is smaller than a given threshold. The total estimated sway is the sum of the estimated residual sways from each iteration.

$$\hat{X}(u) = \sum_{i=1}^{I} \hat{X}_\iota(u) \tag{2.70}$$

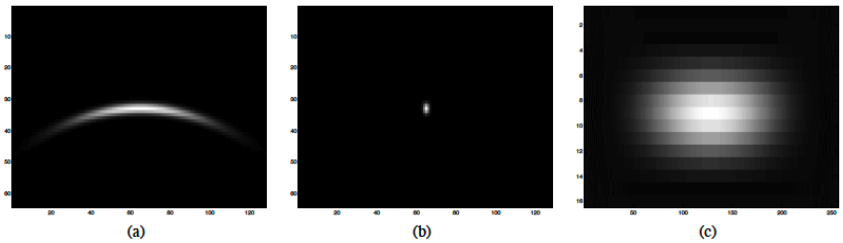

Figure 2.4 Image of a point target with no linear sway: (a) magnitude of pulse compressed target *ss(t,u)*, (b) magnitude of SAS image $\widehat{ff}(x,y)$, (c) real part of spatial fourier transform $\widehat{FF}(f_x,f_y)$ [Hayes et al. 2003].

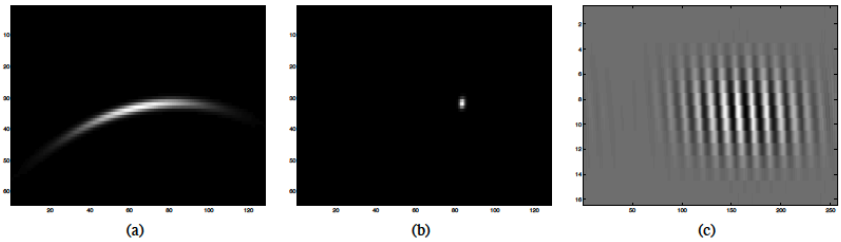

Figure 2.5 Image of a point target with a linear sway (X(y)=0.05y): (a) magnitude of pulse compressed signal *ss(t,u)*, (b) magnitude of SAS image $\widehat{ff}(x,y)$, (c) real part of spatial fourier transform $\widehat{FF}(f_x,f_y)$ [Hayes et al. 2003].

A new widebeam multiple receiver motion compensation method developed by Callow takes advantage of the direction of arrival information [Callow et al. 2009]. The received echo in the time domain is

$$ee_m(t,u,\sigma) \approx \iint \frac{ff(x,y)p(t-\Delta t)}{(4\pi)^2\sqrt{x^2+(u-y)^2}+\sqrt{x^2+(u+\sigma-y)^2}}dxdy \tag{2.71}$$

ff (x,y) is the image of the scene, *p(t)* is the transmit pulse, σ is the along track receiver offset, *(x, y)* is the target position. The time delay is

$$\Delta t = \frac{1}{c}\sqrt{x^2 + (u-y)^2} + \sqrt{x^2 + (u+\sigma-y)^2} \tag{2.72}$$

Apply the Phase Center Approximation (PCA)

$$ee_m(t,u,\sigma) \approx \iint \frac{ff(x,y)p\left(t - \frac{2}{c}\sqrt{x^2 + \left(u + \frac{\sigma}{2} - y\right)^2}\right)}{(4\pi)^2\sqrt{x^2 + \left(u + \frac{\sigma}{2} - y\right)^2}} dxdy \tag{2.73}$$

PCA with position error is

$$\widehat{ee_m}(t,u,\sigma) \approx \iint \frac{ff(x,y)p(t-\Delta t)}{(4\pi)^2\sqrt{x^2 + \left(u + \frac{\sigma}{2} - y\right)^2}} dxdy \tag{2.74}$$

The change in time delay due to position error is

$$\Delta t = \frac{2}{c}\sqrt{(\Delta x(u) - x)^2 + \left(u + \frac{\sigma}{2} - y\right)^2} \tag{2.75}$$

Simplify Eq. (2.74) by using Eq. (2.73) and the binomial expansion becomes

$$\widehat{ee_m}(t,u,\sigma) \approx ee_m\left(t - \frac{2}{c}\Delta x(u)\left(\frac{2x + \Delta x(u)}{2r_0}\right), u, \sigma\right) \tag{2.76}$$

The range to the center of the scene is

$$r_0 = \sqrt{(\Delta x(u) - x)^2 + \left(u + \frac{\sigma}{2} - y\right)^2} \tag{2.77}$$

The equation simplifies to

$$\widehat{ee_m}(t,u,\sigma) \approx ee_m\left(t - \frac{2}{\mathrm{c}}\Delta\mathrm{x(u)}\cos\theta\,,\mathrm{u},\sigma\right) \tag{2.78}$$

θ is the target angle for the co-located transducer. Assume the system is narrowband, Eq. (2.76) can be approximated as

$$\widehat{ee_m}(t,u,\sigma) \approx \iint \frac{ff(x,y)p(t-\Delta\mathrm{t})}{(4\pi)^2\sqrt{x^2+\left(u+\frac{\sigma}{2}-y\right)^2}}dxdy \tag{2.79}$$

The time delay is

$$\Delta\mathrm{t} = \frac{2}{\mathrm{c}}\left(\sqrt{\mathrm{x}^2+\left(u+\frac{\sigma}{2}-y\right)^2}-\Delta\mathrm{x(u)}\right) \tag{2.80}$$

Eq.(2.80) allows for the sway to be treated as a time shift.

$$\widehat{ee_m}(t,u,\sigma) \approx ee_m\left(t - \frac{2}{\mathrm{c}}\Delta\mathrm{x(u)},\mathrm{u},\sigma\right) \tag{2.81}$$

The sway error per ping is

$$\Delta\mathrm{x_p} \equiv \Delta\mathrm{x}\left(\mathrm{u_p}\right) \tag{2.82}$$

The cross-track error is

$$\epsilon = 2\Delta\mathrm{x_p}(1-\cos\theta) \tag{2.83}$$

The improved motion compensation algorithm is

$$Ee\left(\omega,k_\sigma,\mathrm{u_p}\right) \approx \iint ee_m(t,u,\sigma)e^{-i(\omega t+k_\sigma\sigma)}\,dtd\sigma \tag{2.84}$$

$$k_\sigma = k sin\theta_\sigma \tag{2.85}$$

The widebeam compensation for the displacement is

$$Ee(\omega, k_\sigma, \mathrm{u_p}) = Ee(\omega, k_\sigma, \mathrm{u_p}) e^{-i2\Delta \mathrm{x_p}\left(\sqrt{k^2 - k_\sigma^2}\right)} \tag{2.86}$$

The phase center approximation is

$$EE(\omega, k_\sigma, k_u) = \widehat{EE}(\omega, k_\sigma, k_u) e^{-i2\Delta \mathrm{x_p}\left(\sqrt{k^2 - \frac{1}{4}k_y^2}\right)} \tag{2.87}$$

$$Ee(\omega, \sigma, \mathrm{u_p}) = \widehat{Ee}(\omega, \sigma, \mathrm{u_p}) e^{-i2k\Delta \mathrm{x_p}} \tag{2.88}$$

The yaw compensation is

$$\widehat{ee_m}(t, u, \sigma) \approx \iint \frac{ff(x, y) p(t - \Delta \mathrm{t})}{(4\pi)^2 \sqrt{x^2 + \left(u + \frac{\sigma}{2} - y\right)^2}} dxdy \tag{2.89}$$

The time delay for yaw is

$$\Delta \mathrm{t} = \frac{2}{\mathrm{c}} \times \sqrt{\left(\mathrm{x} - \frac{\sigma}{2} sin\Phi(\mathrm{u})\right)^2 + \left(\mathrm{u} + \frac{\sigma}{2} cos\Phi(\mathrm{u}) - \mathrm{y}\right)^2} \tag{2.90}$$

2.5 Doppler Shift

Doppler shift is an apparent shift in the frequency of a signal due to the movement of the vehicle. For a moving source the wavelength is

$$\lambda = \frac{c - v_s}{f_s} \tag{2.91}$$

c is the speed of sound, f_s is the frequency of the source and v_s is the velocity of the source. The frequency at the receiver f_r from a source moving in the positive direction

$$f_r = \frac{f_s(c - v_r)}{(c - v_s)} \tag{2.92}$$

The frequency at the receiver f_r for the bistatic case is

$$f_r = \frac{f_s(c + v_0 \cos\theta_s)}{c - v_0 cos\theta_r} \tag{2.93}$$

f_s is the frequency at the source, c is the speed of sound in water, v_0 is the speed of the vehicle, θ_s is the direction of arrival from the source and θ_r is the direction of arrival from the receiver.

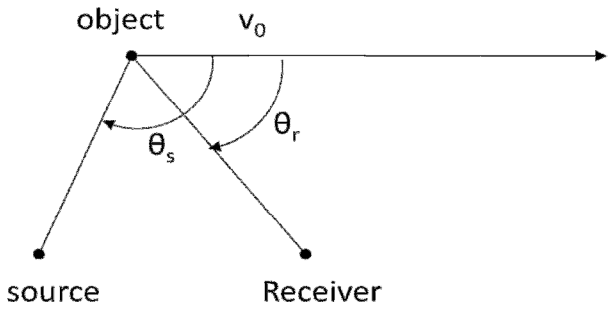

Figure 2.6 Doppler Shift for the bistatic case (moving vehicle or source and receiver not co-located).

A moving sea surface with velocity $|u|cos\gamma$ will impart a Doppler shift in the received frequency.

$$\delta f = f_0 \frac{2|v_0|}{c} cos\gamma \tag{2.94}$$

f_0 is the frequency of the source, γ is the direction of the receiver relative to the source and the current, v_o is the speed of the current and c is the speed of sound of the water.

Summary

In this chapter, I presented the six degrees of freedom for an AUV, DPCA for coarse and SPGA for fine motion compensation for InSAS systems, and the Doppler shift in frequency for a moving vehicle.

Chapter 3 Sonar Signal Processing

3.1 Synthetic Aperture Sonar Signal Processing

A synthetic aperture sonar (SAS) system mounted on an autonomous underwater vehicle (AUV) traverses a path in the along-track or cross-range direction *y* (slow-time), transmitting a pulse at position *u* (on the y-axis) that ensonifies an area (X_s, Y_s) of the seafloor. The amplitude and phase of the backscattered acoustic plane wave in the cross-track or along-range direction *x* received at the SAS is processed to produce an image of the seafloor. This chapter presents the sonar signal processing techniques required to produce the stripmap SAS image of the seafloor from a reflected acoustic plane wave.

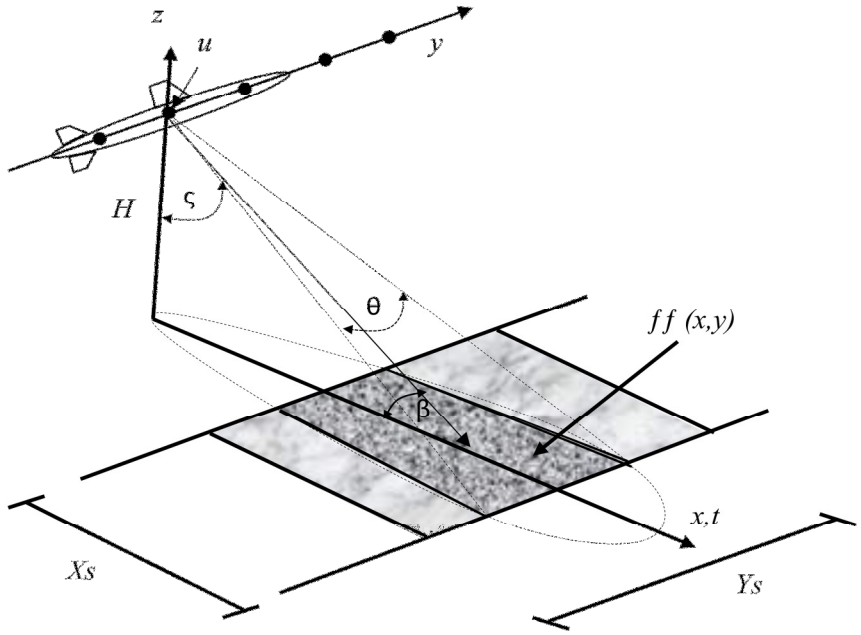

Figure 3.1 Stripmap synthetic aperture imaging geometry. *Xs* is the swath length, *Ys* is the swath width of the ensonified area (*Xs Ys)* of the seafloor, *H* is the height (altitude) of the vehicle above the seafloor, ς is the tilt angle, θ is the beamwidth, β is the grazing angle, and *ff(x,y)* is the reflectivity of the scene.

3.1.1 Range Resolution

The transmitted pulse passes through the ocean medium as an acoustic pressure wave ensonifying a patch of the seafloor whose cross-track (along-range or fast-time) range is

$$X_s = \frac{c}{2B_w \cos\beta} = \frac{c}{2B_w \sin\varsigma} \tag{3.1}$$

c is the speed of sound, B_w is the bandwidth, β is the grazing angle, or alternately the sine of the tilt angle ς. It is divided by two to account for the return trip. The width (azimuth-range) of the ensonified patch of the seafloor is

$$Y_s = R\theta_{3dB} = R\frac{\lambda}{L_{sa}} \tag{3.2}$$

R is the range, θ_{3dB} is the azimuth of the half power point on the main axis of the beam θ_{3dB} = -3dB, λ is the wavelength of the center frequency of the transmit signal, and L_{sa} is the length of the synthetic aperture. Therefore, the area of the ensonified patch of the seafloor is

$$X_s Y_s = R\,\frac{\lambda}{L_{sa}}\frac{c}{2B_w cos\,\beta} \tag{3.3}$$

Cross-track (range) and along-track resolution are estimated at the half power *(θ_{3dB} = -3dB)* point on the main axis of the beam.

$$Range\ Resolution = \delta_x = \alpha_w\frac{c\tau}{2} = \alpha_w\frac{c}{2B_w cos\,\beta} \tag{3.4}$$

α_w is a weighting constant often referred to as windowing or shading (see appendix A2), c is the speed of sound, τ is the pulse length, B_w is the bandwidth of the signal, and β is the grazing angle.

$$Along\ Track\ Resolution = \delta_y = R\frac{\lambda}{2L_{sa}} = \frac{R\lambda}{2\frac{R\lambda}{D}} \approx \frac{D}{2} \tag{3.5}$$

R is the range, L_{sa} is the length of the synthetic aperture, λ is the wavelength of the center frequency of the transmit signal, and D is the length of the real aperture. Synthetic aperture offers an along-track resolution independent of range. The backscattered strength for the ensonified patch is the reflectivity of the seafloor. It is complex with a magnitude and phase.

$$ff(x,y) = |ff(x,y)|e^{i\varphi_x\varphi_y} \tag{3.6}$$

3.1.2 Frequency Sample

Since the maximum spatial frequency based on the Nyquist frequency for a propagating wave is $2/L_{sa}$, The sampling frequency should be sampled finer than half a wavelength $L_{sa}/2$ preferably $L_{sa}/3$. However, Hawkins has found that sampling at $L_{sa}/4$ significantly reduces any residual artifacts or aliasing and some researcher suggest $L_{sa}/8$. This constrains the velocity of the vehicle to

$$V_{max} = \frac{cD}{4Xs} \tag{3.7}$$

c is the speed of sound, D is the aperture, and X_s is the ensonified cross-track length.

3.2 Fast Fourier Transform (FFT)

In SAS processing there are four domains to transform into Spatial-Temporal, Temporal-frequency, Range-Doppler, and Wavenumber. In this section, the notation will be lowercase time domain, and uppercase either the frequency or spatial domain, which will be indicated in the following set of parenthesis [Bracewell 2000]. An FFT in the cross - track direction performed on a signal in the temporal spatial domain $xx(t,u)$ transforms the signal to the temporal-frequency spatial domain $Xx(\omega,u)$.

FFT Frequency domain

$$Xx(\omega, u) = \int_{-\infty}^{\infty} xx(t, u)\, e^{-i\omega t} dt \tag{3.8}$$

To transform the signal back to the temporal domain perform an Inverse Fast Fourier Transform (IFFT).

IFFT back to the temporal domain

$$xx(t, u) = \frac{1}{2\pi} \int_{-\infty}^{\infty} Xx(\omega, u)\, e^{i\omega t} d\omega \tag{3.9}$$

An FFT performed on the along-track direction transforms the image into the range-Doppler domain, which is used in the range-Doppler image formation.

FFT Spatial domain

$$xX\left(t, k_y\right) = \int_{-\infty}^{\infty} xx(t, u)\, e^{-ik_y y} dy \tag{3.10}$$

IFFT back to the temporal domain

$$xx(t,u) = \int_{-\infty}^{\infty} xX\left(t, k_y\right) e^{ik_y y} dy \tag{3.11}$$

A two dimensional FFT transforms the data into the temporal-frequency, spatial-wavenumber domain $XX(\omega,k_u)$ This transform is used in the wavenumber and chirp-scaling methods for SAS image processing.

$$XX(\omega, k_u) = \int \int_{-\infty}^{\infty} xx(t,u)\, e^{-i\omega t} e^{-i\sqrt{4k^2 - k_u^2}x - ik_u u} dt du \tag{3.12}$$

This integral can be solved using the principle of stationary phase (see appendix 6 for details).

3.2.1 Principle of Stationary Phase

Developed by A. Papoulis for optics in 1968 the Principle of Stationary Phase can be used to approximate the above integral. Its premise is based on the fact that the amplitude is smooth and slow varying compared to the rapid oscillatory nature of the phase. In the integral the positive and negative fluctuations of the phase cancel each other and the points where the derivative of the phase are zero (stationary) survive. The approximation to the integral in the general form is

$$\int_u g_0(u) e^{i\varphi(u)}\, du \approx \sqrt{-\frac{2\pi}{\varphi''(u^*)}}\, e^{-\frac{i\pi}{4}}\, g_0(u^*) e^{i\varphi(u^*)} = A_1 e^{i\psi(k_u)} \tag{3.13}$$

$g_0(u)e^{i\varphi(u)}$ is a function with magnitude and phase at a single point u, φ is the phase, φ'' is the second derivative of the phase at u^* , u^* is the stationary point, A_1 is the complex constant, and $\psi_{(ku)}$ is the phase in the spatial-domain. When the stationary point is single valued

$$\varphi'(t^*) = 0 \tag{3.14}$$

The complex constant is

$$A_1 = \sqrt{-\frac{2\pi}{\varphi''(u^*)}} \tag{3.15}$$

The general form of the principle of stationary phase is

$$\int_u g_0(u)e^{i\varphi(u)}\,du = \sqrt{\frac{i2\pi}{\varphi''(u^*)}}\;\; g_0(u^*)e^{i\varphi(u^*)} \tag{3.16}$$

A Single point target in four domains is shown in Figure 3.2.

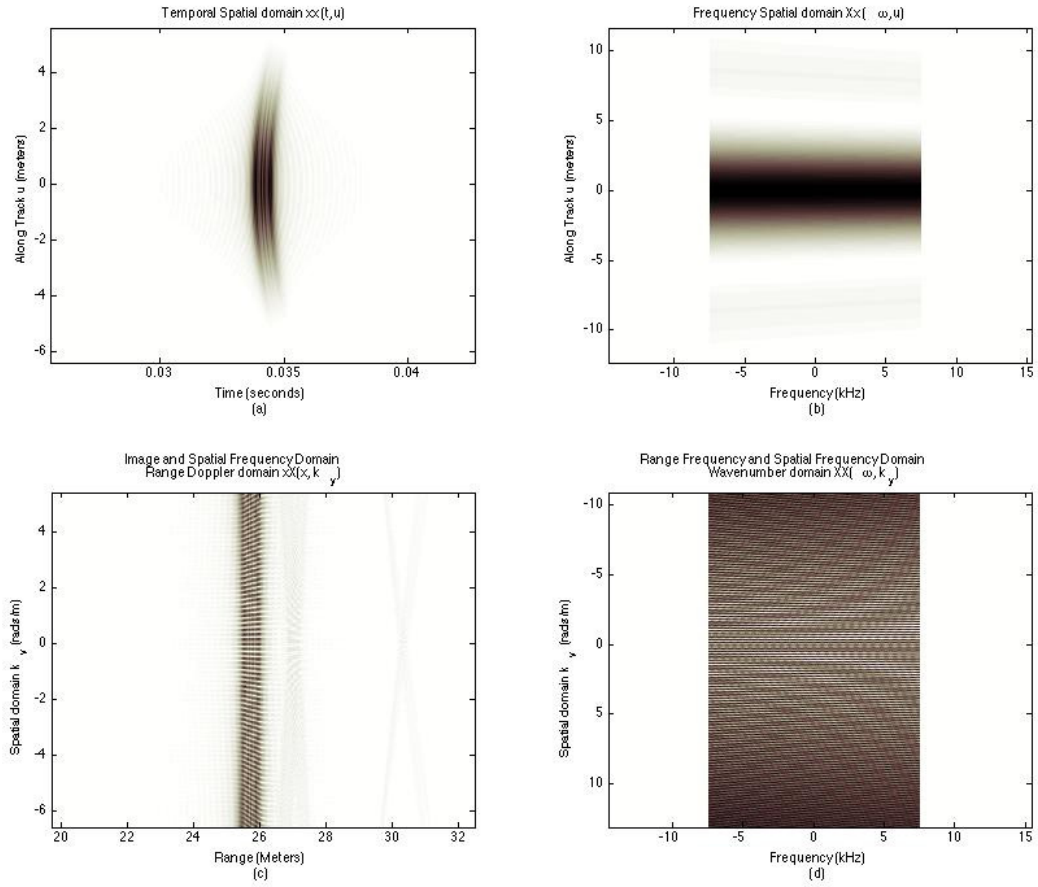

Figure 3.2 Single basebanded point target in the four domains. (a) temporal spatial, (b)frequency spatial, (c) image and spatial frequency, (d) range frequency and spatial frequency.

3.3 Transmit Chirp Signal

The transmit pulse for SAS systems vary with application, however the linear frequency modulated (LFM) chirp is common to the SAS systems presented in this dissertation. LFM chirps allows for a full bandwidth signal to be projected into the water column with greater overall energy. The LFM chirp can also take advantage of the

frequency content of the target of interest. The chirp pulse is a phase modulated signal. The standard form of the pressure $p_m(t)$ ($_m$ = modulated) for a LFM chirp is

$$p_m(t) = rect\left(\frac{t}{\tau_c}\right) e^{i2\pi f_c t + i\pi \frac{B_c}{\tau_c} t^2} = rect\left(\frac{t}{\tau_c}\right) e^{i\omega_c t + i\pi K_c t^2} \tag{3.17}$$

τ_c is the pulse length, f_c is the center frequency of the bandwidth, ω_c is the angular center frequency of the band, B_c is the chirp bandwidth , and K_c is the chirp rate (Hz/s) of the transmit pulse (acceleration through the bandwidth), not to be confused with the pulse repetition frequency (PRF).

$$K_c = \frac{B_c}{\tau_c} \tag{3.18}$$

The instantaneous frequency of the transmit pulse is obtained by taking the first derivative of the phase.

$$\frac{d\varphi}{dt} = \frac{d}{dt}(\omega_c t + \pi K_c t^2) = \omega_c + 2\pi K_c t \tag{3.19}$$

Transform the time domain signal into the frequency domain using the temporal frequency domain FFT

$$P_m(\omega) = \int_{-\infty}^{\infty} rect\left(\frac{t}{\tau_c}\right) e^{i\omega_c t + i\pi K_c t^2}\, e^{-i\omega t} dt \tag{3.20}$$

Simplified by using the principle of stationary phase, where the phase of the Fourier transformed signal is

$$\varphi(t) = \omega_c t + \pi K_c t^2 - \omega t \tag{3.21}$$

The approximate form of the Fourier transform of the modulated waveform is

$$P_m(\omega) \approx rect\left(\frac{\omega - \omega_c}{2\pi B_c}\right) \sqrt{\frac{i}{K_c}}\, e^{-i\frac{(\omega-\omega_c)^2}{4\pi K_c}} \tag{3.22}$$

Transmit pulse for this dissertation is a LFM Chirp centered at 175 kHz with a 30kHz bandwidth

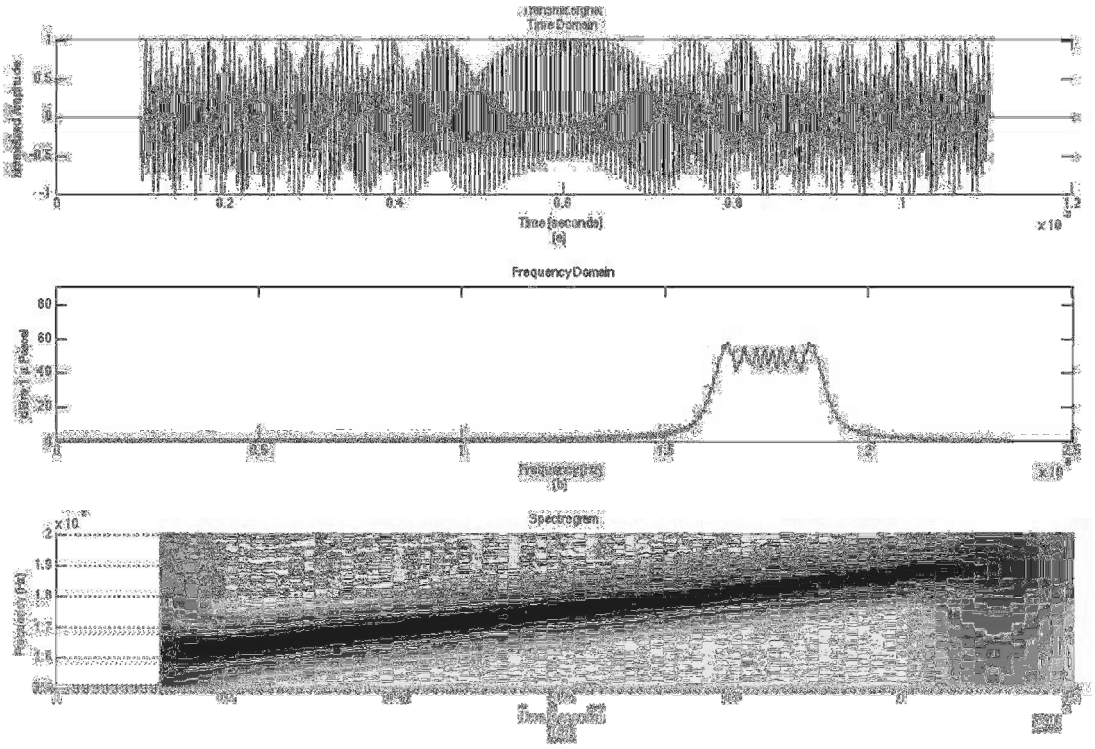

Figure 3.3 The transmit linear frequency modulated chirp signal: (a) time domain, (b) frequency domain, (c) spectrogram.

To optimize the array for the wideband chirp signal it is best to separate the signal into frequency bands by passing the signal through filter banks. Each band is then passed to an independent adaptive broadband beamfromer.

3.4 Windowing

Window functions are essential to signal processing. They are used in spectral analysis, filter design and beamforming. Windowing constrains a signal to an interval by zeroing the signal outside the interval. Windowing is accomplished by multiplying a set of weights W_k with an input signal X_k.

$$S = \sum_{n=0}^{N-1} W_n X_{kn}(t + \tau) \tag{3.23}$$

The weighting process is often referred to as tapering because the beam pattern is reduced at the ends, or shading because outside of the beam pattern has less energy or apodizing because it changes the shape (see appendix 2 for common windows used in SAS signal processing).

3.5 Filtering

Standard InSAS filtering techniques used to denoise the data are mean, median, and adaptive vector filtering. A comparison and analysis of these techniques has shown that adaptive vector filtering performed the best [Qing et al. 2004] [Ouarzeddin et al. 2005]. By measuring the average coherence between echoes at each range-bin, it is possible to accurately estimate the variance of each phase estimate, and weight accordingly. This is known as a weighted phase difference estimation (WPDE). This coherence weighting shows improved performance over other standard methods [Fortune 2005]. Wavelets have been used to denoise the data with fairly good results [Braunisch et al. 2000] [Llort-Pujol et al. 2006] [Sintes et al. 2006]. In some cases post processing filters are applied to the bathymetric map using signal to noise ratio (SNR) as a filter in weighted smoothing, weighted bilateral filtering or weighted median filtering. A comparison revealed the weighted bilateral filtering performed the best in denoising the data without destroying the edges of objects [Saebo et al. 2009].

3.6 Beamforming

3.6.1 Delay and Sum

The most basic method of beamforming is commonly referred to as conventional beamforming and more specifically delay and sum beamforming [Urick 1983]. Delay and Sum Beamforming is the summing of the independent receivers of an array to form a beam pattern. It is the interference of the plane wave from the individual receivers that give the beam pattern its shape (see chapter 1). First consider an acoustic plane wave.

$$P = P_0 e^{-i(\omega t - k r_n)} \tag{3.24}$$

P is the pressure, ω is the radian frequency, t is time, k is the wavenumber, and r_n is the range to the target from the n^{th} receiver. The phase of the plane wave is

$$\varphi_n = \omega t - k r_n \tag{3.25}$$

The phase change between receivers of a uniformly spaced linear array (ULA) is referred to as the phase **delay**

$$\Delta\varphi_n = k\Delta r_n = 2\pi \frac{d}{\lambda} sin\theta \tag{3.26}$$

k is the wavenumber, Δr_n is the change in range for the n^{th} receiver, d is the distance between receivers, λ is the wavelength of the signal, and θ is the arrival angle of the acoustic plane wave. The output voltage of the n^{th} receiver with voltage response R_n is

$$V_n = R_n e^{-in\varphi} \tag{3.27}$$

The output voltage for the whole array will be the **sum** of all the receivers.

$$V = \sum_{n=1}^{n} R_n e^{-i(\omega t - n\varphi)} \tag{3.28}$$

$$V = \left(R_0 + R_1 e^{-i(\varphi)} \ldots + R_n e^{-i(n\varphi)}\right) e^{-i(\omega t)} \tag{3.29}$$

Assume a uniform response where all R_n's are equal, so the *R's* can be dropped. Set the temporal component $e^{-i\omega t}$ aside for now. The voltage response for the array is in the form of a Maclaurin series and can be approximated as

$$V = \frac{e^{-i(n\varphi)} - 1}{e^{-i(\varphi)} - 1} e^{-i(\omega t)} \approx \frac{\sin\left(\frac{n\varphi}{2}\right)}{\sin\left(\frac{\varphi}{2}\right)} \tag{3.30}$$

Square the voltage and normalize by the number of receivers to obtain the beam pattern.

$$b(\theta) = \left(\frac{V}{n}\right)^2 = \left(\frac{\sin\left(n\,\pi \frac{d}{\lambda} sin\theta\right)}{\mathrm{n}\,\sin\left(\pi \frac{d}{\lambda} sin\theta\right)}\right)^2 \tag{3.31}$$

It is obvious that the beam pattern is in the form of a sinc function (see chapter 1). Similarly, the beam pattern for a two-dimensional array is

$$b(\theta) = \left(\frac{V}{mn}\right)^2 = \left[\frac{\sin\left(n\,\pi \frac{d_x}{\lambda} sin\theta\right)}{n\,\sin\left(\pi \frac{d_x}{\lambda} sin\theta\right)}\right]\left[\frac{\sin\left(m\pi \frac{d_y}{\lambda} cos\theta sin\phi\right)}{m\,\sin\left(\pi \frac{d_y}{\lambda} cos\theta sin\phi\right)}\right] \tag{3.32}$$

Increasing the distance between receivers results in a wider beam pattern. Decreasing the distance between receivers results in spatial aliasing and sidelobes. Increasing the number of receivers will make the beam width narrower. Hence, the reason for the development of a synthetic aperture sonar array with a large number of virtual receivers. When the receivers of the array are close together the array becomes a continuous line array and the

voltages can be integrated over the length of the aperture instead of summed. Let *R/D* be the response per unit length *dv,* for the aperture distance *D*.

$$dV = \frac{R}{D} e^{i\left(2\pi\frac{x}{\lambda}sin\theta\right)} dx \tag{3.33}$$

$$V = \frac{R}{D}\int_{-\frac{D}{2}}^{\frac{D}{2}} e^{i2\pi\frac{v}{\lambda}sin\theta} dv = \frac{R}{i2\pi\frac{D}{\lambda}sin\theta}\left[e^{i\left(\pi\frac{D}{\lambda}sin\theta\right)} - e^{-i\left(\pi\frac{D}{\lambda}sin\theta\right)}\right] \tag{3.34}$$

Using Euler's identity and the sinc function as before the voltage response for a continuous array is

$$V = R\frac{sin\left(\pi\frac{D}{\lambda}sin\theta\right)}{\pi\frac{D}{\lambda}sin\theta} = R\ sinc\left(\frac{D}{\lambda}sin\theta\right) \tag{3.35}$$

The beam pattern is

$$b(\theta) = \left(\frac{V}{R}\right)^2 = \left[sinc\left(\frac{D}{\lambda}sin\theta\right)\right]^2 \tag{3.36}$$

The wavenumber bandwidth is

$$B_{k_v} = \frac{2\pi}{D} \tag{3.37}$$

The ½ power point on the main axis of the beam θ_{3dB} = *-3dB*.

$$\theta_{3dB} = \alpha_w \frac{2\pi}{kD} = \frac{\lambda}{D} \tag{3.38}$$

The beam pattern has a main lobe along the x-axis and the smaller lobes are referred to as side lobes.

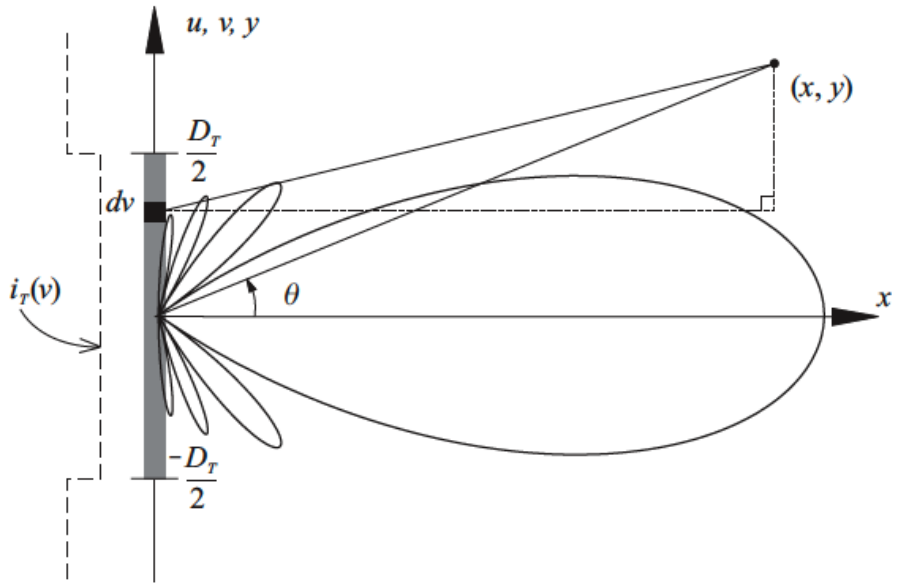

Figure 3.4 The radiation pattern of the transmitted waveform: The radiation pattern of the transmitted waveform: $i_t(v)$ is the intensity, D is the aperture length, dv is the increment of the aperture, and θ is the direction to the point of measurement (x, y) [Gough & Hawkins 96].

3.6.2 Beam Steering

The main beam of the beam pattern is located at the center of the array extending out perpendicular to the array. The beam angle will be referred to as θ and it is optimized at $\theta = 0°$, which is perpendicular to the array. The beam can be pointed in other directions by adding time delays to the transducer elements. This technique is known as beam steering. Steering the beam away from broadside (squinting) distorts the beam pattern with maximum distortion occurring at endfire $\theta = \pm 90°$. Not to be confused with the tilt angle, the mechanical angle at which the SAS array is pointed to the seafloor. Beam pattern of a one-dimensional array with steering angle θ_0 is

$$b(\theta) = \left(\frac{V}{n}\right)^2 = \left[\frac{sin\left(\frac{n\pi d_x}{\lambda}(sin\,\theta - sin\theta_0)\right)}{n\,sin\left(\frac{\pi d_x}{\lambda}(sin\,\theta - sin\theta_0)\right)}\right]^2 \tag{3.39}$$

The beam pattern of a two-dimensional array with steering angle is

$$\left[\frac{sin\left(\frac{n\pi d_x}{\lambda}(sin\,\theta - sin\theta_0)\right)}{n\,sin\left(\frac{\pi d_x}{\lambda}(sin\,\theta - sin\theta_0)\right)}\right]\left[\frac{sin\left(\frac{m\pi d_y}{\lambda}(cos\theta sin\varphi - cos\theta_0 sin\varphi_0)\right)}{m\,sin\left(\frac{\pi d_y}{\lambda}(cos\theta sin\varphi - cos\theta_0 sin\varphi_0)\right)}\right] \tag{3.40}$$

3.6.3 Array Theory

Consider Figure 3.4 the signal received at a point *(x,y)* from a radiating aperture of length *D* where *dv* is the increment of the aperture. The acoustic response of the array also referred to as the aperture function is

$$h_T(x,y,t) \approx \int_{-D/2}^{D/2} \frac{i_t(v)}{\sqrt{x^2+(y-v)^2}} P_m(t)dv \tag{3.41}$$

$P_m(t)$ is the transmit pulse, and $i_t(v)$ is the intensity. A Fast Fourier Transforms (FFT) is used to transfer the aperture function into the frequency domain

$$h_T(x,y,t) \approx \int_{-D/2}^{D/2} \int \frac{i_t(v)}{\sqrt{x^2+(y-v)^2}} P_m(t)e^{-i\omega t}dtdv \tag{3.42}$$

Thus, given the beam pattern function

$$H_T(x,y,\omega) \approx P_m(\omega)\int_{-D/2}^{D/2} i_t(u)\frac{e^{-ik\sqrt{x^2+(y-v)^2}}}{\sqrt{x^2+(y-v)^2}}\,dv \tag{3.43}$$

It is necessary to reference everything to the center of the real aperture by transforming the range into *k* space, where k_v is the Doppler wavenumber. The mapping from domain *(ω, v)* to the *(k_x, k_y)* is non-linear.

$$\int e^{-i2k\sqrt{x^2+(y-v)^2}}e^{-ik_v v}dv \approx \sqrt{\frac{\pi x}{ik}}e^{-i\sqrt{4k^2-k_u^2}x - ik_v y} = A_1 e^{i\psi(k_v)} \tag{3.44}$$

Transform the spatial domain *v* into *k* space and using the principle of stationary phase to solve the above integral (see appendix 3). The wavenumber k_x and k_y is

$$k_x(\omega,k_v) = \sqrt{4k^2-k_v^2} \qquad k_y(\omega,k_v) = k_v \tag{3.45}$$

The distance between wavenumbers is 2k.

$$k_v = 2k\ sin\theta = \frac{2ky}{\sqrt{x^2+y^2}} \qquad 2k = \sqrt{k_x^2 + k_y^2} \tag{3.46}$$

The aspect angle θ from the center of the array to position *(x, y)* is.

$$\theta = sin^{-1}\left(\frac{y}{\sqrt{x^2+y^2}}\right) \qquad \theta = tan^{-1}\left(\frac{(y-v)}{x}\right) \tag{3.47}$$

$$H_T(x,y,\omega) \approx P_m(\omega)\int_{-D/2}^{D/2} i_T(v) \times \int_{-k}^{k} \frac{e^{-i\sqrt{(k^2-k_v^2)}x - ik_v(y-v)}}{\sqrt{k^2-k_v^2}}\, dk_v dv \tag{3.48}$$

$$H_T(x,y,\omega) = P_m(\omega)\int_{-k}^{k}\left\{\int_{-D/2}^{D/2} i_T(v)e^{ik_v v}dv\right\} \times \frac{e^{-i\sqrt{(k^2-k_v^2)}x - ik_v y}}{\sqrt{k^2-k_v^2}}\, dk_v \tag{3.49}$$

$$H_T(x,y,\omega) = P_m(\omega)\int_{-k}^{k} I_T(k_v)\frac{e^{-i\sqrt{(k^2-k_v^2)}x - ik_v(y)}}{\sqrt{k^2-k_v^2}}\, dk_v \tag{3.50}$$

The $I_T(k_v)$ is the amplitude and phase of the illumination function. The amplitude pattern scales to the spatial domain as

$$I_T(k_v) = \int_{-\infty}^{\infty} A_T(k_v)e^{-i\,\varphi k_v}dk_v \tag{3.51}$$

$$H_T(x,y,\omega) \approx P_m(\omega)\int_{-k}^{k} A_T(k_v)\,\frac{e^{-i\sqrt{(k^2-k_v^2)}x - ik_v(y)}}{\sqrt{k^2-k_v^2}}\, dk_v \tag{3.52}$$

The amplitude pattern scales from the k_v wavenumber domain to the spatial domain.

$$A_t(,x,y,\omega) = A_T(k_v) \tag{3.53}$$

The amplitude pattern is the sinc function as illustrated in Figure 3.4.

$$A_T(k_v) = sinc\left(\frac{k_v D}{2\pi}\right) \qquad A_T(x,y,\omega) = sinc\left(\frac{kDsin\theta}{2\pi}\right) \tag{3.54}$$

Take the IFFT to obtain the impulse response of the aperture.

$$a(x,y,t) = \int A_t(,x,y,\omega)e^{i\,\omega t}d\omega \tag{3.55}$$

Take the IFFT to obtain the spatial-temporal response of the aperture function

$$h_T(x,y,t) = \frac{1}{\sqrt{x^2+y^2}}P_m(t)a_T(x,y,t)\delta\left(t - \frac{\sqrt{x^2+(y-u)^2}}{c}\right) \tag{3.56}$$

The last term in Eq. (3.56) is the point spread function (PSF).

$$\delta\left(t - \frac{2}{c}\sqrt{x_0{}^2+u^2} - x_0\right)e^{-i\frac{2\omega_c}{c}\sqrt{x_0{}^2+u^2}-x_0} \tag{3.57}$$

The point spread function can be interpreted using the quadratic approximation to the range migration locus. Similarly based on the principle of reciprocity the sensitivity pattern of the detecting aperture for a target at point (x,y) is

$$H_R(x,y,\omega) = P_m(\omega)A_T(x,y,\omega) \times A_R(x,y,\omega)\frac{e^{-i2k\sqrt{x^2+y^2}}}{x^2+y^2} \tag{3.58}$$

The *2k* in the exponent comes from the instantaneous Doppler frequency being twice the rate of a single aperture. SAS systems use a time varying gain (TVG) or Automatic Varying Gain (AVG) to compensate for the loss due to spherical spreading $1/R^2$, therefore the denominator can be dropped. The sensitivity pattern then becomes.

$$H_R(x,y,\omega) = P_m(\omega)A_T(x,y,\omega) \times A_R(x,y,\omega)e^{-i2k\sqrt{x^2+y^2}} \tag{3.59}$$

Take the IFFT to obtain the transmit a_t and receive a_r amplitude response. The received echo from the seafloor is

$$ee_m(t,u) \approx \iint ff(x,y)\left(a_t(x,y-u,t)a_r(x,y-u,t) \times p_m\left(t-\frac{2}{c}\sqrt{x^2+(y-u)^2}\right)\right)dxdy \tag{3.60}$$

ff(x,y) is the reflectivity of the target and p_m is the LFM chirp, *u* is the position of the vehicle moving in the along-track direction. Transform the temporal domain echo into the frequency domain.

$$Ee_m(\omega,u) \approx p_m(\omega)\iint ff(x,y)\,A_t(x,y-u,\omega)A_r(x,y-u,\omega)e^{-i2k\sqrt{x^2+(y-u)^2}}dxdy \tag{3.61}$$

Transform the spatial domain *u* into *k* space. The temporal frequency Doppler wavenumber domain echo from the seafloor is

$$EE_m(\omega,k_u) \approx p_m(\omega)A(k_u)\iint ff(x,y)\sqrt{\frac{\pi x}{ik}}\,e^{-i\sqrt{4k^2-k_u^2}x-ik_u(y)}dxdy \tag{3.62}$$

3.7 Synthetic Aperture Sonar Signal Processing

Some preliminary signal processing techniques are common to SAS processing. First step is to zero mean and normalize the data by subtracting the mean from the data prior to signal processing and dividing by the number of samples. Zero padding in the time domain provides for ideal interpolation into the frequency domain. This is accomplished by adding zeros at the end of the signal to make it a multiple of powers of two. It is also necessary to account for the propagation loss by compensating the signal in the time domain by the use of a time varying gain (TVG) by multiplying the signal by $-20\log R=1/R^2$. The SAS data typically arrives basebanded , pulse compressed and transformed into the frequency domain. The steps for basebanding and pulse compression are as follows.

3.7.1 Basebanding

The signal is basebanded by removing the carrier frequency. This technique is also referred to as demodulating the signal.

$$ee_b(t,u) = ee_m(t,u)e^{-i\omega_0 t} \tag{3.63}$$

ee_m is the modulated received echo from the seafloor, ω_0 is the center frequency and *t* is the time.

Expansion of the received signal

$$ee_b(t,u) \approx \iint ff(x,y)\left(a_t(x,y-u,t)p_b\left(t-\frac{2}{c}\sqrt{x^2+(y-u)^2}\right)\right)e^{\frac{-i2k_0\sqrt{x^2+(y-u)^2}}{c}}dxdy \tag{3.64}$$

Transform into the temporal-frequency domain then baseband. The signal becomes

$$Ee_b(\omega_b,u) \approx P_b(\omega_b)\iint ff(x,y)\,A(x,(y-u),\omega_b+\omega_0)e^{-i2(k_b-k_0)\sqrt{x^2+(y-u)^2}}dxdy \tag{3.65}$$

3.7.2 Pulse Compression

The dilemma is short pulses are better for range resolution and long pulses are better for signal reception. Pulse compression is a solution that satisfies the dilemma. Energy content of long duration, low power pulses will be comparable to that of the short duration high power pulse. Pulse compression is a matched filtering technique used to enhance the range resolution and signal to noise ratio.

$$ss_b(t,u) \approx \int p_b(\tau-t)^H ee_b(\tau-t)\,d\tau = p_b(t)ee_b(t,u) \tag{3.66}$$

p_b is the basebanded transmit pulse, and ee_b is the basebanded echo. Pulse compression is accomplished by multiplying the outgoing signal by the echo return signal, then transform into the temporal-frequency domain. The Pulse compressed spatial domain expression is

$$Ss_m(\omega_b,u) = |P_m(\omega)|^2\iint ff(x,y)\,A(\omega,x,y-u)\,e^{-i2k\sqrt{x^2+(y-u)^2}}\,dxdy \tag{3.67}$$

The basebanded pulse compressed signal is

$$Ss_b(\omega_b,u) = |P_b(\omega_b)|^2\iint ff(x,y)\,A(\omega,x,y-u)\,e^{-i2k\sqrt{x^2+(y-u)^2}}\,dxdy \tag{3.68}$$

Solve the integral using the principle of stationary phase (see appendix 3) to obtain the pulse compressed signal

$$Ss_b(\omega_b,u) \approx \frac{1}{\sqrt{K_0}}A(x,y-u,\omega)rect\left(\frac{\omega_b}{2\pi K_0\tau_0}\right)\,e^{-i2(\omega_b+\omega_0)R} \tag{3.69}$$

Along-track convolution causes the target responses in the pulse compressed raw data to spread in the along-track direction.

$$ss_\delta(t,x_0) \approx \iint \left(a_t(x_0,u,t)\delta\left(t-\frac{2}{c}\sqrt{x_0^2+u^2}-x_0\right)\right) e^{-i2k_0\sqrt{x_0^2+u^2}} \tag{3.70}$$

Shifting the function to the origin and ignoring the aperture effects gives the PSF necessary for focusing

$$pp(t,u,x_0) = \delta\left[t-\frac{2}{c}\sqrt{x_0^2+u^2}-x_0\right] e^{-i2k_0\sqrt{x_0^2+u^2}-x_0} \tag{3.71}$$

$$pp(t,u,x_0) = \delta\left[t-\frac{2}{c}\Delta R(u,x_0)\right] e^{-i2k_0\Delta R(u,x_0)} \tag{3.72}$$

The range migration locus of the echoed signal is

$$\Delta R(u,x_0) = \sqrt{x_0^2+u^2}-x_0 \tag{3.73}$$

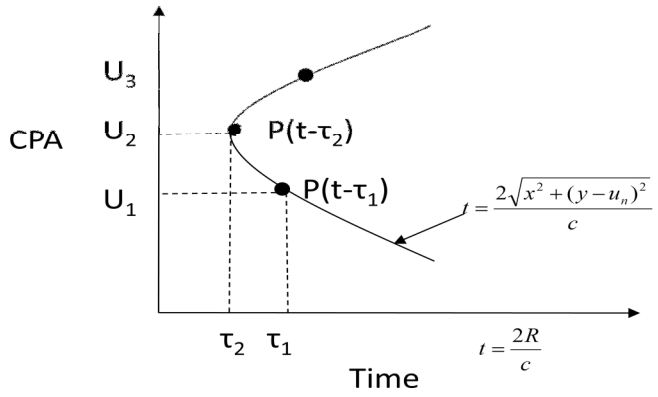

Figure 3.5 The range migration locus of the echoed signal.

The quadratic approximation to the range migration locus to determine the spatial Doppler bandwidth is

$$pp(t,u,x) \approx \delta\left[t-\frac{u^2}{cx_0}\right] e^{-i2k_0\frac{u^2}{x_0}} \tag{3.74}$$

The instantaneous Doppler wavenumber is

$$k_{ui}(u) = \frac{d\varphi}{du} \approx \frac{2k_0}{x_0} u = 2\pi K_a u \tag{3.75}$$

The spatial chirp rate disperses the target in the along-track direction

$$K_a \approx \frac{k_0}{\pi x_0} \tag{3.76}$$

The null-to-null radiation pattern of the aperture has an along-track extend at range

$$Y_0 \approx 2x_0 \frac{\lambda_0}{D} = \frac{4\pi x_0}{k_0 D} \tag{3.77}$$

The wavenumber bandwidth of the along-track signal

$$B_{k_u} \approx 2\pi K_a Y_0 = \frac{8\pi}{D} \tag{3.78}$$

The along-track resolution

$$\delta_{y3dB} = \alpha_\omega \frac{2\pi}{B_p} = \frac{D}{2} \tag{3.79}$$

The across-track resolution is

$$\delta_{x3dB} = \frac{c}{2B_c} \tag{3.80}$$

The wide bandwidth version of the focusing filter function for a target at range x_0 is

$$BB(\omega, k_u) \approx \sqrt{\frac{k}{k_0}} e^{-i\left(\sqrt{4k^2 - k_u^2} - 2k\right)x_0} \tag{3.81}$$

3.8 StripmapSAS Image Reconstruction

The previous sections laid the groundwork for the synthetic aperture image processing techniques presented in this section. The first two techniques presented do not require motion compensation (see chapter two). They are time-domain-backprojection and fast-factored-back-projection. The ω-k and chrip scaling techniques require *a priori* motion compensation. The backprojection techniques are well suited for research because there are less approximations making the image reconstruction more precise. However, this comes at the expense of computational load. The ω-k and chrip-scaling have faster processing times, at the expense of image degradation. These methods are presented here along with range-Doppler that is mostly used in the SAR community along with Raney's range -Doppler that eliminated the need for Stolt mapping. Raney's method led to the development of chirp-scaling. The beauty of chrip scaling is that it is phase preserving.

3.8.1 Time Domain Backprojection

The backprojection algorithm enables perfect image reconstruction for any trajectory or array configuration along as there is a good estimate of the bottom topography.

Transmit pulse is

$$p\left[t - \frac{2\sqrt{x_i^2 + \left(y_j - u\right)^2}}{c}\right] \tag{3.82}$$

Image of the scene

$$ff\left(x_i, y_j\right) = \iint ss(t,u)p^H\left[t - \frac{2\sqrt{x_i^2 + \left(y_j - u\right)^2}}{c}\right]dtdu \tag{3.83}$$

The time delay for the target at point *(i, j)*

$$t_{ij}(u) = \frac{2\sqrt{x_i^2 + \left(y_j - u\right)^2}}{c} \tag{3.84}$$

Simplify by substitute Eq. (3.83) into Eq. (3.82) to obtain the image reflectivity

$$ff(x_i, y_j) = \iint ss(t,u)p^H[t - t_{ij}]dtdu \tag{3.85}$$

Often the data is stored as a pulse compressed basebanded signal in the frequency domain. Using Parseval's Theorem where the energy in the time domain is equivalent to the energy in the frequency domain. The received signal in Eq. (3.84) can be written as follows.

$$\int ss(t,u)p^H[t - t_{ij}]dt = \int Ss_b(\omega_b, u)\, P_b^H(\omega_b)e^{i\omega t_{ij}(u)}\, dt \tag{3.86}$$

The received signal is then basebanded and transformed into the temporal-frequency spatial domain

$$Ss_b(\omega_b, k_u) = P_b^H(\omega_b)A^H(\omega, k_u)Ss_b(\omega_b, k_u) \tag{3.87}$$

The temporal-frequency domain of the scene image is

$$ff(x_i, y_j) = \int_{\omega_{min}}^{\omega_{max}} \int_{y_j - B_{i(\omega_b)}}^{y_j + B_{i(\omega_b)}} Ss_b(\omega_b, u)a^H(\omega, x_i, y_j - u)\, P_b^H(\omega_b)e^{i\omega t_{ij}(u)}\, d\omega du \tag{3.88}$$

The modulated signal in the time domain is

$$S_m(t\,, u) = Ss_b(t,u)P_b^H(t) \tag{3.89}$$

The bandwidth is

$$B_{i(\omega_b)} = x_i \tan\phi_d \tag{3.90}$$

The backprojection algorithm for the scene is

$$ff(x_i, y_j) = \int_{y_j - B_{i(\omega_b)}}^{y_j + B_{i(\omega_b)}} S_m(t_{ij}(u)\,, u)du \tag{3.91}$$

Time domain backprojection is best suited for algorithm development instead of surveys because it is so computationally intensive. This led to the development of approximations to the beamforming techniques to reduce the computational load, so the algorithms could be loaded into a chip on the vehicle and processed in real time. The gain in computational time comes at the expensive of a degraded image.

3.8.2 Fast-Factorization-Backprojection FFBP& Fast-Polar-Back-Projection FPBP

This is a recursive partitioning of the backprojection integral. FFBP is a phase preserving inversion method and is therefore suitable for producing interferometric sonar images [Yegulalp 1999] [Banks & Griffith 2003] [Shippey et al. 2005]. Further research by Callow contradicts this claim. He states, the approximation causes image artifacts and incorrect height in interferometry. Interferometry has shown to be more sensitive to FFBP approximation error than wavenumber domain imagery due to its phase sensitivity [Callow et al. 2006]. Its usefulness is in the ability to scan a large area in less time than conventional methods with the ability to pick out targets that can be reprocessed at a higher resolution.

The Time Domain signal

$$F_0(t,u) = \frac{1}{R^2} e^{i2\pi f_c\left(t-\frac{2R}{c}\right)} sinc\left(B_w\left(t-\frac{2R}{c}\right)\right) \tag{3.92}$$

This notation easily lends itself to account for the motion offsets and various array configurations. Start with transforming the signal to the frequency domain and apply a ramp filter to account for the frequency loss at the higher frequencies of the band. This step can be skipped if the assumption of a dispersionless medium is used.

$$\hat{F}(f,u) = F_0(t,u)|f| \tag{3.93}$$

The intensity of the image pixel in the discrete form for the pixel location is

$$ff(\vec{p}) = \sum_{k=1}^{M} F\left(\frac{2}{c}|\vec{p} - \vec{q}(u_k)|, u_k\right) du_k \tag{3.94}$$

ff(x,y) is the image scene, *p* is the position vector of the target and *q* is the position vector of the receiver. The geometry lends itself to simple processing in polar coordinates. The intensity of the image pixel in the continuous form is

$$ff(\vec{p}) = \int_{-\infty}^{\infty} F\left(\frac{2}{c}|\vec{p} - \vec{q}(u)|, u\right) du \tag{3.95}$$

In FFBP the computation is conducted on a pulse by pulse basis allowing for parallel processing of the above equation. The carrier phase is removed by basebanding then the signal is upsampled prior to using the principle of stationary phase for integration. The integration limits are reduced to a fixed angle for each center point pixel θ_1 and θ_2.

$$\cos\theta_2 \leq \frac{(\vec{p} - \vec{q}(u))\vec{q}(u)'}{|\vec{p} - \vec{q}(u)|} \leq \cos\theta_1 \tag{3.96}$$

FFBP works by dividing the full synthetic aperture into subapertures. An image is produced for each subaperture. To obtain the higher resolution image upsample in the cross-track direction prior to combining the subaperture images. Start the process by breaking the full aperture image into subapertures of length $l = L/N_{subap}$.

$$ff(\vec{p}) = \sum_{n=1}^{N_{subap}} I_n(\vec{p}) \tag{3.97}$$

The center of the n[th] subaperture is given by $s_n = (n-1/2)l$

$$ff(\vec{p}) = \int_{-\frac{l}{2}}^{\frac{l}{2}} F\left(u_n + \xi, \frac{2}{c}|\vec{p} - \vec{q}(u_n + \xi)|\right) d\xi \tag{3.98}$$

ξ is the cross range of the pixel.

3.8.3 Wavenumber (seismic migration or range migration)

Analyzers of InSAS imagery are interested in the location of the target. Therefore, it becomes important to move to the spatial domain. This is often referred to ω-k or wavenumber processing. The name comes from omega being the traditional symbol for radial frequency ω and the wavenumber k. Start with the basebanded data padded with zeros to the next power of two, pulse compress and perform a two-dimensional FFT to transform into the (ω, k_u) domain, then map it into the(kx, ky) domain to have an evenly spaced grid. This last step is referred to as Stolt mapping [Stolt 1978] [Hawkins 1996].

The received echo from the seafloor is

$$ee_m(t,u) \approx \iint ff(x,y)\left(a_t(x,y-u,t)a_r(x,y-u,t) \times p_m\left(t-\frac{2}{c}\sqrt{x^2+(y-u)^2}\right)\right)dxdy \tag{3.99}$$

Transform the temporal domain echo into the frequency domain.

$$Ee_m(\omega,u) \approx p_m(\omega)\iint ff(x,y)\,A_t(x,y-u,\omega)A_r(x,y-u,\omega)e^{-i2k\sqrt{x^2+(y-u)^2}}dxdy \tag{3.100}$$

Transform the spatial domain *u* into *k* space and solve using the principle of stationary phase.

$$A_1 e^{i\psi(k_u)} = \int e^{-i2k\sqrt{x^2+(y-u)^2}}e^{-ik_u u}du \approx \sqrt{\frac{\pi x}{ik}}e^{-i\sqrt{4k^2-k_u^2}x-ik_u y} \tag{3.101}$$

The temporal frequency Doppler wavenumber domain echo from the seafloor is

$$EE_m(\omega,k_u) = \sqrt{\frac{\pi}{ik}}p_m(\omega)A(k_u)\iint ff(x,y)\sqrt{x}\,e^{-i\sqrt{4k^2-k_u^2}x-ik_u y}dxdy \tag{3.102}$$

The two-dimensional FFT into the wavenumber domain is

$$k_x(\omega,k_u) = \sqrt{4k^2-k_u^2} \tag{3.103}$$

$$k_y(\omega,k_u) = k_u \tag{3.104}$$

The non-linear mapping referred to as Stolt mapping is represented by the Jacobian $JJ(k_x,k_y)$

$$JJ(k_x,k_y) = \frac{ck_x}{2\sqrt{k_x^2+k_y^2}} \approx \frac{c}{2} \tag{3.105}$$

Apply Stolt mapping $S\{\}$

$$EE_m(\omega,k_u) \approx \sqrt{\frac{\pi}{ik}}p_m(\omega)A(k_u)S\{FF_x(k_x,k_y)\} \tag{3.106}$$

Forward Stolt mapping is

$$\omega(k_x, k_y) \equiv \frac{c}{2}\sqrt{k_x^2 + k_y^2} \tag{3.107}$$

$$k_u(k_x, k_y) = k_y \tag{3.108}$$

Which maps the wavenumber k_x and k_y into the measurement parameters ω and k_u by using the Jacobian $JJ(\omega, k_u)$

$$JJ(\omega, k_u) = \frac{4k}{c\sqrt{4k^2 - k_u^2}} \approx \frac{2}{c} \tag{3.109}$$

Perform a Stolt IFFT to obtain the Spectral image estimate

$$FF_m(k_x, k_y) = WW(k_x, k_y) S^{-1}\left\{\sqrt{\frac{k}{k_0}} P_m^H(\omega) EE_m(\omega, k_u)\right\} \tag{3.110}$$

$$FF_m(k_x, k_y) = WW(k_x, k_y) S^{-1}\left\{\sqrt{\frac{k}{k_0}} SS_m(\omega, k_u)\right\} \tag{3.111}$$

The window function $WW(k_x,k_y)$ is used to extract the range and along-track processing bandwidths and sidelobe reduction. Redefine the temporal origin to be centered on range r_0, $t' = t - 2r_0/c$. Output range origin is $x' = x - r_0$. This step is necessary to shift the x origin back to the center.

$$\begin{aligned} ee_m(t', u) \approx \iint ff(x', y)\, a_t\left(t' + \frac{2r_0}{c}, x' + r_0, y - u\right) p_m\left(\left(t' + \frac{2r_0}{c}\right)\right. \\ \left. - \frac{2}{c}\sqrt{(x' + r_0)^2 + (y - u)^2}\right) dx'dy \end{aligned} \tag{3.112}$$

$$EE'_m(\omega, k_u) = \sqrt{\frac{\pi}{ik}} p_m(\omega) A(k_u) e^{i2kr_0} \iint ff(x', y)\, e^{-i\sqrt{4k^2 - k_u^2}(x' + r_0) - ik_u y} dx'dy \tag{3.113}$$

$$EE'_m(\omega, k_u) = \sqrt{\frac{\pi}{ik}} p_m(\omega) A(k_u) e^{-i\left(\sqrt{4k^2 - k_u^2} - i2k\right) r_0} S\{FF'_x(k_x, k_y)\} \tag{3.114}$$

The wavenumber inversion with phase defined relative to r_0

$$\widehat{FF'_m}(k_x, k_y) = WW(k_x, k_y) S^{-1} \left\{ \sqrt{\frac{k}{k_0}} e^{-i\left(\sqrt{4k^2 - k_u^2} - i2k\right) r_0} P_m(\omega) EE'_m(\omega, k_u) \right\} \tag{3.115}$$

$$\widehat{FF'_m}(k_x, k_y) = WW(k_x, k_y) S^{-1} \left\{ \sqrt{\frac{k}{k_0}} e^{-i\left(\sqrt{4k^2 - k_u^2} - i2k\right) r_0} SS'_m(\omega, k_u) \right\} \tag{3.116}$$

The most efficient way to implement the wavenumber inversion is on the basebanded signal because the data set is smaller for both the FFT and the Stolt interpolator

$$\widehat{FF'_b}(k_x, k_y) = WW(k_x, k_y) {S_b}^{-1} \left\{ \sqrt{\frac{k}{k_0}} e^{-i\left(\sqrt{4k^2 - k_u^2} - i2k\right) r_0} P_b(\omega_b) EE'_b(\omega_b, k_u) \right\} \tag{3.117}$$

The weighting function chosen is a rect and a two-dimensional Hamming which lowers the sidelobes by -13dB.

$$WW(k_x, k_y) = rect\left(\frac{k_y}{Bk_y}\right) \frac{1}{A(k_y)} W_h\left(\frac{k_x}{Bk_x}\right) W_h\left(\frac{k_y}{Bk_y}\right) \tag{3.118}$$

The wavenumber bandwidths of the extracted data is

$$Bk_x = \sqrt{4k_{max}^2 - \left(\frac{2\pi}{D}\right)^2} - 2k_{min} \approx \frac{4\pi B_c}{c} - \frac{2\pi^2 B_c}{k_{max} D^2} \tag{3.119}$$

$$Bk_y = \frac{4\pi}{D} \tag{3.120}$$

The final image resolution for wavenumber domain is

$$\delta_{x3dB} = \frac{2\pi}{B_{k_x}} = \alpha_\omega \frac{c}{2B_{eff}} \quad B_{eff} \approx \frac{\pi c}{2k_{max}D^2} \tag{3.121}$$

$$\delta_{y3dB} = \frac{2\pi}{B_{k_y}} = \alpha_\omega \frac{D}{2} \tag{3.122}$$

Other window functions are in appendix 2, but for now I will apply the simplest the rect function window. The baseband version of the spectral estimate using a rectangular window is

$$\widehat{FF'}_b(k_x, k_y) = \sqrt{\frac{\pi}{ik_0}} rect\left(\frac{k_x}{Bk_x}\right) rect\left(\frac{k_y}{Bk_y}\right) FF'_x(k_x, k_y) \tag{3.123}$$

The basebended reflectivity of the scene

$$\begin{aligned} \left|\widehat{ff'}_b(x', y)\right| &= \left|\mathcal{F}^{-1}_{k_x,k_y}\left\{\widehat{FF'}_b(k_x, k_y)\right\}\right| \\ &= \sqrt{\frac{\pi}{ik_0}}\left(\frac{Bk_x}{2\pi}\right)\left(\frac{Bk_y}{2\pi}\right) sinc\left(\frac{Bk_x}{2\pi}x\right) sinc\left(\frac{Bk_y}{2\pi}y\right) ff'_x(x', y) \end{aligned} \tag{3.124}$$

Shifting back to the x- axis

$$\left|\widehat{ff}_b(x, y)\right| = \sqrt{\frac{\pi x}{ik_0}}\left(\frac{2B_{eff}}{c}\right)\frac{2}{D} sinc\left(\frac{2B_{eff}}{c}x\right) sinc\left(\frac{2}{D}y\right) ff(x, y) \tag{3.125}$$

The synthetic aperture improvement factor is seen to be

$$IF_{SA} = 20log_{10}\sqrt{\frac{\pi x}{k_0}}\frac{2}{D} \tag{3.126}$$

This factor is the space bandwidth product of the along-track chirp

$$K_A L_{SA} = \frac{k}{\pi x}\left(\frac{x\lambda}{D}\right)^2 = \frac{4\pi x}{kD^2} \tag{3.127}$$

Or the improvement factor of *N* along-track samples

$$N = \frac{L_{SA}}{\Delta_u} = \frac{4\pi x}{kD^2} \tag{3.128}$$

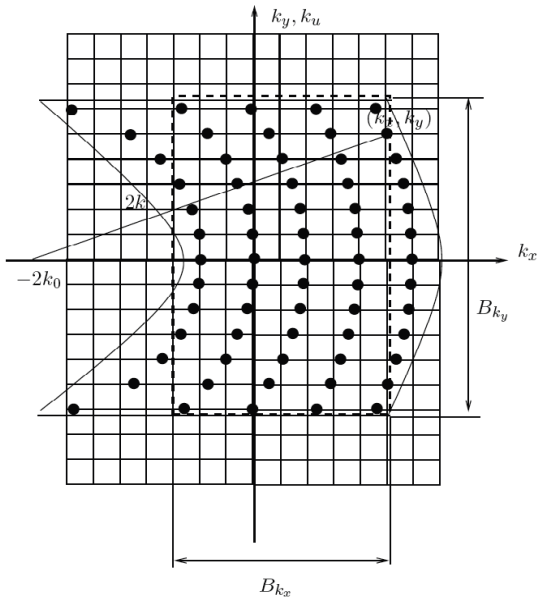

Figure 3.6 The two-dimensional collection surface of the wavenumber data.The heavy dots indicate the location of the raw data samples along radii *2k* at height k_u. The underlying rectangular grid shows the format of the samples after mapping (interpolating) to a Cartesian grid on (k_x, k_y). The spatial bandwidths Bk_x and Bk_y outline the rectangular section of the wavenumber data that is extracted, windowed and IFFT to produce the image estimate. The slightly offset nature of the mapped basebanded data appears as an irrelevant phase factor in the spatial domain. This phase factor does not effect the final image estimate $ff_b(x,y)$.

3.8.4 Chirp-scaling

Chirp-scaling is a very good choice for InSAS because it preserves the phase. Chirp-scaling requires the transmit signal to be a LFM chirp. Chirp-scaling is a method of curvature equalization where no grid interpolation is required similar to the Raney's Range-Doppler (see Appendix 8). After wavenumber transformation the range migration trajectories have been adjusted to have congruent loci, equivalent to the trajectory at a selected reference range [Runge and Bamler1992] [Raney et al. 1994]. Along-track FFT of the range-Doppler signal of the PSF is

$$pp(t,u,x_0) = \delta\left[t - \frac{2}{c}\sqrt{x_0^2+u^2} - x_0\right] e^{-i2k_0\sqrt{x_0^2+u^2}-x_0} \tag{3.129}$$

$$eE_b(t,k_u) = \mathcal{F}_u\{ee_b(t,u)\} \tag{3.130}$$

$$eE_b(t,k_u,x_0) = \sqrt{\frac{x_0\pi}{ik_0}}A(k_u)rect\left(\frac{t-\frac{2}{c}R_s(k_u;x_0)}{\tau_c}\right)e^{i\pi K_s(k_u;x_0)\left[t-\frac{2}{c}R_s(k_u;x_0)\right]^2}e^{-i\sqrt{4k_0^2-k_u^2}x_0} \quad (3.131)$$

The k_u dependent chirp rate or scaled chirp rate is

$$K_s(k_u;r_0) = \frac{1}{\frac{1}{K_c - K_{src}(k_u;r_0)}} \quad (3.132)$$

Range dependent chirp term secondary range compression (SRC) is

$$K_{src}(k_u;r_0) = \frac{8\pi r_0}{c^2}\frac{k_u^2}{(4k_0^2-k_u^2)^{\frac{3}{2}}} \quad (3.133)$$

Transform to the range-Doppler domain. The range-Doppler domain is then perturbated by a phase multiplier that causes all the phase centers of the reflected chirps to have a range migration locus that is identical to the reference range r_0.

$$mM_b(t,k_u) = \mathcal{F}_t\{eE_b(t,k_u)\varphi\Phi_1(t,k_u)\} \quad (3.134)$$

Where the chirp-scaling multiplier is

$$\varphi\Phi_1(t,k_u) = e^{i\pi K_s(k_u;r_0)C_s(k_u)[t-t_0(k_u)]^2} \quad (3.135)$$

So the range migration phase terms of all scatterers are equalized to that of a scatterer at reference r_0.

$$\varphi(t) = i\pi K_s(k_u;r_0)\left(t-\frac{2}{c}x[1+C_s(k_u)]\right)^2 + \pi K_s(k_u;r_0)C_s(k_u)\left(t-\frac{2}{c}x[1+C_s(k_u)]\right)^2 - \omega_b t \quad (3.136)$$

$$\varphi(t) = i\pi K_s(k_u;r_0)[1+C_s(k_u)]t^2 - \left\{\frac{4\pi}{c}K_s(k_u;r_0)[1+C_s(k_u)][x+r_0C_s(k_u)] + \omega_b\right\}t + \left\{\frac{4\pi}{c^2}K_s(k_u;r_0)[1+C_s(k_u)]^2[x+r_0^2C_s(k_u)]\right\} \quad (3.137)$$

Where K_s is the chrip rate, C_s is the curvature, and the wavenumber dependent reference time is the time locus of the reference range. The curvature factor is

$$C_s(k_u) = \sqrt{1 - \left(\frac{k_u}{2k_u}\right)^2} - 1 \tag{3.138}$$

$$t_0(k_u) = \frac{2}{c} r_0[1 + C_s(k_u)] \tag{3.139}$$

The application of the range variant chirp-scaling multiplier is easily applied in the range-Doppler domain where range is a parameter. The wavenumber algorithm removes the range variant nature of the system equations in the two-dimensional wavenumber domain where range is not available as a parameter. The chirp scaled data is then temporal Fourier transformed to the two-dimensional wavenumber domain. The range migration loci of all targets now follow the same reference curvature, however, the chirp-scaling operation induces a further Doppler dependence in the range chirp. Pulse compression, including secondary range compression, bulk range migration correction, deconvolution of the frequency dependent amplitude term and windowing are performed across the bandwidth by

$$NN_b(k_x, k_y) = WW(k_x, k_y) C^{-1}\{MM_b(\omega_b, k_u)\Theta\Theta_2(\omega_b, k_u)\} \tag{3.140}$$

The phase multiplier simultaneously applies range correction, compression and secondary range compression. This is known as azimuthal range compression

$$\Theta\Theta_2(\omega_b, k_u) = \sqrt{\frac{k}{k_0}} e^{i\left\{\frac{{\omega_b}^2}{4\pi K_c(k_u; r_0)[1 + C_s(k_u)]}\right\}} e^{i2k_b r_0 C_s(k_u)} \tag{3.141}$$

The transform C^{-1} in Eq.(3.140) is

$$k_x(\omega_b, k_u) \equiv \frac{2\omega_b}{c} \tag{3.142}$$

$$k_y(\omega_b, k_u) \equiv k_u \tag{3.143}$$

The range-Doppler of the image is obtained by taking the IFFT in range

$$fF_b(x,k_y) = nN_b(x,k_y)\psi\Psi_3(x,k_y) \tag{3.144}$$

Where the along-track compression and residual phase compensation is performed by the phase multiplier

$$\psi\Psi_3(x,k_y) = e^{\left(\sqrt{4k_0^2-k_u{}^2}-2k_0\right)x_0} e^{i\frac{4\pi}{c^2}K_s(k_y;r_0)C_s(k_y)[1+C_s(k_y)](x-r_0)^2} \tag{3.145}$$

The final complex image estimate is

$$ff_b(x,y) = F_{k_y}^{-1}\{F_{k_x}^{-1}WW(k_x,k_y)C^{-1}F_t\{eE_b(t,k_u)\varphi\Phi_1(t,k_u)\}\Theta\Theta_2(\omega_b,k_u)\}\psi\Psi_3(x,k_y) \tag{3.146}$$

The chirp-scaling multiplier neglects the range dependence of K_s. The range-Doppler uses a Taylor series expansion to approximate the Stolt interpolation. These errors are small and will have to be accounted for in the interferometric height determination. The accelerated chirp-scaling is the chirp-scaling algorithm above, with the addition of a preliminary pulse compression step.

3.9 Adaptive filters

Operationally we have multiple frequencies, varying angles of incidence, non-homogenous environments, multiple signals, low signal to noise ratios, and most importantly signals whose properties change with time. With that in mind it is realized that our simple solution may not be very effective. It is now time to focus our attention on the implementation of adaptive filters. The key word being adaptive – the ability to adjust to change. In the specific case of this dissertation the change in signal to noise properties and most importantly direction of arrival for interferometric signal processing. Adaptive filters operate on the principle of filtering the input and minimizing the error function between the desired output and the signal. The difference in these adaptive filters is in the design of the weighting and the approach to minimizing the error [Haykin 2001].

3.9.1 MATCHED FIELD MFP

The generalized Matched Field Processing beamformer measures the acoustic field at the array. The replica signal is a solution to the Helmholtz wave equation for a particular environment. First step is to calculate the acoustic field by creating a replica signal from a propagation model for each point on the gridded field. The replica signal will be a function of angle, range and depth. The environmental parameters considered will be surface interaction, bottom characteristics and sound velocity for each receiver of the array. The modeled acoustic field is then correlated with the received signal to find the range, bearing and depth of the received signal. Environmental mismatches will degrade the performance of the processor. MFP provides improvements in SNR due to array gain and rejecting sidelobe noise. By resolving the position in depth you are able to separate the surface noise from the subsurface

noise.

$$P_{cv}(\hat{a}) = |m^H(\hat{a})s(a_T)|^2 + m^H(\hat{a})Qm(\hat{a}) \tag{3.147}$$

m is the steering vector with angle, range and depth, *S* is the replica signal, and *Q* is the noise vector . The replica signal as a function of depth.

$$S(z_r) = \left[1 - e^{i2\pi\frac{\Delta r}{\lambda}}\right] e^{i2\pi\frac{\Delta z \sin\varphi}{\lambda}} = 2sin\left(\frac{2\pi z_s \Delta z_r}{r\lambda}\right) e^{i\frac{2\pi(z_s - z_r)^2}{r\lambda} + z_s z_r} e^{-i\frac{\pi}{2\lambda}} \tag{3.148}$$

Δr is the change in range, r is the range, λ is the wavelength, Δz is the change in depth, z_s is the depth of the source, z_r is the depth of the receiver.

3.9.2 Wiener Solution

The Wiener solution is the first and simplest of the adaptive filters. It is a linear discrete time filter whose output *y(n)* provides an estimate of a desired response *d(n)* , given a set of input samples *x(n),* such that the mean square value of the estimation error *e(n)* , defined as the difference between the desired response *d(n)* and the actual response *y(n)*, is minimized. The filter input is the time series *x(n)* and the filter response is *w(k).* The filter output at discrete time *(n)* is the linear convolution sum [Haykin 2001].

$$y_n = \sum_{n=0}^{N-1} W_k^H x_{(n-k)} \tag{3.149}$$

The assumption is that the input and the desired response are single realizations of jointly wide sense stationary ergodic stochastic processes. The estimation error e_n is

$$e_n = d_n - y_n \tag{3.150}$$

To optimize the filter design, minimize the mean square value of e_n. J is the cost function. It is the mean square error (MSE). The requirement is to determine the operating condition in which the cost function obtains its minimum value.

$$\mathcal{J} = E|e_n|^2 \tag{3.151}$$

Apply the gradient operator with respect to the filter coefficient *w(k)* to the cost function *J*. Optimize by setting *J*

equal to zero, the stationary point.

$$\nabla_{\mathrm{k}}\mathcal{J} = -2E|x(n-k)e_n^H| = 0 \tag{3.152}$$

Let e_0 denote the special value of the estimation error that results when the filter operates in its optimum condition.

$$E|x(n-k)e_0^H| = 0 \tag{3.153}$$

The condition in which the cost function attains its minimum value, is for e_0 to be orthogonal to each input sample that enters into the estimation of the desired response at time n. This is referred to as the Principle of Orthogonality. It states that the error vector of the optimal estimator is orthogonal to any possible estimator. Using the Principle of Orthogonality, the expectation is

$$E|y_n e_n^H| = \sum_{k=0}^{\infty} W_k^H \, E\left|x_{(n-k)}e_n^H\right| \tag{3.154}$$

The corollary is when the filter operates in its optimum condition, the estimate of the desired response defined by the filter output y_0 and the corresponding estimation error e_0 are orthogonal to each other.

$$E|y_0 e_0^H| = 0 \tag{3.155}$$

The estimation error for the optimized filter output becomes.

$$e_o = d_n - y_0 \tag{3.156}$$

$$d_n = e_0 + y_0 \tag{3.157}$$

Let J_{min} be the minimized mean square error.

$$\mathcal{J}_{min} = E|e_o|^2 \tag{3.158}$$

Using the corollary to the Principle of Orthogonality

$$\sigma_d^2 = \sigma_y^2 + \mathcal{J}_{min} \tag{3.159}$$

σ_d^2 is the variance of the desired signal and σ_y^2 is the variance of the estimated noise. Solving for the minimum square error

$$\mathcal{J}_{min} = \sigma_d^2 - \sigma_y^2 \tag{3.160}$$

Normalize J_{min} by dividing through by σ_d

$$\frac{\mathcal{J}_{min}}{\sigma_d^2} = 1 - \frac{\sigma_y^2}{\sigma_d^2} \tag{3.161}$$

Now let

$$\mathcal{E} = \frac{\mathcal{J}_{min}}{\sigma_d^2} \tag{3.162}$$

This is the normalized mean square error is

$$\mathcal{E} = 1 - \frac{\sigma_y^2}{\sigma_d^2} \qquad 0 \leq \mathcal{E} \leq 1 \tag{3.163}$$

3.9.3 Recursive Least Mean Square

Recursive Least Mean Square (RLS) algorithms are also known as transversal filters. The RLS is an extension of the Least Mean Square (LMS) filter with a faster rate of convergence. Its key features are the forgetting factor λ and the use of the Matrix Inversion Lemma (see appendix A4). The inversion lemma allows for the update vector to be inverted and appended to the autocorrelation matrix *R* vice inverting the whole matrix for every update. The forgetting factor is really a nice feature because signals and noises are transient, therefore it will forget the signals that have already passed by [Haykin 2001]. The cost function is minimized as

$$\mathcal{J}_n = \sum_{i=1}^{n} \beta(n,i)|e(i)|^2 \tag{3.164}$$

J_n is the cost function, β_n is the weighting factor often referred to as the forgetting factor,

$$\beta(n,i) = \lambda^{n-i} \qquad 0 \leq \beta(n,i) \leq 1 \tag{3.165}$$

n is the variable length of the observable data at time i, e_i is the difference between desired response d_i and the filter output y_i , which is the weight w_n of the impulse filter at time n, and x_i the input vector at time i.

$$e_i = d_i - y_i = d_i - w_n^H x_i \tag{3.166}$$

The cost function is somewhat ill-posed and it would be better to expand the cost function to be minimized as the sum of two components

$$\mathcal{J}_n = \sum_{i=1}^{n} \lambda^{n-i} |e(i)|^2 + \delta\lambda^n |w(n)|^2 \tag{3.167}$$

This is the sum of the weighted error squared

$$\sum_{n=1}^{n} \lambda^{n-i} |e(i)|^2 = \sum_{i=1}^{n} \lambda^{n-i} |d_i - w_n^H x_i|^2 \tag{3.168}$$

The regularization term is

$$\delta\lambda^n |w(n)|^2 = \delta\lambda^n w_n^H w_n \tag{3.169}$$

The regularization parameter δ is used to stabilize the solution to the recursive least-squares problem by smoothing the solution. Expanding the cost function to a time average correlation matrix

$$\mathbf{\Phi}_n = \sum_{i=1}^{n} \lambda^{n-i} x_i \, x_i^H + \delta\lambda^n I \tag{3.170}$$

Φ_n is nonsingular. This matrix is said to be diagonally loaded. The cross correlation vector between the tap inputs and the transversal filter and the desired response is unaffected by the use of regularization.

$$z_n = \sum_{i=1}^{n} \lambda^{n-i} x_i \, d_i^H \tag{3.171}$$

The Normal equation (orthogonal)

$$\boldsymbol{\Phi}_n w_n = z_n \tag{3.172}$$

Recursive computation of Φ_n and z_n

$$\boldsymbol{\Phi}_n = \lambda \left[\sum_{i=1}^{n-1} \lambda^{n-1-i} x_i \, x_i^H + \delta \lambda^{n-1} I \right] + x_n x_n^H \tag{3.173}$$

The correlation matrix is

$$\boldsymbol{\Phi}_{n-1} = \left[\sum_{i=1}^{n-1} \lambda^{n-1-i} x_i \, x_i^H + \delta \lambda^{n-1} I \right] \tag{3.174}$$

The recursion for updating the value of the correlation matrix of the tap inputs is

$$\boldsymbol{\Phi}_n = \lambda \boldsymbol{\Phi}_{n-1} + x_n x_n^H \tag{3.175}$$

Similarly the recursion for updating the cross correlation vector between the tap inputs and the desired response is

$$z_n = \lambda z_{n-1} + x_n d_n^H \tag{3.176}$$

Here we will be able to apply the Matrix Inversion Lema to compute the least squares estimate of the weights w_n. The matrix inversion lema also known as the Woodbury Identity is one of the most eloquent features of matrix algebra (see appendix A4).

$$\boldsymbol{\Phi}_{\mathrm{n}}^{-1} = \lambda \boldsymbol{\Phi}_{\mathrm{n-1}}^{-1} - \frac{\lambda^{-2} \boldsymbol{\Phi}_{\mathrm{n-1}}^{-1} x_n x_{\mathrm{n}}^{\mathrm{H}} \boldsymbol{\Phi}_{\mathrm{n-1}}^{-1}}{1 + \lambda^{-1} x_{\mathrm{n}}^{\mathrm{H}} \boldsymbol{\Phi}_{\mathrm{n-1}}^{-1} x_n} \tag{3.177}$$

For simplicity let P be the inverse cross correlation matrix

$$\mathbf{P}_n = \mathbf{\Phi}_{\mathrm{n}}^{-1} \tag{3.178}$$

and the gain vector k_n

$$\mathrm{k}_n = \frac{\lambda^{-1}\mathbf{P}_{\mathrm{n}-1}x_n}{1+\lambda^{-1}x_{\mathrm{n}}^{\mathrm{H}}\mathbf{P}_{\mathrm{n}-1}x_n} \tag{3.179}$$

Thus, the Riccati equation for the RLS algorithm

$$\mathbf{P}_n = \lambda^{-1}\mathbf{P}_{\mathrm{n}-1}x_n - \lambda^{-1}\mathrm{k}_n x_{\mathrm{n}}^{\mathrm{H}}\mathbf{P}_{\mathrm{n}-1} \tag{3.180}$$

Rearranging the gain vector to obtain

$$\mathrm{k}_n = \lambda^{-1}\mathbf{P}_{\mathrm{n}-1}x_n - \lambda^{-1}\mathrm{k}_n x_{\mathrm{n}}^{\mathrm{H}}\mathbf{P}_{\mathrm{n}-1}x_n \tag{3.181}$$

$$\mathrm{k}_n = [\lambda^{-1}\mathbf{P}_{\mathrm{n}-1} - \lambda^{-1}\mathrm{k}_n x_{\mathrm{n}}^{\mathrm{H}}\mathbf{P}_{\mathrm{n}-1}]x_n \tag{3.182}$$

Since

$$\mathbf{P}_n = [\lambda^{-1}\mathbf{P}_{\mathrm{n}-1} - \lambda^{-1}\mathrm{k}_n x_{\mathrm{n}}^{\mathrm{H}}\mathbf{P}_{\mathrm{n}-1}] \tag{3.183}$$

$$\mathrm{k}_n = \mathbf{P}_n x_n \tag{3.184}$$

Then the gain vector becomes

$$\mathrm{k}_n = \mathbf{\Phi}_{\mathrm{n}}^{-1}x_n \tag{3.185}$$

Now it is time to update the weight vector

$$\mathrm{w}_n = \boldsymbol{\Phi}_{\mathrm{n}}^{-1}\mathrm{z}_n = \mathbf{P}_n\mathrm{z}_n \tag{3.186}$$

$$\mathrm{w}_n = \lambda\mathbf{P}_n\mathrm{z}_{n-1} + \mathrm{P}_n x_n d_{\mathrm{n}}^{\mathrm{H}} \tag{3.187}$$

$$\mathrm{w}_n = \mathbf{P}_{n-1}\mathrm{z}_{n-1} - \mathrm{k}_n x_{\mathrm{n}}^{\mathrm{H}}\mathbf{P}_{n-1}\mathrm{z}_{n-1} + \mathbf{P}_n x_n d_{\mathrm{n}}^{\mathrm{H}} \tag{3.188}$$

$$\mathrm{w}_n = \boldsymbol{\Phi}_{\mathrm{n}-1}^{-1}\mathrm{z}_{n-1} - \mathrm{k}_n x_{\mathrm{n}}^{\mathrm{H}}\boldsymbol{\Phi}_{\mathrm{n}-1}^{-1}\mathrm{z}_{n-1} + \mathbf{P}_n x_n d_{\mathrm{n}}^{\mathrm{H}} \tag{3.189}$$

$$\mathrm{w}_n = \mathrm{w}_{n-1} - \mathrm{k}_n x_{\mathrm{n}}^{\mathrm{H}}\mathrm{w}_{n-1} + \mathbf{P}_n x_n d_{\mathrm{n}}^{\mathrm{H}} \tag{3.190}$$

The equation for updating the weight vector is

$$\mathrm{w}_n = \mathrm{w}_{n-1} + \mathrm{k}_n[d_{\mathrm{n}}^{\mathrm{H}} - x_{\mathrm{n}}^{\mathrm{H}}\mathrm{w}_{n-1}] \tag{3.191}$$

Let ξ be the *a priori* estimation error where the inner product is

$$\xi_{\mathrm{n}} = d_{\mathrm{n}} - x_{\mathrm{n}}^{\mathrm{T}}\mathrm{w}_{n-1}^{\mathrm{H}} = d_{\mathrm{n}} - \mathrm{w}_{n-1}^{\mathrm{H}}x_{\mathrm{n}} \tag{3.192}$$

$$\mathrm{w}_n = \mathrm{w}_{n-1} + \mathrm{k}_n\xi_{\mathrm{n}}^{\mathrm{H}} \tag{3.193}$$

Where the *a posteriori* estimation error is

$$e_n = d_n - w_n^H x_n \tag{3.194}$$

3.9.4 Eigenvalue deconvolution

The cross spectral density matrix CSDM is an ensemble average of the source response taking over the array. The time span for the average is chosen that the sources are statistically and linearly independent. The noise is independent of the source. We can assume the noise subspace is orthogonal to the signal subspace.

$$\boldsymbol{R} = \sum_{i=1}^{M} \lambda_i \nu_i \nu_i^H \tag{3.195}$$

$$Rv_i = \lambda_i v_i \tag{3.196}$$

$$\boldsymbol{R} = \sum_{i=1}^{P} \sigma_i \, s_i s_i^H + \sigma_n^2 I \tag{3.197}$$

There are *p* signal sources therefore there are *M-p* eigenvectors that are orthogonal to the signal vector space. If we assume white noise the noise vector is proportional to the identity matrix and has zero mean. Additional gains are made by using eigenvector deconvolution prior to beam steering and minimum variance processing. In beam steering we can truncate the CSDM by not using the noise subspace. This is done by scanning the space with the replica vectors resulting in sharp peaks at the source location.

The inverse vector R^{-1} has the same eigenvectors of the CSDM. Therefore we can truncate the CSDM by not including the source subspace. The replica scanning causes a null in the source location. The minimum variance (MV) prescription of the inverse process is infinite at source location and finite otherwise. Resulting in a high resolution of the source location.

3.9.5 Maximum Likelihood or Minimum Variance Distortionless Response MVDR

The minimum variance distortionless response method often referred to as the maximum likelihood method ML developed by Capon is based on the separation of signal and noise space by eigenstructure decomposition of the estimated covariance matrix. Capon realized that the sum and delay method was inadequate at separating the signal from the ambient noise in a high density noise environment. The weight vector in MVDR is chosen to minimize the variance (average power) of the beamformer output subject to the constraint $W^H{}_m S(\theta) = 1$ by means of the Lagrangian multiplier. Where $S(\theta)$ is the direction of arrival. This constrained minimization yields an adaptive beamformer with a minimum variance distortionless response [Burdic 1990] [Jensen et al. 1994].

$$y(i) = \sum_{t=0}^{M} w_t^H \, x(i-t) \tag{3.198}$$

w_t^H are the weights of the filter and x is the input signal.

The output energy of this system is

$$\mathcal{J} = \sum_{i=M+1}^{N} |y(i)|^2 \tag{3.199}$$

Subject to the constraint

$$\sum_{k=0}^{M} w_n^H \, e^{-ik\theta} = 1 \tag{3.200}$$

θ is the steering vector similarly this can also be used in the frequency domain by substituting ω_0 for θ. k is the number of filter coefficients. The output energy of the system or cost function constrained by the Lagrange multiplier is

$$\mathcal{J} = \sum_{i=M+1}^{N} |y(i)|^2 + \gamma \left(\sum_{k=0}^{M} w_k^H \, e^{-ik\theta} - 1 \right) \tag{3.201}$$

γ is the Lagrange multiplier which is a function of the constraint. To optimize the system take the gradient of the output energy and set it equal to zero

$$\nabla_{\mathrm{k}} \mathcal{J} = 2 \sum_{i=M+1}^{N} x(i-k) y^H(i) + \gamma^H e^{-ik\theta} = 0 \tag{3.202}$$

$$\nabla_{\mathrm{k}} \mathcal{J} = 2 \sum_{t=0}^{M} w_t \sum_{i=M+1}^{N} x(i-k) x^H(i-t) + \gamma^H e^{-ik\theta} = 0 \tag{3.203}$$

R is the spatial covariance matrix from the autocorrelation of the input signal and noise.

$$R = \sum_{t=0}^{M} \sum_{i=M+1}^{N} x(i-k) x^H(i-t) \tag{3.204}$$

Substitute R into Eq. (3.299)

$$\nabla_{\mathrm{k}} \mathcal{J} = 2 \sum_{t=0}^{M} w_t \, \mathrm{R(t,k)} + \gamma^H e^{-ik\theta} = 0 \tag{3.205}$$

$$\sum_{t=0}^{M} w_t \, \mathrm{R(t,k)} \; = \frac{1}{2}\left(\gamma^H e^{-ik\theta}\right) \tag{3.206}$$

In matrix form let the steering vector by $s(\omega_0)$

$$w \, \mathrm{R} = \frac{1}{2}\gamma^H s(\theta) \tag{3.207}$$

Solve for the lagrangian multiplier using the condition of constraint

$$w^H s(\theta) = 1 \tag{3.208}$$

$$\gamma^H = \frac{-2}{w^H R^{-1} w} \tag{3.209}$$

Solve for the weight applying by substituting for the Lagrange multiplier to obtain the optimum solution to the MVDR or equivocally the MVDR estimate

$$w = \frac{R^{-1}s(\theta)}{s^H(\theta)R^{-1}s(\theta)} \tag{3.210}$$

The aperture function for the array is

$$g_{mv} = \frac{R^{-1}w}{w^H R^{-1} w} \tag{3.211}$$

The power average output

$$P_{mv} = g_{mv}^H R g_{mv} = \frac{w^H R^{-1} R R^{-1} w}{(w^H R^{-1} w)^2} = \frac{1}{w^H R^{-1} w} \tag{3.212}$$

Assuming the noise is isotropic the improvement in power using the MVDR method over conventional methods is 2:1. Capon found that with K independent temporal samples to estimate the noise covariance matrix for a N receiver array is:

$$\frac{\sigma_{P_{mv}}^2}{E_{P_{mv}}^2} = \frac{1}{K - N + 1} \tag{3.213}$$

This beamformer is constrained to produce a distortionless response along the look direction corresponding to φ_0. In other words, the optimum beamformer is constrained to pass the target signal with unit response, while at the same time minimizing the total output variance. This variance minimization process attenuates interference and noise not originating at the angle φ_0 of the source.

$$B_{mv}(\theta_s) = [w^H(\theta_s)K^{-1}(\theta_{true})w(\theta_s)]^{-1} \tag{3.214}$$

One of the main advantages of this method is a narrow beamwidth, with no sidelobes which will provide a better bearing estimate. The second advantage is its ability to separate two closely spaced targets.

3.9.6 MUSIC

Multiple Signal Classification uses eigenvalue decomposition where the noise subspace is orthogonal to the signal. The noise subspace is set equal to unity (prewhitening the CSDM) was developed by [R.O. Schmidt 1977] and simultaneously developed by [Bienvenu 1979] from [Pisarenko 1973] work in subspace harmonic decomposition.

$$s^H(\theta_k)v_n = 0 \tag{3.215}$$

For a given steering vector *k*. for any steering vector *s(θ)*. Expand the above relationship to

$$s^H(\theta_k)V_nV_n^Hs(\theta_k) = 0 \quad for\ \theta = \theta_1 \ldots \theta_p \tag{3.216}$$

Where V_n is a complex matrix composed the last *M-p* eigenvectors of the covariance matrix corresponding to the noise subspace. Then the theoretical direction of arrival can be found by searching the null values of the above product. Unfortunately the true covariance matrix is unknown and must be estimated from

$$R_x(t) = \frac{1}{N}\sum_{t=1}^{N} y(t)y^H(t) \tag{3.217}$$

The eigen decomposition of $R_x(t)$ provides an estimation of the true eigenvalues vectors given

$$R_x(t) = V_s\Lambda_s V_s^H + V_n\Lambda_n V_n^H \tag{3.218}$$

Since the signal and noise subspace are based on the estimated covariance matrix decomposition, a localization function $f(\theta)$ is created, providing null values at or in the immediate neighborhoods of the true directions of arrival.

$$f_{music}(\theta) = s^H(\theta)V_nV_n^Hs(\theta) \tag{3.219}$$

Another approach is to invert the above equation and search for the maximum

$$g_{music}(\theta) = \frac{1}{as^H(\theta)V_nV_n^Hs(\theta)} = \frac{1}{\sum_{i=p+1}^{N-D}|s^Hv_i|^2} \tag{3.220}$$

v_i are the noise eigenvectors. MUSIC produces a number of angular peaks equal to D. If D is too large then there will be extra peaks that do not correspond to the plane wave of interest. If D is two small only the largest peak response will be displayed. If $D = 0$ then the result will be the same as the mimimum variance response.

In order to have a proper estimation, the number of independent realizations should be high. If not it could result in the covariance matrix being singular. A common solution is to split the receiving data into several subvectors and filter leaving a smoothed version of the covariance matrix.

$$R_x = SR_xS^H + \sigma_n^2 I = \sum \lambda_k\, e_k e_k^H \tag{3.221}$$

$$D = SR_xS^H + \sigma_n^2 I = \sum \lambda_k\, e_k e_k^H \tag{3.222}$$

The frequency estimation function for music or power response

$$P_{mu}(e^{i\omega}) = \frac{1}{\sum_{i=p+1}^{N-D}|s^Hv_i|^2} \tag{3.223}$$

$$S = \begin{bmatrix}1 & e^{i\omega} & e^{i2\omega} & e^{i(M-1)\omega}\end{bmatrix}^T \tag{3.224}$$

3.9.7 Root MUSIC

$$f_{music}(\theta) = s^H(\theta) V_n V_n^H s(\theta) = 0 \tag{3.225}$$

$$V = \begin{bmatrix} 1 & z^{-1} & z^{-2} & z^{-(M-1)} \end{bmatrix}^T \tag{3.226}$$

$$\mathrm{z} = e^{\frac{2\pi \mathrm{d}}{\lambda} \sin\theta} \tag{3.227}$$

The roots of f_{music} will provide the direction of arrivals that are not quite on the unit circle.

3.9.8 ESPRIT

Estimation of Signal Parameters via Rotational Invariance Technique ESPRIT is a subspace algorithm derived by Roy in 1989. The algorithm exploits the rotational invariance among signal subspaces induced by an array of sensors with a translational invariance structure. There is a Least Squares method LS and a Total Least Squares method TLS. The TLS-ESPRIT is described here. Consider a uniform linear array of *N* receivers. The first step is to find two identical subarrays with N_s receivers and $N_s > D$ number of plane wave sources.

$$x(t) = Gs(t) + n(t) \qquad G = [a(\theta_1) \ldots a(\theta_d)] \tag{3.228}$$

Where $a(\theta)$ is the array response in direction θ. Now consider a selection of matrices J_p that are a subset of the array with the following rotational invariant structure

$$J_0 G = A, \quad J_1 G = A\Phi, \quad J_p G = A\Phi^{\mathrm{P}} \tag{3.229}$$

Φ is a unitary diagonal matrix with diagonal receivers

$$\phi_{\mathrm{i}} = e^{i2\pi \frac{\mathrm{d}\sin\theta_{\mathrm{i}}}{\lambda}} \qquad i = 1 \ldots d \tag{3.230}$$

$$R_x = G R_x G^H + \sigma_n^2 I \tag{3.231}$$

The covariance matrix of the signal vector is of full rank *d* and the columns of the response function *G* are linearly independent. The eigen decomposition of the covariance matrix results in

$$R_x = U\Sigma U^H = U_s \Sigma U_s^H + \sigma_n^2 U_n U_n^H \tag{3.232}$$

Where U_s is the eigen value signal subspace and U_n is the eigen value subspace of the noise. That span { U_s } = span {G}. This implies the existence of a *d x d* full rank matrix *T*, satisfying $U_s = GT$. The signal subspace corresponding to the subarrays defined by { $U_i = J_i U_s$ i = 0 … p } .

$$U_i = A\Phi^{\mathrm{i}}\mathrm{T} = \mathrm{B}\Psi^{\mathrm{i}} \tag{3.233}$$

Where B = AT and $\Psi = \mathrm{T}^{-1}\Phi\mathrm{T}$

$$U_i = A\Phi^{\mathrm{i}}\mathrm{T} = U_i\Psi^{\mathrm{i}} \tag{3.234}$$

Now apply the TLS to obtain an estimate of U_i

$$U_i = A\Phi^{\mathrm{i}}\mathrm{T} = \mathrm{B}\Psi^{\mathrm{i}} \tag{3.235}$$

3.9.9 Bayesian Beamformer [Lasenby & Fitzgerald 1991][Bell et al. 2000]

The Bayesian beamformer is an extension of the MVDR method. The Bayesian approach is to perform the conventional MVDR beamformer on a number of direction of arrival candidates with a specified angular range and then balances multiple outputs according to the *a posteriori* probability density function (PDF) that describes the likelihood of the true direction of arrival. When the number of observed data samples increases the likelihood function becomes more accurate and eventually converges to an impulse on the DOA that has the largest likelihood. The resulting beamformer is able to adapt to the true DOA given that the true DOA lies on one of these candidate points.

$$P(\theta_i|X) = \frac{P(\theta_i)P(X|\theta_i)}{\sum_{i=1}^{L} P(\theta_i)P(X|\theta_i)} \quad i = 1,2 \ldots L \tag{3.236}$$

Where $p(X|\theta_i)$ is the PDF of the data given θ_i

$$P(X|\theta_i) = \prod_{k=1}^{K} \frac{1}{\pi^n |R_x(\theta_i)|} \; e^{-iX(t_k)^H R_x(\theta_i) X(t_k)} \tag{3.237}$$

$$P(X|\theta_i) = \pi^{NK}|R_x(\theta_i)|^{-K}\ e^{-\sum_{k=1}^{K} X(t_k)^H {R_x}^{-1}(\theta_i)X(t_k)} \tag{3.238}$$

The determinant has the form

$$|R_x(\theta_i)| = |R_n|(1 + \sigma_s^2 a(\theta_i)^H {R_n}^{-1} a(\theta_i)) \tag{3.239}$$

Expanding and using the matrix inversion lemma (see appendix 4)

$$|R_x^{-1}(\theta_i)| = R_x^{-1} - \frac{\sigma_s^2 {R_n}^{-1} a(\theta_i)^H a(\theta_i) {R_n}^{-1}}{(1 + \sigma_s^2 a(\theta_i)^H {R_n}^{-1} a(\theta_i))} \tag{3.240}$$

The *a posteriori* PDF is

$$P(\theta_i|X) = c\ P(\theta_i)\left(1 + \sigma_s^2 \beta(\theta_i)\right)^K\ e^{\left(\frac{k\sigma_s^2\beta(\theta_i)^2}{1+\sigma_s^2\beta(\theta_i)}\right)\left(\frac{a(\theta_i)^H {R_n}^{-1} \widehat{R_K} {R_n}^{-1} a(\theta_i)}{(\beta(\theta_i)^2)}\right)} \tag{3.241}$$

C is the normalization factor to ensure the pdf sums to one

$$\beta(\theta_i) = a(\theta_i)^H {R_n}^{-1} a(\theta_i) \tag{3.242}$$

The *a posteriori* probability of the true DOA will approach one, whereas the *a posteriori* probabilities of the other DOA will approach zero.

Summary

This chapter presented the basic beamforming techniques necessary to produce a SAS image. The SAS image will be used in the next section on interferometry. The adaptive beamforming techniques have been presented here to lay the groundwork for future InSAS work. The basic principles of these techniques will be applied to find the direction of arrival from the phase information of the interferometry.

Chapter 4 Interferometry

4.1 Interferometry

Interferometry was developed by Michelson & Morley in the 1880's to detect the aether. The technique has been modified and applied to Synthetic Aperture Sonar (SAS) systems and is referred to as Interferometric Synthetic Aperture **S**onar (InSAS). InSAS systems measure the phase difference between a pair of sonar arrays to derive the direction of arrival to obtain the bathymetric height. InSAS systems are limited by ambiguities caused by the phase wrapping around 2π. The goal of InSAS signal processing is to develop an accurate estimate of the unwrapped phase that is suitable to estimate the bathymetric height to create precise three-dimensional imagery of the seafloor. InSAS is possible because transmit and receive signals are coherent and they have a measureable time delay and phase. Figure 4.1 is the system geometry for an InSAS system.

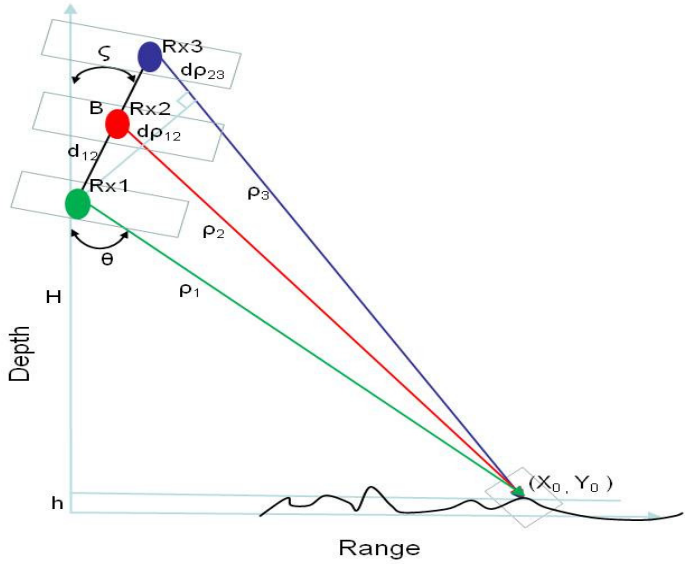

Figure 4.1 The geometry of an InSAS system with three arrays receiving data from a patch of seafloor. (X_0, Y_0) is the patch on the seafloor, B is the baseline, H is the altitude of the AUV from the seafloor, h is the estimate of the change in seafloor height. Rx_1, Rx_2 and Rx_3 are the receiver arrays, d_{12} is the distance between Rx_1 and Rx_2, d_{23} is the distance between Rx_2 and Rx_3, ρ_1, ρ_2, and ρ_3 are the path lengths and $d\rho_{12}$ and $d\rho_{23}$ are the respective phase differences, θ is the direction of arrival, and ς is the tilt angle of the array.

InSAS Signal processing begins with the received coherent backscattered acoustic energy of an ensonified patch of seafloor on two vertically separated arrays. The backscattered acoustic energy is filtered and beamformed to produce a complex image of the scene (see chapter 3 for details). The pressure for a backscattered acoustic plane wave is

Array 1
$$P_1(x_0, y_0) = a_1 \iint ff(x,y)\, W(x - x_0, y - y_0) e^{i2k_0\rho_1 - \omega t} dxdy \tag{4.1}$$

Array2 $$P_2(x_0, y_0) = a_2 \iint ff(x,y)\, W(x - x_0, y - y_0) e^{i2k_0\rho_2 - \omega t} dxdy \tag{4.2}$$

P_1 and P_2 are the pressure from the acoustic plane wave for the reflected point (x_0, y_0) on the ground plane for array 1 and array 2, a_1 and a_2 are the amplitudes of the plane wave, (x,y) is the position of the receiver, $ff(x, y)$ is the reflectivity distribution of the target scene, $W(x-x_0, y-y_0)$ is the system impulse response, $e^{i2k_0\rho_1 - \omega t}$ is the spatial phase for the received signal where the *two* is for the two way travel time, k_0 is the wavenumber, ρ_1 is the slant range, and ωt is the angular frequency.

4.1.1 Phase difference

The measured phase difference between seafloor images from two separate arrays can be obtained by taking the phase difference from the cross correlation of the two complex images, thus forming the interferogram.

$$\Delta\varphi = angle(P_1 P_2^H) \tag{4.3}$$

Simplifying Eq. (4.1) and Eq. (4.2) to its magnitude and phase components

$$P_1 = A_1 e^{i(2k_0\rho_1)} \tag{4.4}$$

$$P_2 = A_2 e^{i(2k_0\rho_2)} \tag{4.5}$$

Cross correlation of P_1 and P_2 leads to

$$P_1 P_2^H = A_1^2 + A_2^2 + 2A_1 A_2 e^{i(2k_0(\rho_2 - \rho_1))} \tag{4.6}$$

The change in phase occurs in the third term of Eq. (4.6)

$$\Delta\varphi = angle(P_1 P_2^H) = 2k_0(\rho_2 - \rho_1) \tag{4.7}$$

Where range ρ_2 is equivalent to ρ_1 plus the phase difference.

$$\rho_2 = \rho_1 + \frac{\lambda\Delta\varphi}{2\pi} \tag{4.8}$$

the change in phase $\Delta\varphi$ can also be expressed as a function of the direction of arrival θ (see chapter 1).

$$\Delta\varphi = k_0(\rho_2 - \rho_1) = \frac{2\pi b}{\lambda} cos(\theta + \varsigma) \tag{4.9}$$

The cosine of the direction of arrival and tilt angle can also be expressed as a sine function of the steering angle less the direction of arrival because the steering angle θ_s is perpendicular to the tilt angle ς, $\theta_s = (\varsigma - \pi/2)$.

$$cos(\theta + \varsigma) = sin(\theta_s - \theta) \tag{4.10}$$

$$\Delta\varphi = k_0(\rho_2 - \rho_1) = \frac{2\pi b}{\lambda} sin(\theta_s - \theta) \tag{4.11}$$

The phase is measured from *0 to* 2π, much like an analog clock measures time from *0* to *12* hours. As range increases the phase difference will become greater then π and will jump or wrap around to $-\pi$. Figure 4.2 shows the phase difference collected in the cross-track direction increases with range.

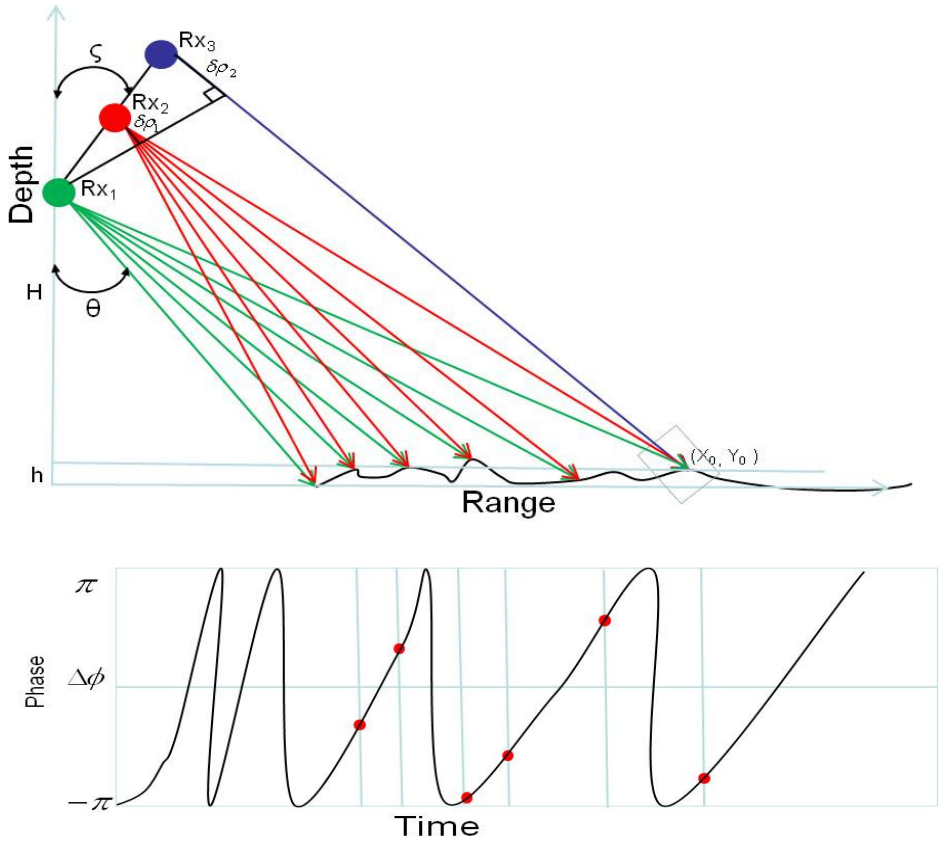

Figure 4.2 The measured wrapped phase showing 2π ambiguity in the cross range. The red dots in the phase verse time plot (bottom) are the phase differences for the corresponding time samples in the depth verse range plot (top).

An Interferogram is a map of the phase differences for a set of returns. Repeating fringes represent a jump in the 2π cycle ergo the phase is measured modulo 2π. Figure 4.3 is an interferogram of a seafloor image with two targets. The measured phase for a single scan line is overlaid on the interferogram illustrating the 2π jumps aligning with fringes of the interferogram.

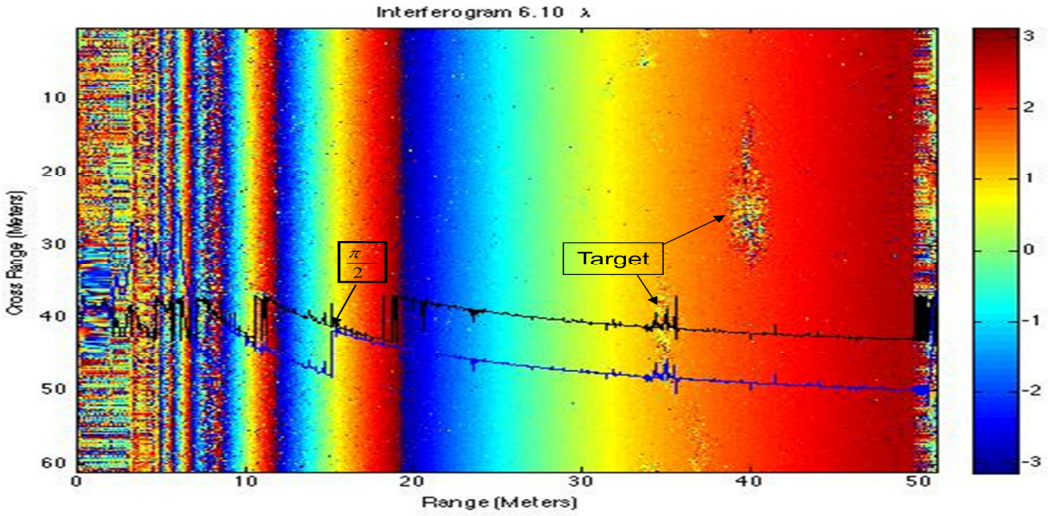

Figure 4.3 An Interferogram of an image scene of the ocean bottom with two targets overlaid with the measured wrapped phase (black) and the unwrapped phase (blue) from a single sounding.

The Phase is unwrapped by adding a 2π to the phase jumps and summing all the phases. This is known as the Itoh condition. The true phase per sounding *(k)* is

$$\Delta\Phi_{(k)} = \Delta\varphi_{(k)} + 2\pi m_{(k)} = \frac{2\pi b}{\lambda} \sin\left(\theta_s - \theta_{(k)}\right) \tag{4.12}$$

$\Delta\varphi$ is the measured wrapped phase, m is the phase jump counter, b is the baseline between arrays, λ is the wavelength, θ is the direction of arrival, and θ_s is the steering angle.

It is also important to consider the phase angle as a function of the arctangent because there are jumps at the boundaries where $\Delta\varphi = \pm \pi/2$, because $\cos(\pm \pi/2) = 0$, and the tangent is undefined. Adding $\pm \pi/2$ at the arctangent boundaries will correct for this phase jump. The phase as a function of the arctangent

$$\Delta\varphi = \tan^{-1}\left(\frac{\sin(\Delta\varphi)}{\cos(\Delta\varphi)}\right) \tag{4.13}$$

4.1.2 Bathymetric Height

The unwrapped phase is then used to obtain the direction of arrival $\theta_{(k)}$, often referred to as the bathymetric sounding.

$$\theta_{(k)} = \theta_s - sin^{-1}\left(\frac{\Delta\varphi_{(k)} + 2\pi m_{(k)}}{\frac{2\pi b}{\lambda}}\right) \tag{4.14}$$

The direction of arrival can also be expressed as a function of range

$$\theta_{(k)} = cos^{-1}\left(\frac{\rho_2^2 - b^2 - \rho_1^2}{2b\rho_1}\right) - \varsigma \tag{4.15}$$

Accuracy in the direction of arrival $\theta_{(k)}$ is crucial to trigonometrically solving for the change in bathymetric height h.

$$h = H - \rho_1 cos\theta_{(k)} \tag{4.16}$$

H is the altitude or height of the array above the seafloor, and ρ_1 is the range.

4.1.3 Zero Phase Instance (ZPI) difference max amplitude mean time

ZPI is one of the older methods used in bathymetric height determination. The backscattered signal reaches the array from an angle normal to the interferometer axis, both sensors receive the signal at the same time. Therefore, the difference between time of arrival and phase is zero. The phase ramp as a function of time is fitted with a polynomial whose intersection at zero-phase give the instant corresponding to the direction of arrival. This polynomial approximation acts as a low pass filter decreasing the noise level and degrading the horizontal resolution.

4.1.4 Co-registration

Precise and robust measurements of the phase are complicated due to environmental and system sources of noise. The difficulties come from extreme terrain, media variations, multipath reflections, height induced layover, shadows, low signal to noise ratios, aliasing, coherence loss, baseline decorrelation, footprint misalignment, temporal decorrelation and numerical processing noise [Lurton 2000] [Saebo 2005] [Barclay 2006].

Co-registration is a method to remove the effects of footprint misalignment. Co-registration is performed by maximizing the local coherence between the two images by shifting one of the images to align with the other image. This requires a cross correlation and finding the time lag between the two received signals and shifting one of the

images until they align. Co-registration needs to be performed at the subpixel level, upsampled by a factor of ten and interpolated between subswath centers to estimate the time delay for each range bin [Banks 2000]. The range difference as a function of range ρ_1 of the first image is

$$(\rho_2 - \rho_1) = \sqrt{(H + b\,cos\varsigma) + \left(\sqrt{(\rho_1^2 - H^2)} - b\,sin\varsigma\right)^2} - \rho_1 \tag{4.17}$$

H is the height of the sonar above the seafloor, b is the baseline, ρ_1 is the range to the first receiver, and ς is the tilt angle. Figure 4.4 illustrate how co-registration acts as a filter reducing the noise that causes phase ambiguities.

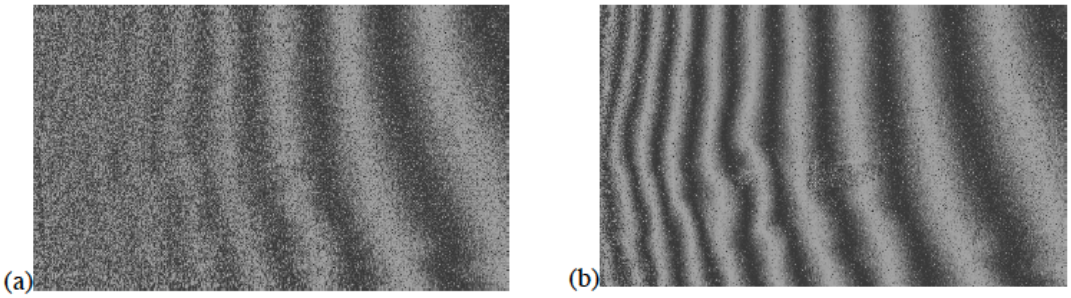

Figure 4.4 Co-registration: (a) interferogram before image co-registration, (b) after three iterations of coregistration.

It is important to know the degree of corelation between the two signals. This is known as the correlation coefficient or coherence and can be used to create a quality map of the data (quality maps are used in phase unwrapping).

$$\gamma = \frac{\langle P_1 P_2^H \rangle}{\sqrt{\langle P_1 P_1^H \rangle}\sqrt{\langle P_2 P_2^H \rangle}} = \mu e^{i\psi} \tag{4.18}$$

The Signal to Noise Ratio (SNR) as a function of the coherence factor is

$$SNR = \frac{\gamma}{(1-\gamma)} \tag{4.19}$$

The probability density function (PDF) for the error in the estimate of the phase is

$$P(\varphi) = \frac{1-\gamma^2}{2\pi}\frac{1}{1-\gamma^2 cos^2(\varphi - \varphi_T)}\left(1 + \frac{\gamma cos(\varphi - \varphi_T) cos^{-1}\left(-\gamma cos(\varphi - \varphi_T)\right)}{\sqrt{1-\gamma^2 cos^2(\varphi - \varphi_T)}}\right) \tag{4.20}$$

The standard deviation is

$$\sigma_{\varphi}^{2} = \int (\varphi - \varphi_T)^2 \; P(\varphi, \gamma) d\varphi \tag{4.21}$$

4.2 Phase Unwrapping Techniques

There are many techniques for two-dimensional phase unwrapping for InSAS systems with varying ranges of success [Ghiglia & Pritt 1998] [Sintes et al. 2000] [Chen 2001] [Saebo & Hansen 2004] [Jun et al. 2007]. Two commonly used methods are Path-Following developed by R.M. Goldstein and Minimum-Norm. Path-Following techniques presented in this dissertation are: Region-Growing, Mask-Cuts, and Minimum Discontinuity, followed by Minimum-Norm with least-squares.

4.2.1 Path Following Method (PFM)

Path-following with branch cuts is a local optimization theory. It is highly dependent on residues and quality maps. This method identifies the residues, then balances them by connecting them with branch-cuts in pairs of opposite polarity [Goldstein 1988] [Zebker & Lu 1998]. The branch-cuts are generated by a method that attempts to minimize the sum of the cut lengths to obtain a consistent phase. There is a decrease in performance as the residue density increases. Discontinuities and noise will lead to different paths and different phase values. It is difficult to find the correct path and this method is computationally expensive.

Goldstein's method starts with a normalized phase map. When the difference between adjacent pixels changes by .5 $\pm$1 is added to the next pixel. This is done for each pixel in the phase map. The $\pm$1 is referred to as a residue, $\pm$ pairs are linked using a cut line. An optimized solution is found by minimizing the branch cut lengths.

0.1 0.2 0.5 0.3
0 0 0
0.0 → 0.3 0.4 → 0.0
↑ *+1* ↓ *0* ↑ *-1* ↓
0.8 ← 0.6 0.4 ← 0.8
0 0 0
0.8 0.7 0.7 0.8

Figure 4.5 Normalized phase map showing the path following method with residues [Banks et al. 2000].

4.2.2 Region growing

Region growing is a quality guided path-following algorithm. In areas of high quality pixels the region of unwrapped pixels grows until only low quality pixels are left. The algorithm follows the path of highest quality

pixels through the low quality regions until the net high quality region is encountered, thus unwrapping the highest quality pixels first. This method allows for phase changes between two adjacent pixels larger than π. This method depends on a good quality map. The quality map will guide the integration path without encircling any unbalanced residues [Xu & Cummings 1999].

Quality Maps provide quality information on the interferometric phase by measuring the absolute value of the coherence correlation coefficient. Coherence is low for pixels having high decorrelation or original phase discontinuities.

$$\alpha = |\rho| = \left| \frac{\sum u_{ij} v_{ij}^{*}}{\sqrt{\sum |u_{ij}|^2 \sum |v_{ij}|^2}} \right| \tag{4.22}$$

4.2.3 Mask-cut algorithm

Mask-cut algorithms grow pixel masks that connect the residues often referred to as mask-cuts. It uses the quality map to guide the placements of the mask cuts. This method is more stable then the region growing method.

4.2.4 Minimum discontinuity

Minimum discontinuity approach identifies the lines of discontinuities that are joined into loops and then adds the appropriate multiples of 2π to the pixels enclosed by the loop. This is a recursive method reducing the number of discontinuities at each stage.

4.2.5 Minimum Norm Methods Global Optimization Theory

Minimum Norm Methods (MNM) attempt to find an absolute phase image solution Φ for which L^p norm of the difference between absolute phase derivatives and wrapped phase derivatives are minimized.

4.2.6 Least-Squares Method

Least-Squares Method (LSM) unwrapping is achieved by minimizing the mean square deviation between the estimated and unknown neighboring pixel differences of the unwrapped phase. It is computationally faster than the aforementioned path-following methods. However, the resulting unwrapping is not very accurate, because least-squares procedures tend to spread the errors that are concentrated on a limited set of points [Abbas 05]. Unweighted least square method gives poor results in areas of low to medium coherence.

Method of Least-Squares

$$\langle E \rangle = \min \sum_{i=1}^{M-1} \sum_{j=1}^{N} \omega_{i,j}^{x} \left[\left(\phi_{i+1,j} - \phi_{i,j} \right) - W\left(\psi_{i+1,j} - \psi_{i,j} \right) \right]^{P} + \sum_{i=1}^{M-1} \sum_{j=1}^{N} \omega_{i,j}^{y} \left[\left(\phi_{i,j+1} - \phi_{i,j} \right) - W\left(\psi_{i,j+1} - \psi_{i,j} \right) \right]^{P} \quad (4.23)$$

$\psi_{i,j}$ is the wrapped phase, $\phi_{i,j}$ is the unwrapped phase, ω is the frequency, and W is the weight (filter).

[Ghiglia & Pritt 1998] offer several methods for weighted least squares. They are the Picard iteration method, Preconditioned Conjugate Gradient method, and the Multigrid method. A combined branch-cuts and branch-cut with least squares, where pole locations form the weighting basis for the weighted least-square approach is an improvement over weighted least squares based on coherent data weighting schemes [Akerson et al. 2000]. Weighted methods are limited in that they can only compensate for isolated low coherence areas caused by effects such as shadowing and layover. Instead of unwrapping the phase by adding 2π at the artificial phase jumps in phase characteristics, Abbas suggests a recurrent formula to calculate the unwrapped phase at the boundaries of the arctangent function. LS Delta K method of phase unwrapping for SAR splits the image into subbands and determines the phase frequency [BRCIC 2009].

4.2.7 Kalman filter

Kalman filter Phase unwrapping algorithm based on an Extended Kalman filter [Martinez-Espla 2009] exploits a so called “Basic - Slope Model" enabling the filter to incorporate additional local slope information obtained from the sample frequency spectrum of the interferogram by a local slope estimator. The local slope information is then optimally fused with the information directly obtained from the real and imaginary part of the interferogram [Loffeld & Kramer 1994] [Kramer & Loffeld 1996] [Osmanoglu 2009].

4.3 Robust Phase Unwrapping Techniques

The aforementioned phase unwrapping methods originally developed for InSAR systems have proven to be unstable for InSAS systems [Zebker & Lu 1998] [Jun 2007] [Kaplan 2007]. The difficulty in unwrapping the phase led to the development of more robust methods such as, the Vernier Method, and Cross-Correlation-Time-Delay-Estimation. They still require phase unwrapping but provide a better estimate of the phase.

4.3.1 Vernier Method (VM) The vernier method requires three arrays with two distinct baselines. The additional receiver is spaced less than one wavelength from the top and or bottom array. The phase difference will only contain one wrap therefore, the phase will not have the modulo 2π ambiguity. The phase difference between the shorter baseline is used to unwrap the phase of the larger baseline that has higher resolution [Denbeigh 1989] [Sintes 2002] [Llort-Pujol et al. 2008] [Sintes et al. 2010] [Sintes et al. 2011]. This method can also be conducted using

multiple frequencies. Lower frequency data is used to unwrap the phase of the higher frequency data that has better resolution [Wei Xu et al. 1994] [Hayes 2001] [Hayes 2005] [Gough et al. 2006] [Sintes et al. 2008]. The vernier method relies on estimating the direction of arrival by finding the rotation counter couple (m_1, m_2) that minimizes the difference between range verse direction of arrival curves. Dual baseline method is

$$\frac{\Delta\varphi_{(1)}\lambda}{2\pi b_1} + \frac{m_{(1)}\,\lambda}{b_1} = cos\left(\theta_{(k)} + \varsigma\right) = \frac{\Delta\varphi_{(k)}\lambda}{2\pi b_2} + \frac{m_{(2)}\,\lambda}{b_2} \tag{4.24}$$

Dual frequency method is

$$\frac{\Delta\varphi_{(1)}\lambda_{(1)}}{2\pi b} + \frac{m_{(1)}\,\lambda_{(1)}}{b} = cos\left(\theta_{(k)} + \varsigma\right) = \frac{\Delta\varphi_{(k)}\lambda_{(2)}}{2\pi b} + \frac{m_{(2)}\,\lambda_{(2)}}{b} \tag{4.25}$$

The baseline or frequencies have to be selected so that the overlapping curves are within $\{-\pi/2, \pi/2\}$. In practice this is difficult and often the curves do not overlap. A minimization technique is then required to solve for the rotation counter. This technique may still leave some phase ambiguities.

$$(m1, m2) = min\left\{\left(\frac{\Delta\varphi_{(1)}\lambda}{2\pi b_1} + \frac{m_{(1)}\,\lambda}{b_1}\right) - \left(\frac{\Delta\varphi_{(k)}\lambda}{2\pi b_2} + \frac{m_{(2)}\,\lambda}{b_2}\right)\right\} \tag{4.26}$$

The vernier efficiency defines the robustness of the algorithm to remove the phase ambiguity in the presence of noise by drawing a map for different values of baselines. The efficiency is inversely proportional to the baselines length [Sintes et al. 2000] [Llort-Pujol et al. 2008].

$$eff_{(1,2)} \triangleq \frac{1}{2} min\left\{\frac{m_{(1)}\,\lambda}{b_1} - \frac{m_{(2)}\,\lambda}{b_2}\right\} \tag{4.27}$$

4.3.2 Cross Correlation Time Delay Estimation (CC-TDE) complex cross-correlation of across-track image stripes are used to estimate the coarse lag with pixel-size resolution which can be used to find the phase within the correct 2π interval. This method combined with the full resolution phase difference derived from the interferometry provides robust height estimation [Banks et al. 2000] [Banks et al. 2001] [Hansen 2003] [Saebo et al. 2004] [Saebo et al. 2005] [Saebo et al. 2006] [Saebo et al. 2007] [Llort-Pujol et al. 2008] [Saebo et al. 2009] [Saebo 2010] [Vossen 2008]. By formulating a generalized steering vector first then, taking advantage of the coherence information of neighboring pixel pairs, the covariance matrix of a complex data vector is estimated. Then used to formulate a global optimum cost function of the covariance matrix, by which the exact interferometric phase can be estimated when the cost function is minimized [Zhang 2008] [Liu et al. 2009]. The two signals are cross correlated

over a temporal window to obtain the correlation peak μ and the coarse time lag τ_c at the peak of the correlation envelope and the corresponding phase Φ. The estimate of the interferometric delay τ_f where the ambiguity number m (phase jump counter) is found from the condition that $| \tau_c - \tau_f |$ is minimized. This method is similar to the Displaced Phase Center Antenna principle presented in chapter 2 [Hayes et al. 2008] [Pinto et al. 2001, 2000] [Lurton] [Saebo et al. 2006].

Apply an averaging window to each of the time series of the receiver pair with a window that covers a range between (1 meter to 1.5 meters). This range produces a low-variance estimate of the delay while short enough to assume a constant delay. The coarse delay is the location of the peak magnitude which is the number of whole wavelengths spanned by the time shift.

$$\Delta\tau_{coarse} = max|P_1 P_2^H| \tag{4.28}$$

The fine delay is the fractional part of a wavelength.

$$\Delta\tau_{fine} = \frac{\Phi}{2\pi f_0} + \frac{m}{f_0} \tag{4.29}$$

Φ is the phase, f_o is the frequency, and m is the ambiguity number satisfying the condition that minimizes $\Delta\tau$.

$$\Delta\tau = \Delta\tau_{coarse} - \Delta\tau_{fine} \tag{4.30}$$

The range is

$$c\Delta\tau = \rho_2 - \rho_1 = \sqrt{(x - x_2) + (z - z_2)} - \sqrt{(x - x_1) + (z - z_1)} \tag{4.31}$$

(x,z) is the location of the seafloor, (x_1,z_1) is the location of Rx_1 and (x_2,z_2) is the location of Rx_2. The direction of arrival is

$$\theta_0 = \frac{c\Delta\tau}{b} \tag{4.32}$$

Which equates to the depth z

$$z = \frac{z_1 + z_2}{2} + R_{rpc} sin(\theta_0 + \phi_{roll}) \tag{4.33}$$

R_{rpc} is the range of the phase center, θ_0 is the direction of arrival at zero phase, b is the baseline, ϕ is the angle of the roll. Step two is to produce the correlation coefficient between the two signals. Assume P_{1ij} and P_{2ij} are zero-mean, wide-sense stationary and ergodic. The cross covariance is

$$\gamma = \frac{\langle P_1 P_2^H \rangle}{\sqrt{\langle P_1 P_1^H \rangle}\sqrt{\langle P_2 P_2^H \rangle}} = \mu e^{i\psi} \tag{4.34}$$

$$P_{1_{ij}} = p_m(t)\left(t - \frac{2\rho_1}{c}\right) e^{i\omega_0 t} \tag{4.35}$$

$$P_{1_{ij}} = p_b(t)\left(t - \frac{2\rho_1}{c}\right) e^{i\omega_0\left(t - \frac{2\rho_1}{c}\right)} e^{-i\omega_0 t} \tag{4.36}$$

$$P_{1_{ij}} = p_b(t)\left(t - \frac{2\rho_1}{c}\right) e^{i\omega_0\left(\frac{2\rho_1}{c}\right)} \tag{4.37}$$

$$P_{2_{ij}} = p_b(t)\left(t - \frac{2\rho_2}{c}\right) e^{i\omega_0\left(\frac{2\rho_2}{c}\right)} \tag{4.38}$$

$$C_{mn} = \int P_{1_{ij}}(\lambda) P_{2}^{H}{}_{ij}(\lambda - t) d\lambda \tag{4.39}$$

$$\gamma_{mn} = \int p_b(t)\left(\lambda - \frac{2\rho_1}{c}\right) p_b(t)^H \left(\lambda - t - \frac{2\rho_2}{c}\right) e^{-i\omega_0\left(\frac{2(\rho_2 - \rho_1)}{c}\right)} d\lambda \tag{4.40}$$

$$\gamma_{mn} = e^{-i\omega_0\left(\frac{2(R_2 - R_1)}{c}\right)} \int \left| p_b(t)\left(\lambda - \frac{2R_1}{c}\right)\right|^2 d\lambda \tag{4.41}$$

Step three due an FFT based cross correlation with interpolation for peak finding. Step four find the coarse delay based on the lag of correlation coefficient γ_{mn} [Pinto 2000]. Figure 4.6 shows the time delay estimate and the corresponding phase.

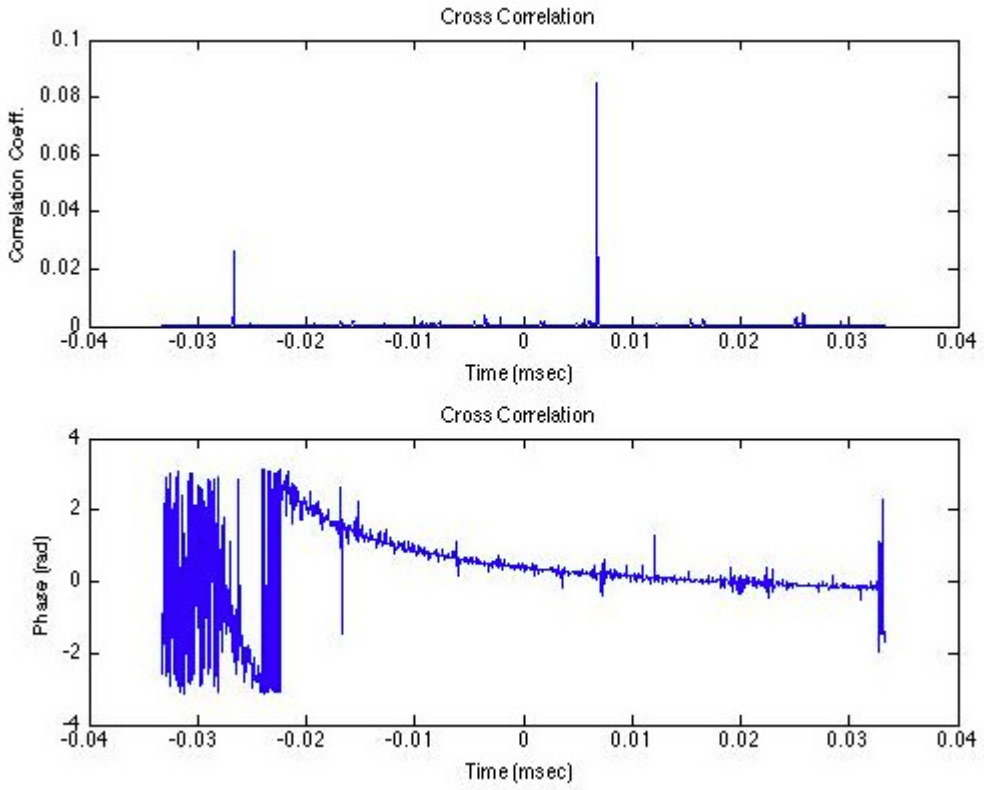

Figure 4.6 Cross Correlation Time Delay Estimate, and Phase delay estimate for cross correlation Phase

4.3.3 Phase Unwrapping–Free DEM Reconstruction – First step is breaking down the image into blocks selecting control points at the center and estimating the height. Create a coarse Digital Elevation Map (DEM) from those points by Least-Mean-Squares or interpolation. Resample the control blocks on to a reference plane. Interferometric phase variation is

$$\Delta\varphi = \frac{-4\pi}{\lambda}\frac{b\Delta h}{R\,sin\theta} - \frac{4\pi}{\lambda}\frac{b\Delta r}{R\,tan\theta} \tag{4.42}$$

b is the baseline, λ is the wavelength, Δh is the change height, R is the range, θ is the direction of arrival, and Δr is the change in range. This is known as interferogram flattening generating a phase map that is proportional to the terrain map which is added back in after DEM conversion. The maximum measured coherence is the real plane [Bai et al. 2010]. Similar to fast-factored-back-projection.

4.4 Bayesian and Regulation Methods

The limitations of the algorithms required a more precise phase measurement technique. Adaptive and maximum likelihood methods [Dias & Leitao 2002] offer a better alternative to phase unwrapping in this environment. Phase unwrapping as a constrained optimization problem using a maximum *a posteriori* probability (MAP) estimation is a viable approach for bathymetric height estimation [Barclay et al. 2003] [Chen 2001]. Chen takes it a step further

and derives a joint statistics of interferometric data and incorporates the statistics into a non-linear cost function. Below is a brief explanation of phase unwrapping methods.

4.4.1 Belief Propogation (BP) is a statistical filtering approach used to search a volume of height likelihoods. This volume is generated by remapping the slant range imagery onto a set of height differing ground planes, calculate the variance, convert the variance to likelihood find a maximum a posterior (MAP) estimation by either using a Bayesian or Hidden-Markov-Random-Field approach to make an estimate of the height using belief propagation as a statistical filter to find the most likely surface, given a volume of measured likelihood estimates and the expected variation between neighboring points [Barclay 2003] [Barclay 2006]. An alternative method is to back-project the echo data into the volume to be reconstructed [Hayes 2008]. A volumetric factor graph model which represents the joint probability distribution of the scene along with the Greedy algorithm is used to reconstruction a three-dimensional image of the scene [Forne 2007]. Maximum Likelihood (ML) phase difference is used to give the best estimate of the phase instead of phase unwrapping. Using the Max-product algorithm the belief B at node i for the h^{th} height is.

$$B_i^n(h) = L_i(h) \prod M_{ij}^n(h) \tag{4.43}$$

$$M_{ij}^n(h) = max(h')\left(\Psi(h,h')\frac{B_i^n(h')}{M_{ij}^{n-1}(h')}\right) \tag{4.44}$$

$$M_{ij}^n(h) = \left(\frac{M_{ij}^{n-1}(h) + M_{ij}^n(h)}{\sum_{h=1}^{H} M_{ij}^{n-1}(h) + M_{ij}^n(h)}\right) \tag{4.45}$$

$$M_{ij}^0(h) = H^{-1} \tag{4.46}$$

$$\widehat{h_\iota} = \max B_i(h) \tag{4.47}$$

4.4.2 ZπM Method (ZπM) An effective algorithm for absolute phase estimation from incomplete, noisy and modulo-2 observations in interferometric aperture radar and sonar (InSAR/InSAS). Bayesian viewpoint is adopted; the observation density is 2π periodic and accounts for the interferometric pair decorrelation and system noise; the *a priori* probability of the absolute phase is modeled by a compound Gauss–Markov random field (CGMRF) tailored to piecewise smooth absolute phase images. An iterative scheme for the computation of the maximum *a posteriori* probability (MAP) absolute phase estimate, where each iteration embodies a discrete optimization step (Z -step), implemented by network programming techniques, and an iterative conditional modes (ICM) step (π-step).

Accordingly, the algorithm is termed ZπM , where the letter M stands for maximization. An important contribution of ZπM is the simultaneous implementation of phase unwrapping, and smoothing. This improves considerably the accuracy of the absolute phase estimates compared to methods in which the data is low-pass filtered prior to unwrapping [Dias 2002].

4.4.3 Multiple frequency interferometry is, basically, a phase acquisition strategy aimed at reducing or eliminating the ambiguity of the wrapped phase observations or, equivalently, reducing or eliminating the fringe ambiguity order. In multiple frequency interferometry, the phase measurements are acquired at different frequencies (or wavelengths) and recorded using the corresponding sensors (measurement channels). Assuming that the absolute phase to be reconstructed is piece-wise smooth, we use a nonparametric regression technique for the phase reconstruction. The nonparametric estimates are derived from a local least squares criterion, which, when applied to the multi-frequency data, yields denoised (filtered) phase estimates with extended ambiguity (periodized), compared with the phase ambiguities inherent to each measurement frequency. The filtering algorithm is based on local polynomial (LPA) approximation for design of nonlinear filters (estimators) and adaptation of these filters to unknown smoothness of the spatially varying absolute phase. For phase unwrapping, from filtered periodized data, we apply the recently introduced robust (in the sense of discontinuity preserving) PUMA unwrapping algorithm. Simulations give evidence that the proposed algorithm yields state-of-the-art performance for continuous as well as for discontinues phase surfaces, enabling phase unwrapping in extraordinary difficult situations when all other algorithms fail. [Matias 2006] [Dias 2007] [Katkovnik 2010]

4.4.4 PUMF Phase Unwrapping Max Flow (PUMF) algorithm was developed by SAR data. PUMF is an energy minimization approach using binary moves optimization scheme adopted from the ZπM algorithm similar to the classic L^p Norm mapped on to a max-flow problem. PUMF was benchmarked against the previous mentioned PU algorithms with very positive results [Matias 2006].

4.4.5 Markov Random Field phase unwrapping method using a region-based Markov Random Field (MRF) model. Specifically, the phase image is segmented into regions within which the phase is not wrapped. Then, the phase image is unwrapped between different regions using an improved Highest Confidence First (HCF) algorithm to optimize the MRF model. The proposed method has desirable theoretical properties as well as an efficient implementation. Simulations and experimental results on MRI images show that the proposed method provides similar or improved phase unwrapping than Phase Unwrapping Max-flow/min-cut (PUMA) method and *ZπM* method [Dong & Ji 2010].

Summary

There exists a plethora of phase unwrapping algorithms, too many to mention. Robustness and accuracy are the desired attributes. Computational time and memory consumption are the limiting factors in choosing a technique for a real time system. The cross-correlation and vernier method are equally suited for phase unwrapping. The

Bayesian Regulation methods are well suited for InSAS systems operating in noisy shallow water enviornments. Belief Propagation and ZπM have the potential of becoming the algorithm of choice.

Chapter 5 Data Analysis

The purpose of this research was to develop a robust signal processing technique for an InSAS system. The challenges were to choose a beamforming technique that would preserve the phase and be suitable to produce a SAS image; secondly, to find a phase unwrapping technique robust enough to unwrap the phase in a noisy environment; and finally, to produce a three dimensional bathymetric image suitable for automatic target recognition. In the beginning of chapter two I presented the flowchart shown again in Figure 5.1 for bathymetric reconstruction. The highlighted fields represent the work performed for this dissertation research.

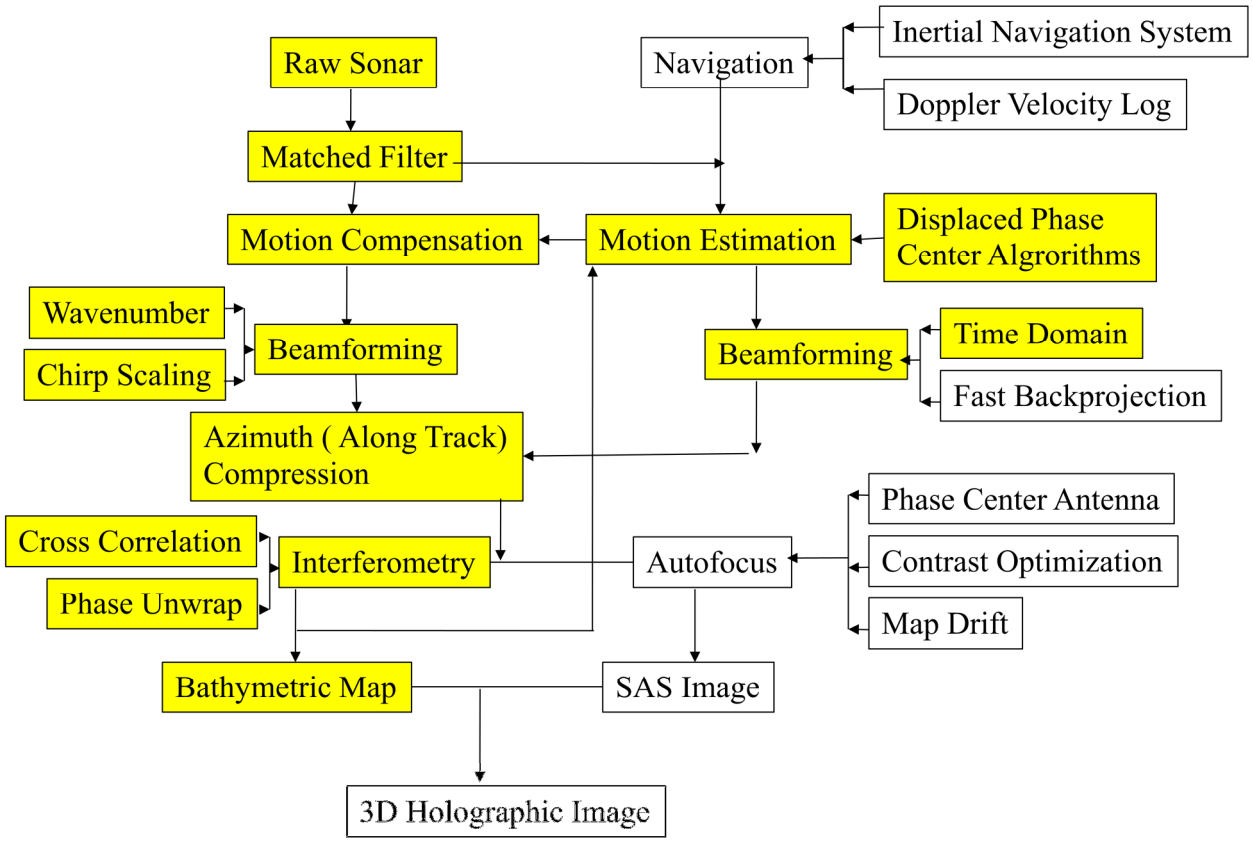

Figure 5.1 Flowchart for Bathymetric Reconstruction.

In the process I have been working on the development of the InSAS toolbox that is a platform for testing InSAS algorithms, processing InSAS data, and producing three dimensional bathymetric maps.

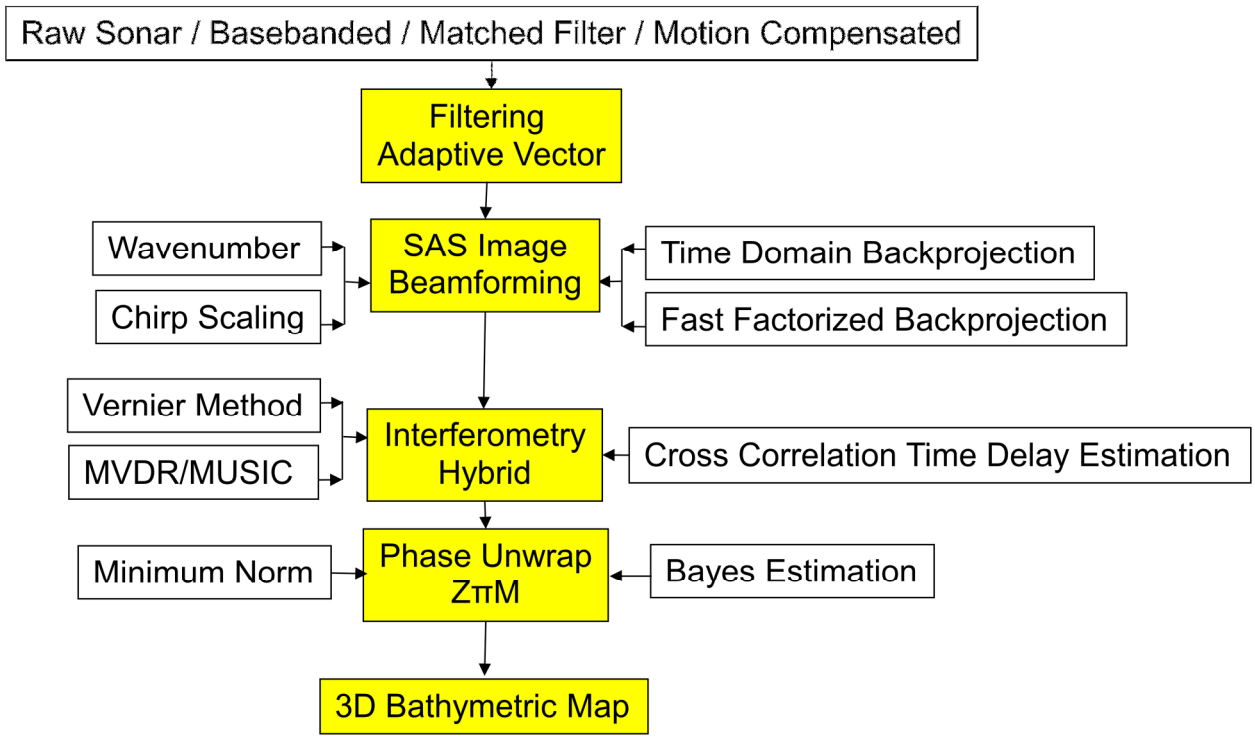

Figure 5.2 InSAS Toolbox

For this research I worked with simulated raw stave data produced by the Personal Computing Shallow Water Acoustic Toolbox Version 10 (PC SWAT). PC SWAT uses the Gaussian RAy Bundle (GRAB) model for the propagation and high frequency environmental models. It uses a three dimensional height map to describe the sea bottom terrain. For this simulation the AUV was flying at five meters above the seafloor at a depth of ten meters from the surface. The array was on a tilt angle of ten degrees. The incident signal is a linear frequency modulated chirp centered at 175 kHz with a bandwidth of 30 kHz, a pulse period of 1.0 millisecond, a pulse repetition rate of 66.67 milliseconds, a beamwidth of 30°, and a sound pressure level of 220 dB re 1 μ Pascal.

The raw stave data prior to signal processing is for 1600 pings in the along-track direction and 3984 time samples in the across-track direction. The scene to be imaged contains three geometric shapes: at a range of twenty meters there is a cube with dimensions of one meter, at a range of thirty meters a cylinder that is half a meter in diameter with a length of one meter pointed on a forty-five degree angle towards the array, and at a range of forty meters there is a one meter diameter sphere. Range migration causes the reflection from the sphere to spread in the along-track direction. The raw sonar data has high intensity in the near range and fades in the far range. This is due to the loss in intensity from spherical spreading, and is compensated for with use of a time varying gain routine. The raw stave data is presented in Figure 5.3.

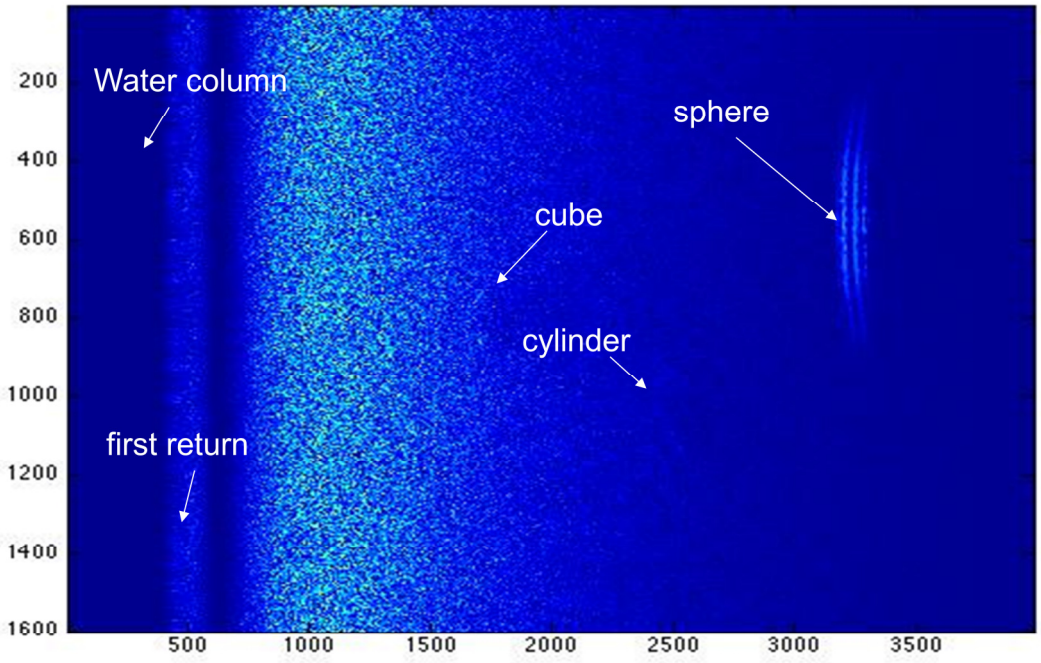

Figure 5.3 Raw sonar data with cube, cylinder and sphere.

In this research I investigated two beamformers: wavenumber and chirp scaling. Early on in my research the chirp-scaling seemed to produce the best image, but after adjusting some of the parameters I found the wavenumber to produce an image just as good as chirp-scaling. The synthetic aperture sonar image in Figure 5.4 was produced using the wavenumber beamformer. The synthetic aperture sonar image in Figure 5.5 was produced with the chirp-scaling beamformer. There is a little smearing in the cross range in the chirp-scaling that can easily be corrected with an adjustment to beamforming parameters.

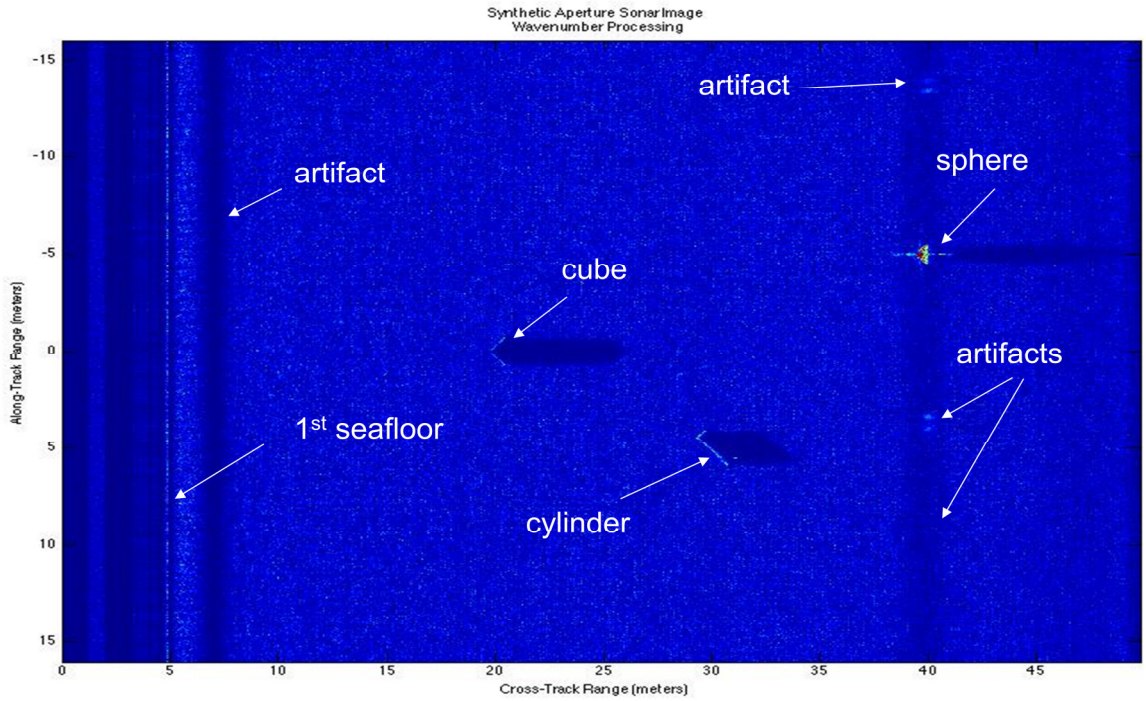

Figure 5.4 Synthetic Aperture Sonar image with three geometric objects (cube, cylinder and sphere) produced with wavenumber processing.

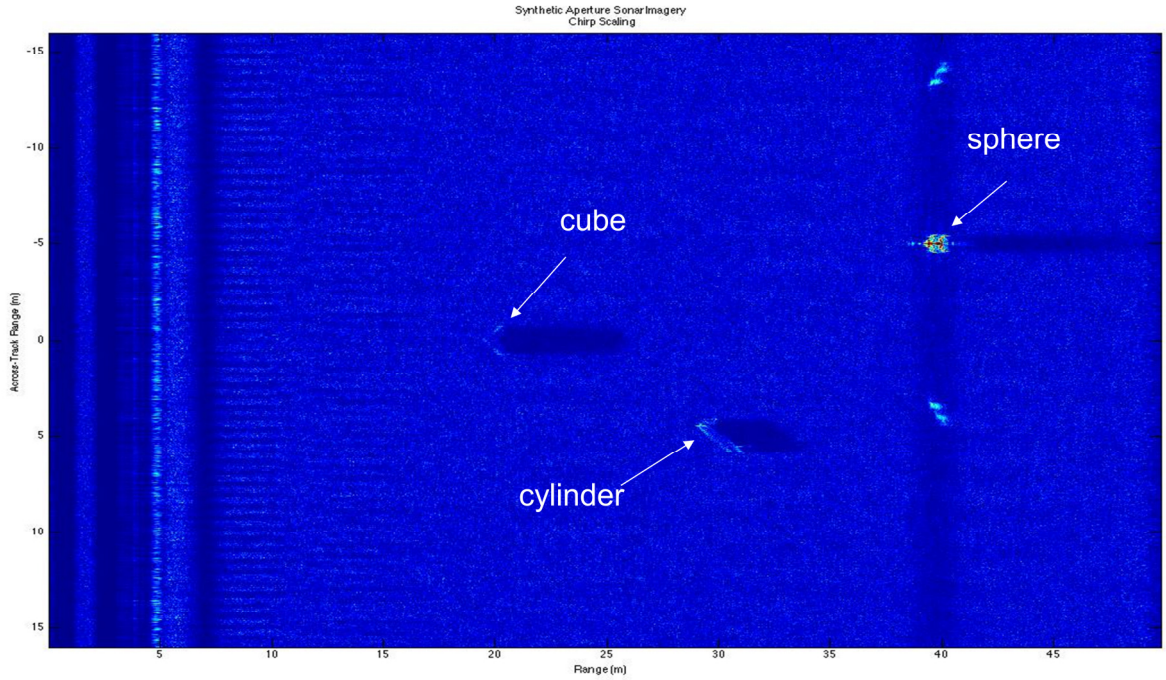

Figure 5.5 Synthetic Aperture Sonar image with three geometric objects (cube, cylinder and sphere) produced with chirp-scale processing.

There are two artifacts that run parallel to the along-track direction. The first is caused by the beamforming and the second is caused by the time varying gain. At forty meters there are two artifacts produced by the sphere where the energy was picked up in the sidelobes. For the rest of the research I choose to use the chirp-scaling beamformed image because it is computationally faster, requires less memory, and is phase preserving.

I modeled the true phase based on the geometry of the system for four of the baselines. The modeled phases run parallel to each other, and the offset is a function of wavelength and baseline. The modeled phase is needed to measure the performance of the phase unwrapping algorithm.

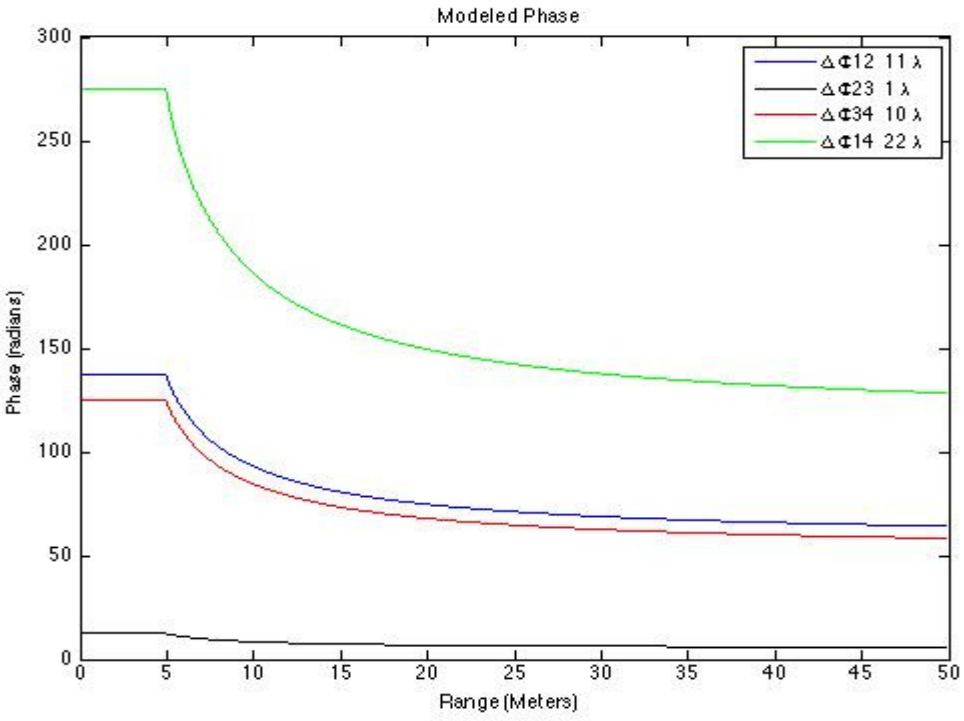

Figure 5.6 Modeled phase for four array pairs with baselines of 11λ (blue), 1λ (black), 10λ (red), and 22λ (green).

I created an interferogram from the measured phase differences for the 11λ baseline from the image in Figure 5.5. The colored fringes represent the phase jumps from π to -π. I overlaid the measured phase difference for a single ping that ensonified the cube. From the measured wrapped phase I generated the unwrapped phase using the Itoh method. I then shifted and plotted the unwrapped phase to align with the wrapped phase. This shows how the phase jumps align with the fringes and how the height of the object affects the phase. The phase unwrapping technique missed a π/2 phase jump caused by an arctangent boundary. The artifacts that are parallel to the track at a range of 27 and 37 meters are also caused by the arctangent boundary. Both incidences corrupt the unwrapped phase, but are easily removed in the other phase unwrapping routines [Abbas 2005].

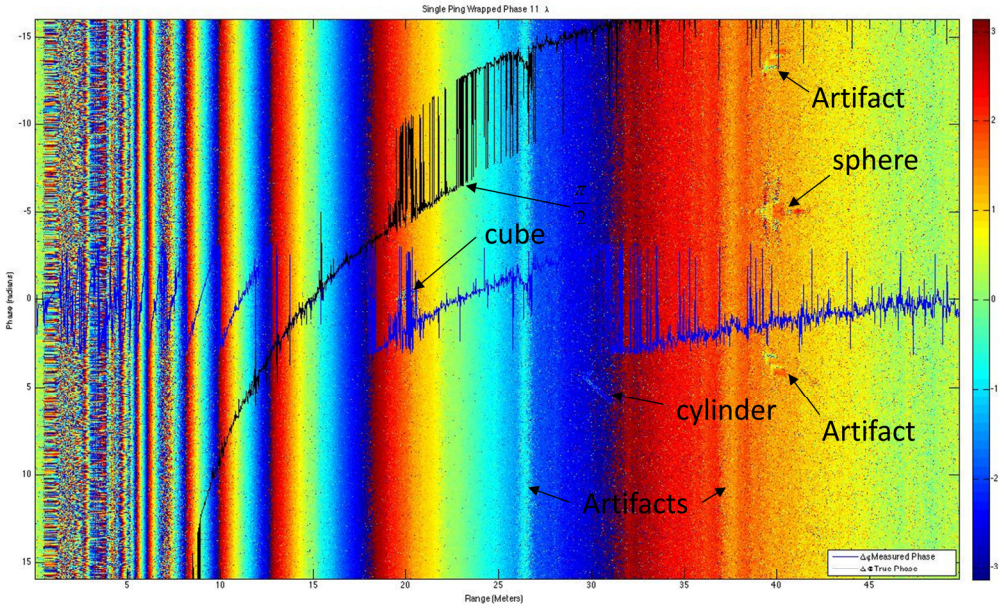

Figure 5.7 Interferogram with an 11λ baseline for the seafloor image, overlaid with the measured phase in blue and the true phase in black.

The 1λ baseline has only one phase jump at a range of eight meters and is easily unwrapped, however the resolution is insufficient for bathymetric height determination.

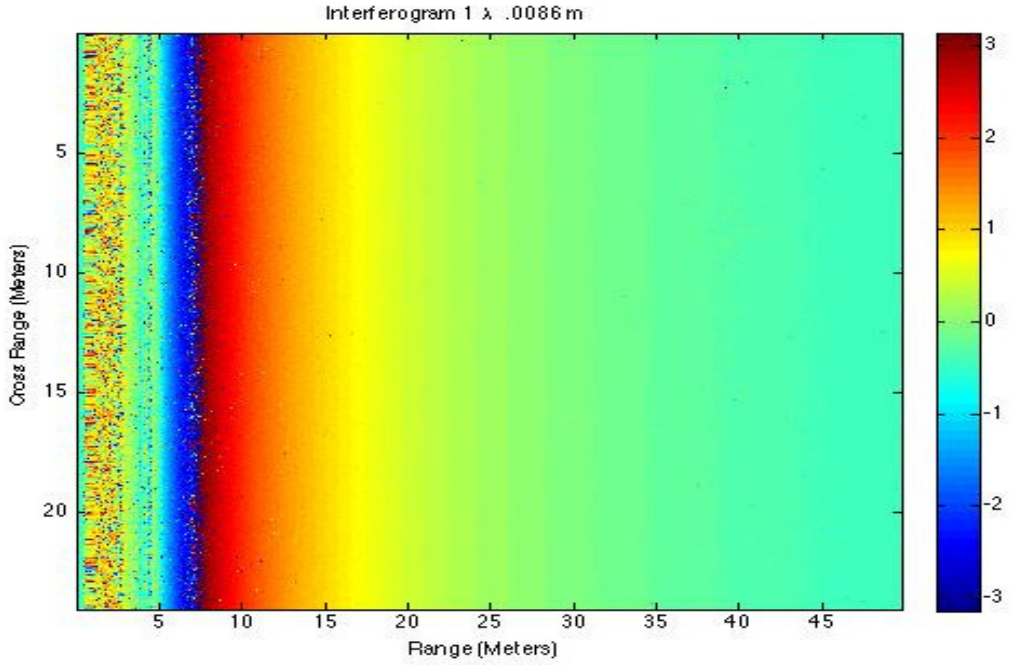

Figure 5.8 Interferogram for the 1λ baseline.

In Figure 5.9 the wrapped phase is unwrapped and fitted to the modeled phase using Eq. (5.1)

$$\Phi = model(\Phi) - angle\left(\frac{e^{imodel(\Phi)}}{e^{i\Delta\varphi}}\right) \tag{5.1}$$

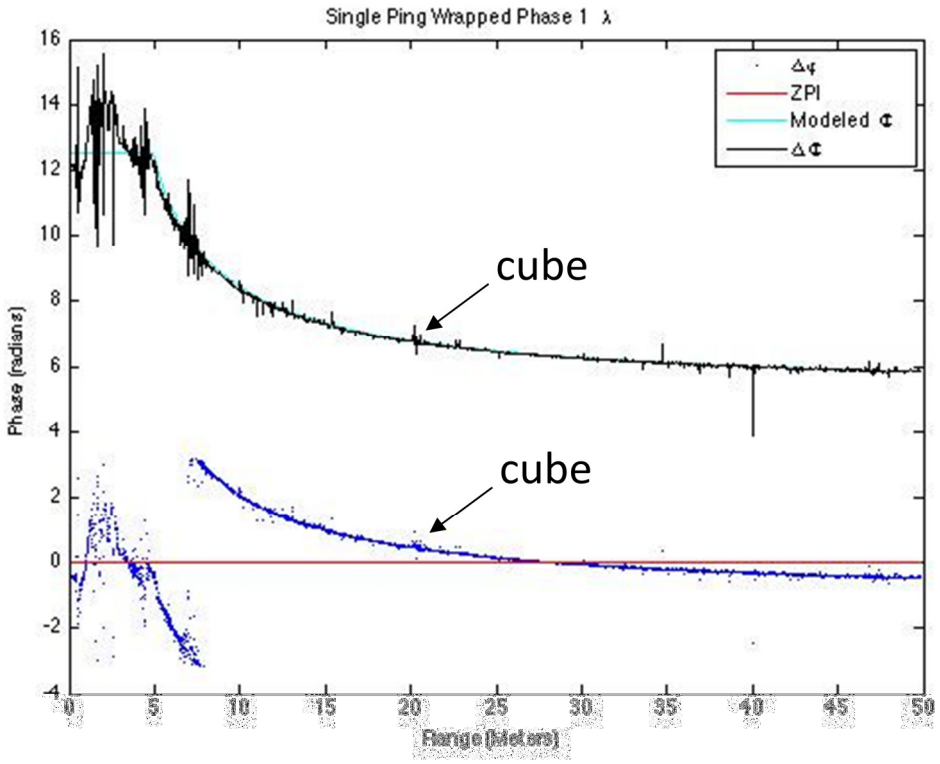

Figure 5.9 Unwrapped phase is fitted to the modeled phase for a 1 λ baseline, with the wrapped phase (blue), unwrapped phase (black), and modeled phase (cyan).

The bathymetry produced from the interferogram for the 1 λ baseline in Figure 5.10 gives an average height of half a meter, for the one meter cube, as indicated by the colorbar to the right with height in meters. This is insufficient accuracy for this application.

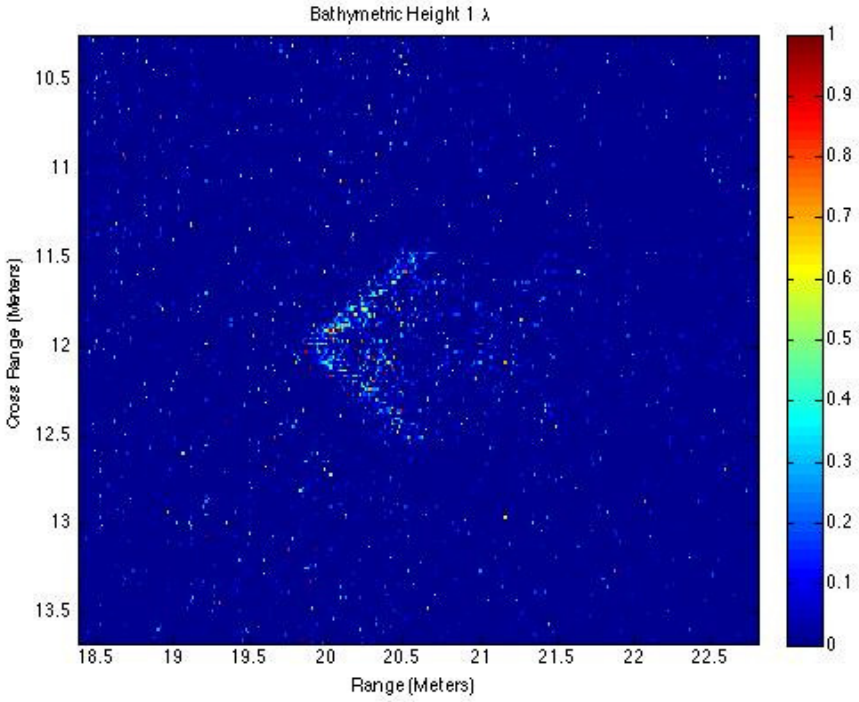

Figure 5.10 Bathymetry for cube 1λ baseline.

The phase information for the 11λ baseline for a single ping is shown in Figure 5.11. The measured wrapped phase is shown in blue, and, is unwrapped using the Itoh method. The true phase in black is then fitted to the modeled phase in cyan.

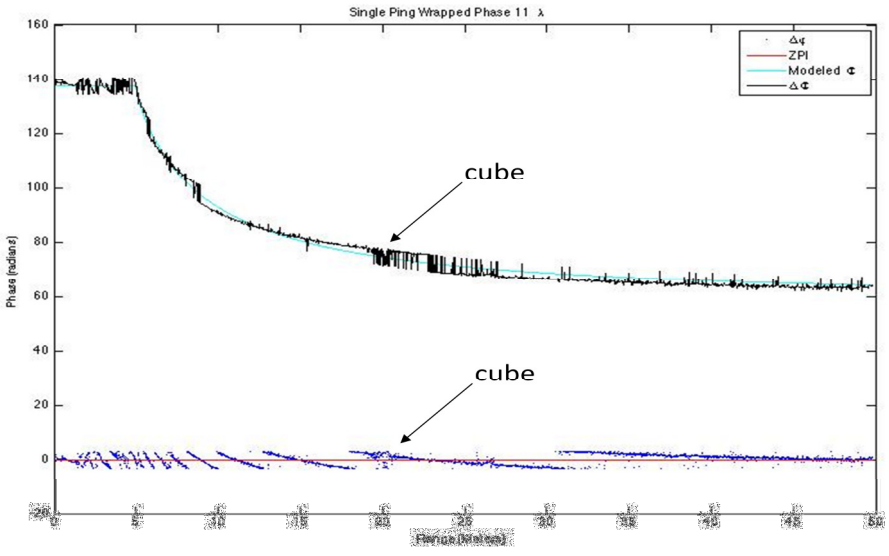

Figure 5.11 Unwrapped phase fitted to modeled phase for a single sounding with the zero phase instant in red, the measured wrapped phase in blue, the modeled phase in cyan and the fitted unwrapped phase in black.

This method has several ambiguous phase jumps and is not robust enough to obtain a direction of arrival suitable for bathymetric height determination. From the unwrapped phase I produced the direction of arrival and calculated the bathymetric height. The bathymetric image of scene is presented in Figure 5.12. Using this method I have therefore obtained an average height of 0.75 meters, which is fairly close to the actual height of one meter, but still insufficiently accurate for this application.

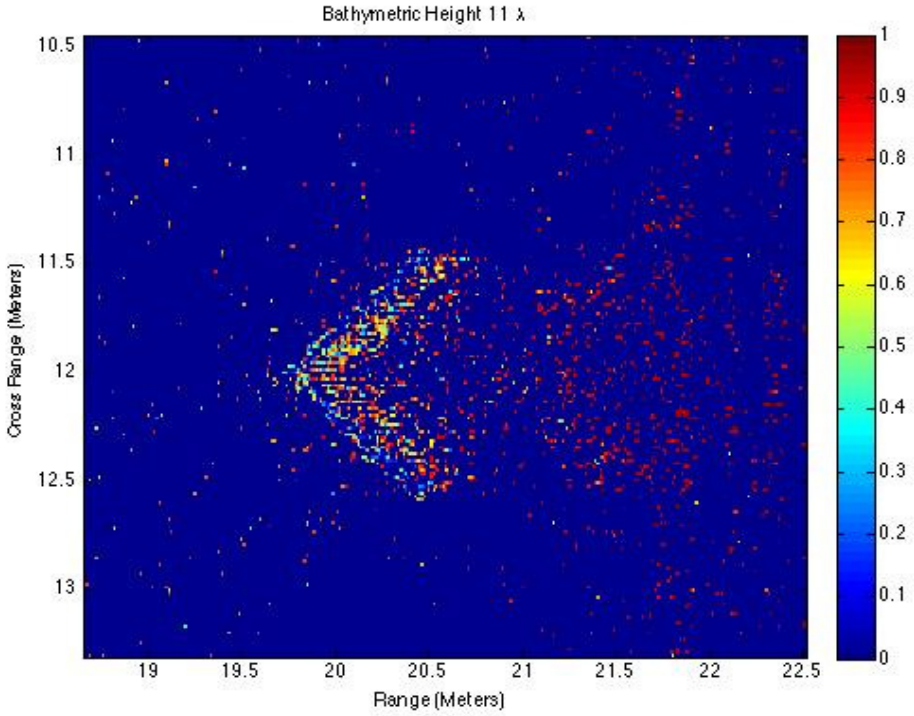

Figure 5.12 Bathymetric height of the cube.

Vernier Method

The Vernier principle is based on the information redundancies between baselines to estimate the exact phase in the interferometric equation expressed as the direction of arrival (see chapter four for details) [Sintes 2011].

$$\frac{\Delta\varphi_{(1)}\lambda}{2\pi b_1} + \frac{m_{(1)}\,\lambda}{b_1} = cos\left(\theta_{(k)} + \psi\right) = \frac{\Delta\varphi_{(k)}\lambda}{2\pi b_2} + \frac{m_{(2)}\,\lambda}{b_2} \qquad (5.2)$$

The vernier method works by finding the rotation counter pairs $(m_1,m_2) \in \{1,2,3,4\}^2$ that minimizes the phase difference.

$$(m1, m2) = min\left\{\left(\frac{\Delta\varphi_{(1)}\lambda}{2\pi b_1} + \frac{m_{(1)}\lambda}{b_1}\right) - \left(\frac{\Delta\varphi_{(k)}\lambda}{2\pi b_2} + \frac{m_{(2)}\lambda}{b_2}\right)\right\} \quad (5.3)$$

The direction of arrival curves *Cos(θ+ψ)* for the 1λ baseline and the 11λ baseline derived from Eq. (5.2) are shown in Figure 5.13. The curves that overlap provide the true phase. The direction of arrival derived from the MUSIC algorithm in blue is used to select the direction of arrival for the true phase.

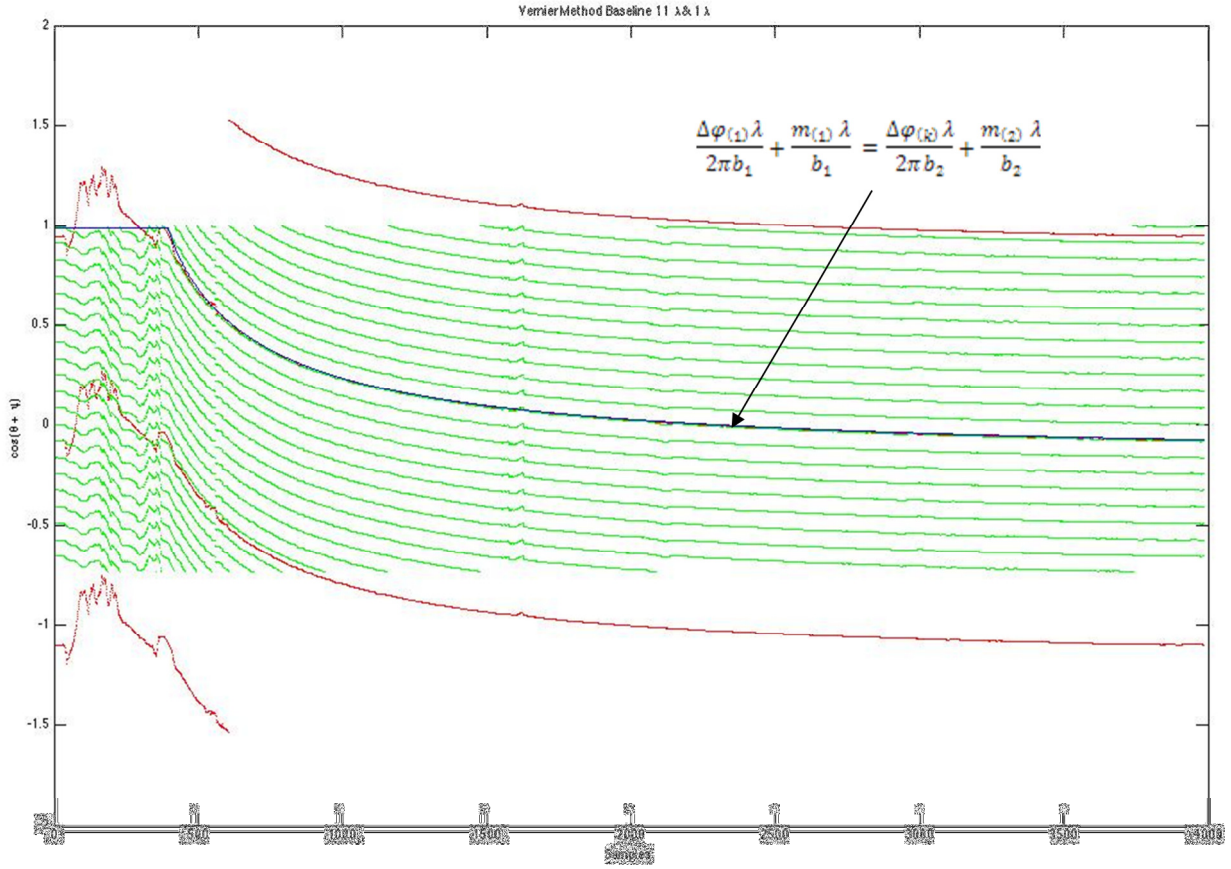

Figure 5.13 Vernier Method: the phase expressed as the direction of arrival *Cos(θ+ψ)* for the 1λ baseline in red and the 11λ baseline in green with the MUSIC direction of arrival in blue.

MUSIC is a method of eigenvalue decomposition of the correlation matrix, where the noise subspace is orthogonal to the signal noise subspace. The signal is projected on to the noise subspace providing null values at the true direction of arrival (see chapter 3for more details). The directions of arrival are given by the pseudo-spectral peaks (the inverse of the null-spectrum). Thus sources are resolved if the estimated null-spectrum contains nulls at or in the immediate neighborhoods of the true direction of arrival [Llort-Pujol 2007].

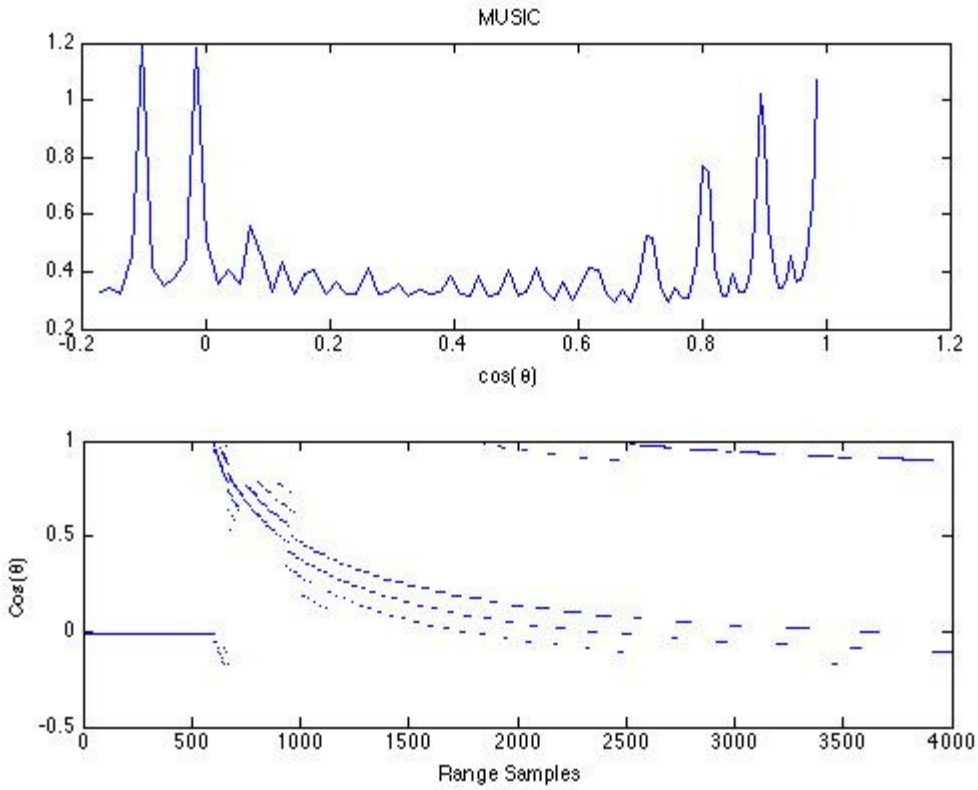

Figure 5.14 Music Algorithm: top plot is the Normalized pseudo-spectrum verse direction of arrival, bottom plot is the direction of arrival verse range.

I used MUSIC to obtain the direction of arrival and fused it with the direction of arrival derived using the vernier method. I was able to produce the bathymetric height for the whole scene with very accurate results, as shown in figure 5.15 where the cube height is found to be one meter.

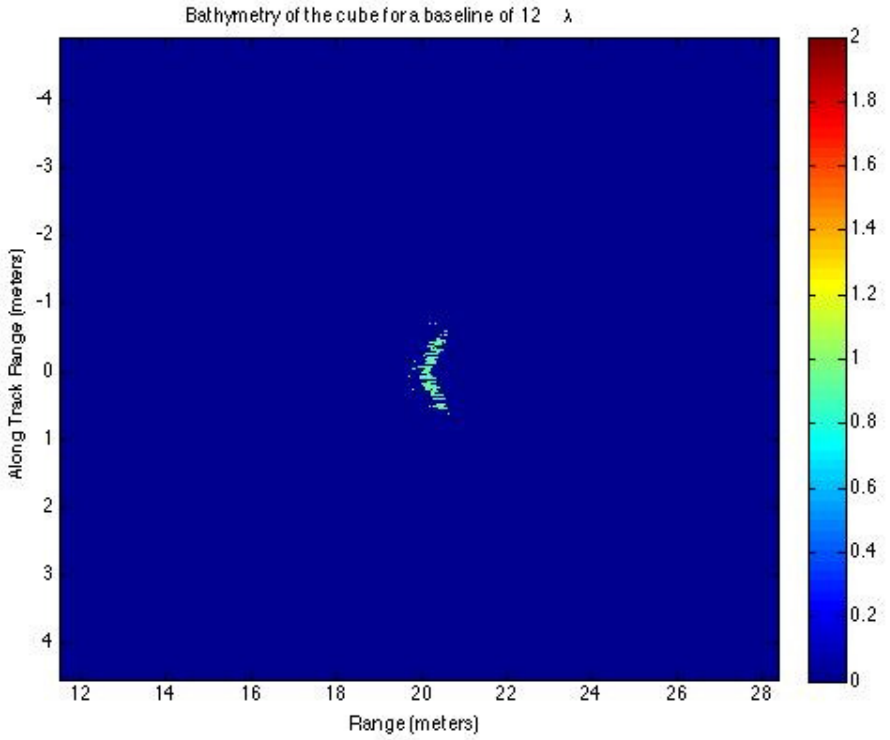

Figure 5.15 Bathymetry of the cube using the vernier method.

Array Calibration

On the first run of the vernier method, I noticed that the phase lines were crossing. The phase lines should remain parallel for each of the baselines. Figure 5.16 shows the crossings of the phase expressed as direction of arrival verse range. There are several possibilities for this discrepancy. It could be an error in the baseline measurement, misalignment in the baselines, and misalignment of the tilt angle.

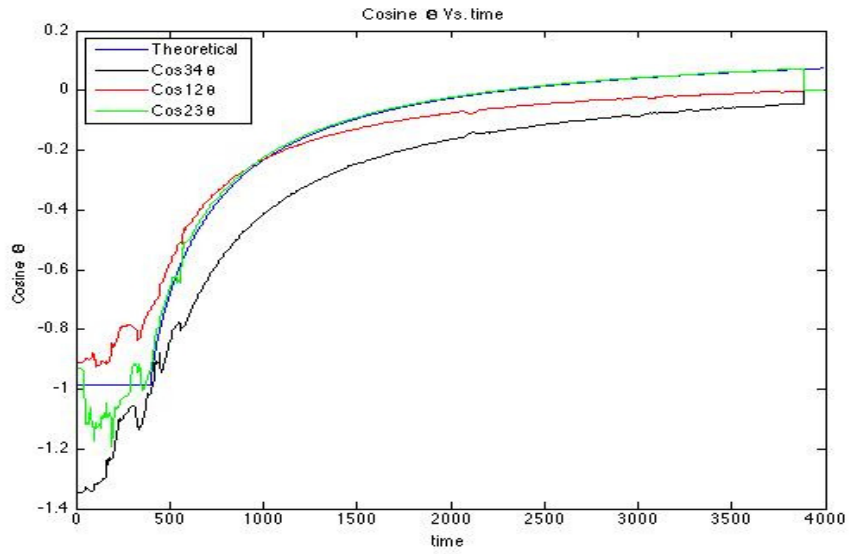

Figure 5.16 Error in the phase: seen as a crossing of the direction of arrival for each of the baselines. Theoretical in blue, 10 λ baseline in black, 11 λ baseline in red , and 1 λ baseline in green.

In this section I present a method to calibrate the array with *a priori* knowledge of the perceived seafloor, baseline, and tilt angle. I did a polynomial fit of the theoretical direction of arrival with the direction of arrival function of the baseline less the theoretical direction of arrival. I used the coefficients of the polynomial to obtain an error estimate. I used the mean and standard deviation to adjust the direction of arrival function. Figure 5.17 is the adjusted direction of arrivals, it can be seen that they are now parallel.

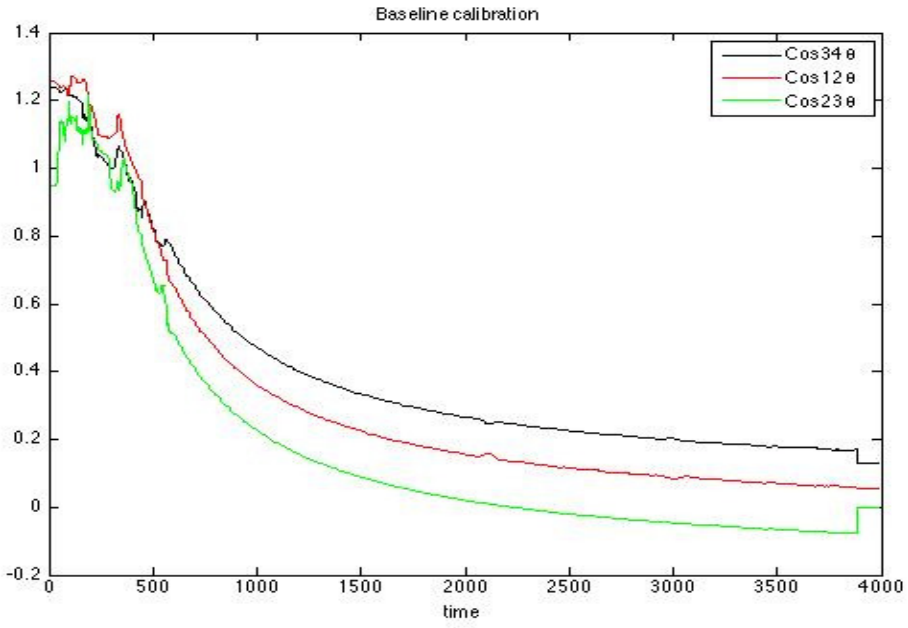

Figure 5.17 Adjusted direction of arrival.

To test the calibration, a single sounding for a baseline of twelve wavelengths in a flat area of the seafloor was used to calculate the measured cos(θ +ψ). It aligned precisely with the theoretical value and produced a relatively good bathymetric height.

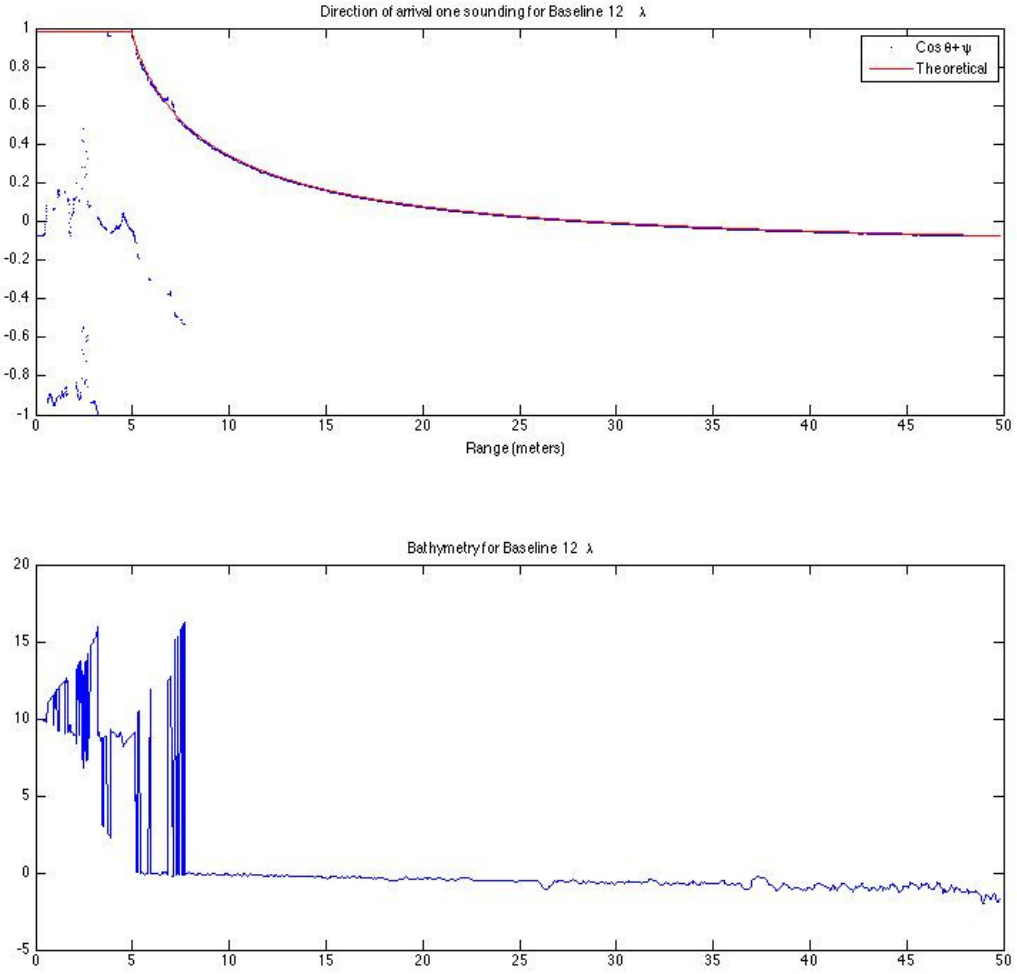

Figure 5.18 Calibrated direction of arrival and bathymetry for a single ping over a flat bottom.

I then tested the calibration over the cube and found a height of exactly one meter for the cube.

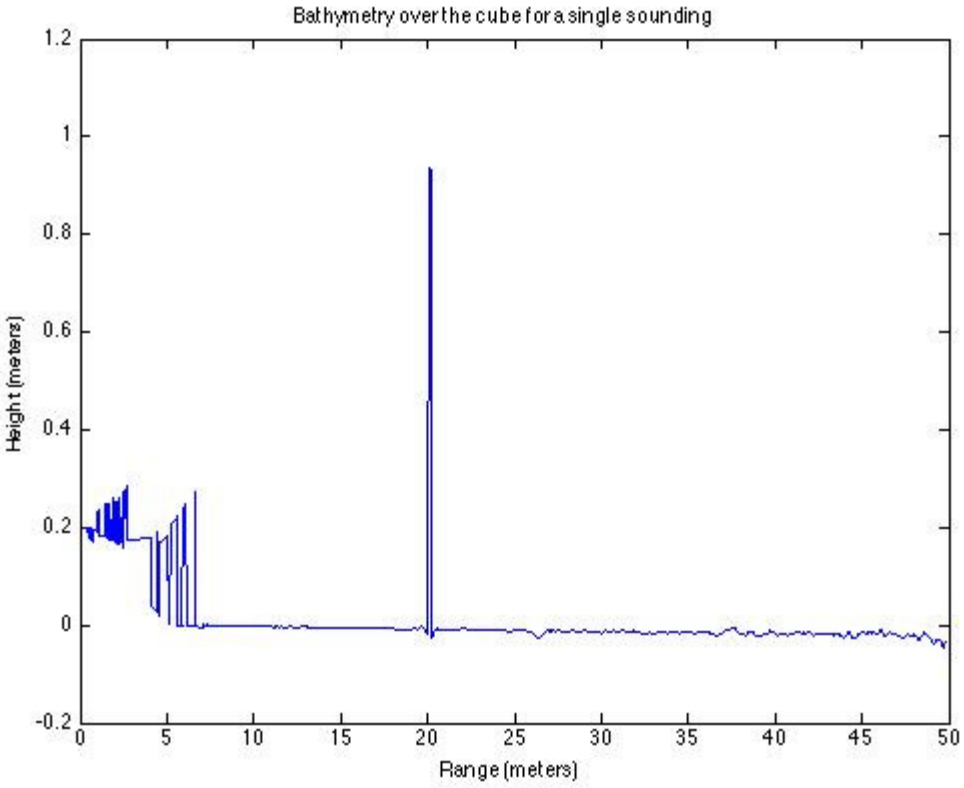

Figure 5.19 Bathymetry over the cube.

Robustness &Performance

Robustness and accuracy are the desired attributes. Computational time and memory consumption are the limiting factors in choosing a technique for a real time system. Methods for quantifying the robustness of the algorithm are: Standard deviation of the depth estimate as a function of the standard deviation of the phase, height sensitivity, height ambiguity, fringe frequency, critical baseline, baseline dependent coherence, computational speed, computational memory usage, noise susceptibility, phase accuracy, image accuracy and pixel resolution.

(Quantifying information about robustness and performance can be found in subsequent reports)

Summary

I produced an image of the seafloor using the chirp-scale beamforming technique. I unwrapped the phase difference using the vernier method for interferometry. I fused the direction of arrival from the vernier method with the direction of arrival obtained from the MUSIC algorithm to precisely produce bathymetric height for the cube.

Chapter 6

Conclusion

In this dissertation I presented basic principles for the phase based on underwater acoustics , a motion estimation and motion compensation technique for autonomous underwater vehicles, signal processing techniques for producing a SAS image, Interferometry and bathymetry as it pertains to InSAS systems, and finally the chirpscale-vernier-MUSIC algorithm.

Learn from the system

The Bayesian Regulation methods are best suited for InSAS systems operating in shallow water. Adaptive filtering methods MVDR, MUSIC, ESPRIT, are well suited for direction of arrival determination. The combined chirp-scale, vernier, MUSIC combination offers a stable solution to bathymetric height in a noisy environment.

Improvements over previous systems

The bathymetry obtained from previous methods was not as accurate as that from the chirp scale vernier method with MUSIC algorithm.

Future Developments

In the near future the research will continue with a fusion of the Bayes regulation methods with the vernier and cross correlation methods, develop a graphical user interface for the InSAS toolbox, develop an algorithm based purely on eigen value decomposition including filtering, motion compensation, beamforming and interferometry, and a comparison study of InSAS signal processing based on robustness and performance with emphasis on beamforming and phase unwrapping.

References

[1] Kattoush Abbas, "A new Recurrent Approach for Phase Unwrapping", Int. *J. App. Sci. Eng.*, vol. 3 iss. 2, 2005. pp. 135-143.

[2] Kannan Achan, Brendan j. Frey, Ralf Koetter, "A Factorized variation al technique for Phase unwrapping in Markov Random Fields", [Online] http://www.psi.toronto.edu/pubs/2001/mfpu-uai01.pdf, Probablistic and statistical Inference Group, University of Toronto, Canada, 2001.

[3] Piyush Agram, Howard Zebker, "Edgelist Phase Unwrapping Algorithm for Time Series InSAR analysis", *J. Opt Soc Am Image Sci Vis*, vol. 27, no. 3, Mar 1 2010, pp. 605-612.

[4] Jerome J. Akerson, Yingching Eric Yang, Yoshihisa Hara Bae-Ian Wu and Jin a. Kong, "Automatic Phase Unwrapping Algorithms in Syntehtic Aperture Radar (SAR) Interferometry ", *IEICE Trans. Electron., vo l E83-c*, no. 12, December 2000. pp. 1896 -1903.

[5] J.R. Apel, *Principles of Ocean Physics (International Geophysical Series Vol. 38),*San Diego, CA: Harcourt Brace Jovanovich ,1987.

[6] Akira Asada and Tamaki Ura, "Full-swath bathymetric survey system with synthetic aperture and triangle-arrayed interferometric techniques for autonomous underwater vehicle", *Oceans 2010,* 2010, pp. 1-6.

[7] Akira Asada and Tamaki Ura, Fumitaka Maeda, and Toshihiro Maki, "Sub-bottom synthetic aperture imaging sonar system using an AUV and an autonomous surface tracking vehicle for searching for buried shells of toxic chemicals", *Waterside SecurityConference 2010,* Marina di Carrara, Italy*,* 2010, pp. 1-3.

[8] Louis Nicolas Atallah, "Learning from Sonar Data for the Classification of Underwater Seabed", Ph.D. Thesis, University of Oxford, Oxford, United Kingdom, 2004.

[9] Shengxiang Bai, Jinsong Tang, Ming Chen, Sen Zhang, "Method of Phase Unwrapping-Free DEM Reconstruction of InSAS", *IEEE IASP 2010,* 2010, pp. 60 -63.

[10] SM Banks, HD Griffiths, TJ Sutton, " *A Technique for Interferometric Synthetic Aperture Sonar Image Processing",* UCL Press LTD, United Kingdom 2001.

[11] SM Banks, HD Griffiths, TJ Sutton, "Interferometric Synthetic Aperture Sonar", *London Communication Symposium*, UK 2000.

[12] SM Banks, TJ Sutton, HD Griffiths, "Noise susceptibility of phase unwrapping algorithms for interferometric synthetic aperture sonar", *Proc. Fifth ECUA 2000*, Lyons, France, July 2000, pp. 451-456.

[13] Barclay, Philip J., "Interferometric Synthetic Aperture Sonar Design and Performance", Ph.D. Thesis, University of Canterbury ChristChurch New Zealand August 2006.

[14] Barclay, Philip J., "Reconstructing seafloor bathymetry with multichannel broadband Insas using Belief Propagation", University of Canterbury ChristChurch New Zealand, pg 2149-2154, August 2006.

[15] P.J. Barclay, Michael P. Hayes, Peter T. Gough, "Bathymetric results from a multi-frequency InSAS sea trial", *Oceans 2006 Asia-Pacific*, Singapore, 2006, pp. 1-6.

[16] P.J. Barclay, Michael P. Hayes, Peter T. Gough, "ML estimation of seafloor topography using multifrequency Synthetic Aperture Sonar" , *Oceans Europe 2005*, Brest, France 2005, pp. 579 – 584.

[17] P.J. Barclay, Michael P. Hayes, Peter T. Gough, "Reconstructing seafloor bathymetry with a multichannel broadband InSAS using Belief Propagation", *Proc. Oceans 2003*, vol. 4, 2003, pp. 2149-2154.

[18] P.J. Barclay, Michael P. Hayes, Peter T. Gough, "Reconstructing seafloor bathymetry with a multichannel broadband InSAS", University of Canterbury ChristChurch New Zealand, 2002.

[19] Maurice Bellanger, *Digital Processing of Signals Theorey and Practice 2nd edition,* New York: John Wiley &Sons Ltd., 1989.

[20] Andrea Bellettini and Marc A. Pinto, "Theoretical Accuracy of Synthetic Aperture Sonar Micronavigation using Displaced Phase-Center Antenna*", IEEE J. Ocean Eng.,* vol. 27, no. 4, October 2002.

[21] Andrea Bellettini and Benjamin Evans, "Experimental results of a 300kHz Shallow water synthetic aperture sonar", NURC La Spezia, Italy, NURC-PR-2007-15, November 2007.

[22] Didier Billon, "About accuracy of the elevation angle measurement in interferometric synthetic aperture sonar", *Proc. Oceans 2005- Europe*, vol. 1, Brest, France, 2005, 10.1109/OCEANSE.2005.1511791, pp. 650-654.

[23] Didier Billon, Franck Fohanno, "Two improved ping-to-ping cross-correlation methods for synthetic aperture sonar: theory and sea results", *Proc. Oceans 2002 vol.4,* Biloxi, MS, October 2002, pp.2284 -2293.

[24] Didier Billon, M. A. Pinto, "Some General Considerations For Synthetic Aperture Sonar Design", *Proc. Oceans 1995*, San Diego, CA, *1995, pp. 1665-1670.*

[25] William W. Bonifant, "Interferometric synthetic aperture sonar processing", M.S. thesis, Georgia Institute of technology, Atlanta, GA, July 1999.

[26] William W. Bonifant, "Interferometric height estimation of the seafloor via synthetic aperture sonar in the presence of motion error", *IEE Proc. Radar Sonar Navig*., vol 147, no. 5, October 2000.

[27] William W. Bonifant, "An Analysis of the Effect of Motion and Phase Errors on the Implementation of Interferometric Processing by Synthetic Aperture Sonar", *Conf. record 3rd asilomar conf. sig. sys. comp., vol. 1, San Francisico, CA 1999, pp. 269 -273.*

[28] Newell O. Booth, Gary L. Mohnkern, *Signal-to-Noise Gain From Adaptive Matched-Field Beamforming of Multidimensional Acoustic Arrays. Technical Report 1661, September 1994.*

[29] Nathaniel Bowditch, " The American Practical Navigator, Pub No. 9, 2002 Bicentennial Edition", Bethesda, MD National Imagery and Mapping Agency, 2002.

[30] Ronald N. Bracewell, " The Fourier Transform and Its Application Third Edition", Boston, MA: McGraw-Hill, Inc. 2000.

[31] Henning Braunisch, Bae-Ian Wu, and Jin a. Kong, "Phase Unwrapping of SAR Interferogram after Wavelet Denoising", *IGARSS 2000*, vol. 2, Honolulu, Hi , 2001, pp. 752-754.

[32] Ramon Brcic, Michael Eineder, Richard Bamler, Ulrich Steinbrecher, Daniel Schulze, Robert Metzig, Konstantinos Papathanassiou(1), Thomas Nagler, Florian Mueller(2), Martin Suess , "Delta-K Wideband Sar Interferometry For Dem Generation And Persistent Scatterers Using Terrasar-X", *Proc. Fringe 2009 Workshop*, Franscati, Italy , December 2009.

[33] William S. Burdic, " Underwater Acoustic System Analysis (2nd Edition)", Los Altos, CA: Peninsula Publishing, 1990.

[34] Hayden J. Callow, Michael P. Hayes, Peter T. Gough, "Motion-Compensation Improvement for Widebeam, Multiple-Receiver SAS Systems*", IEEE J. Ocean Eng.,* vol. 34, no. 3, July 2009.

[35] Hayden J. Callow, Torstien Saebo, Roy E. Hansen, “Towards Robust Quality Assessment of SAS Imagery using the DPCA algorithm”, *Oceans 05 Europe*, Brest, France, June 2005.

[36] Hayden J. Callow, Roy E. Hansen, Torstien Saebo,, “Effect of Approximations in Fast Factorized Backprojection in Synthetic Aperture Imaging of Spot Regions”, *Oceans 06*, Boston, MA, September 2006, pp. 1-6.

[37] Hayden J. Callow, “Signal processing for Synthetic Aperture Sonar Image Enhancement”, Ph.D., Dissertation, University of Canterbury Christchurch, New Zealand, April 2003.

[38] Hayden J. Callow, Michael P. Hayes, Peter T. Gough, “Stripmap phase gradient autofocus”, *Proc. Oceans 2003*, pp. 2414-2421.

[39] Hayden J. Callow, Michael P. Hayes, Peter T. Gough, “Wavenumber domain reconstruction of SAR/SAS imagery using single transmitter and multiple-receiver geometry”, ELECTRONICS LETERS ,Vol. 38 No. 7, 28th March 2002, pp. 336-337.

[40] Hayden J. Callow, Michael P. Hayes, Peter T. Gough, “Noncoherent Auto focus of Single-Receiver Broad-Band Synthetic Aperture Sonar Imagery”, *Oceans 2001*, Honolulu, Hawaii 2001, pp. 157 -162.

[41] Hayden J. Callow, Michael P. Hayes, Peter T. Gough, “Autofocus of Multi-band, Shallow-water Synthetic Aperture Sonar Imagery using Shear-averaging”, IGARSS 2001 vol. 4, Syndney NSW Australia, 2001, pp. 1601 – 1603.

[42] G.F. Carballo, P.W. Fieguth, ‘Hierchical Netwrok Flow Phase Unwrapping*”, IEEE Trans. Geosci. Remote Sens.*, 2002. pp. 1695-1708.

[43] Gilles Le Chenadec, Jean-Marc Boucher, and Xavier Lurton, “Angular dependence of k-distribution sonar data”*, IEEE Trans. Geosci. Remote Sens*, vol. 45, no. 5, May 2007.

[44] Curtis W. Chen, “Statistical-Cost Network-Flow Approaches To Two Dimensional Phase Unwrapping For Radar Interferometry”, Ph.D. Dissertation, Stanford University, Stanford CA, 2001.

[45] Ming Chen, Sen Zhang, Jinsong Tang, “An Interferometric synthetic aperture sonar raw signal simulation based on points-scatterer model”, *Proc. ICSO 2009,* Hainan, China, April 2009, pp. 367 -369, doi: 10.1109/CSO.2009.442.

[46] Clarence S. Clay, Herman Medwin, *Acoustical Oceanography,* New York: John Wiley and Sons Inc., 1977.

[47] Daniel A. Cook, “*Synthetic Aperture Sonar Motion Estimation and Compensation*”, M.S. Thesis, Georgia Institue of Technology, Atlanta, GA, May2007. *Don’t use

[48] Philip N. Denbigh, “Swath Bathymetry: Principles of Operation and an Analysis of Errors”, *IEEE J Ocean Eng*., vol. 14, no. 4, October 1989.

[49] Jose M B Dias, Jose M.N. Leitao, “The Zπm Algorithm: A method for Interferometric Image Reconstruction in SAR/SAS”, *IEEE Trans. image proc.,* vol. 11, no. 4, April 2002.

[50] Jose M B Dias, Goncalo Valadao, “Phase Unwrapping via Graph Cuts ”, *IEEE Trans. Image Process.*, vol. 16, no. 1, 2007.

[51] Ying Dong and Jim Ji, ” Phase Unwrapping Using Region-Based Markov Random Field Model", *IEEE 32nd Annual Int. Conf. EMBS,* Buenos Aires, Argentina, August 2010.

[52] E. Ertin R.L. Moses L.C. Potter, " Interferometric methods for three-dimensional target reconstruction with multipass circular SAR", *IET Radar Sonar Navig*., 2010, vol. 4, iss. 3, 2009, pp. 464–473.

[53] Qianqian Fang, Paul M. Meaney, and Keith D. Paulsen, " The Multidimensional Phase Unwrapping Integral and Applications to Microwave Tomographical Image Reconstruction", *IEEE Trans. Image Proc.,* vol. 15, no. 11, November 2006, pp. 3311-3324.

[54] Wang Feng, Wu Gang, Veronique Prinet, and Ren Kun, " Phase Unwrapping Based on Active Contour Model", *Proc. IGARSS 2003*, vol. 7, July 2003, pp. 4386-4388.

[55] Christopher J. Forne, "3-D Scene Reconstruction from Multiple Photometric Images", Ph.D., Dissertation, University of Canterbury Christchurch, New Zealand, April 2007.

[56] Steven A. Fortune, "Phase Error Estimation for Synthetic Aperture Imagery", Ph.D., Dissertation, University of Canterbury Christchurch, New Zealand, June 2005.

[57] Terje G. Fossum, Torstein Olsmo Sæbø, Bjørnar Langli, Hayden Callow, Roy Edgar Hansen, "HISAS 1030 - High resolution interferometric synthetic aperture sonar", *Proc. Canadian Hydro. Conf. Nat. Surveyors Conf. 2008,* Victoria British Columbia, 2008.

[58] A. Ganse, Christophe, *An introduction to beamforming,* http://staff.washington.edu/aganse/beamforming/beamforming.html, 2003.

[59] R. Garello, Christophe Sintes, Didier Gueriot and J.-M. Nicolas, *Radar and Sonar interferometry,* www.acoustics08-paris.org June 2008.

[60] Dennis C. Ghiglia, Mark D. Pritt, *Two-Dimensional Phase Unwrapping Theory, algorithms, and Software*, New York: John Wiley & sons, Inc, 1998.

[61] Peter Gerstoft, "Inversion of seismoacoustic data using genetic algorithms and a posteriori probability distributions", *J. Acoust. Soc. Am*, vol. 95, no. 2, February 1994, pp. 770-782.

[62] Richard M. Goldstein, Howard a. Zebker and Charles L. Werner, " Satelite Radar Interferometry: Two Dimensional Phase Unwrapping", *Radio Science*, vol. 23, no. 4 July 1988, pp. 713-720.

[63] Peter T. Gough, Michael P. Hayes, "A simulation model of the pulse returns for a short-range SAS', *Oceans 2010,* Sydney Australia, 2010.

[64] Peter T. Gough, Michael P. Hayes, "Ten Key Paper in Synthetic Aperture Sonar", *Acoustics 08 Paris*, Paris, 2008.

[65] Peter T. Gough, M. A. Noonchester, A.J. Hunt, Michael P. Hayes, "Towards multi-frequency imaging and analysis of sub-surface targets using SAS", *Oceans 2006,* Boston, MA 2006.

[66] Peter T. Gough, Michael P. Hayes, "Fast Fourier technique for SAS imagery", *Oceans Europe 2005*, Brest, France 2005.

[67] Peter T. Gough, and M. A. Miller, "The SAR map-drift algorithm extended for a multi hydrophone SAS", *Proc. Oceans 2003,* vol.5 pp. 2427-2432, 2003.

[68] Peter T. Gough, and R.G. Lane, "Autofocusing SAR and SAS imaging using Conjugate Gradient Search Algorithms", IGARSS vol.2, pp.621 – 623, 1998.

[69] Peter T. Gough, and David W. Hawkins,''A short history of Synthetic Aperture Sonar", IGARSS vol.2, pp. 618-620, 1998.

[70] Peter T. Gough, and Bobby R. Hunt, "Synthetic Aperture Radar Image Reconstruction Algorithms Designed for subsurface imaging" , IGARSS 1997, vol.4, pp. 188 – 1590, 1997.

[71] Peter T. Gough, and David W. Hawkins, "Unified Framework for Modern Synthetic Aperture Imaging algorithms" *in International Journal of Imaging Systems and Technology*, vol 8, issue 4, John Wiley & Sons, Inc., 1997, pp. 343–358.

[72] Peter T. Gough, and David W. Hawkins, "Imaging Algorithms for Strip-Map Aperture Sonar: Minimizing the effects of aperture errors and aperture undersampling", *IEEE J. Ocean Eng*., Vol. 22, N0. 1, January 1997.

[73] Peter T. Gough, and David W. Hawkins,"On the use of mapping operators on SAR and SAS", *Rec. 13th Asilomar Conf. Signals, Systems and Computers 1996,* vol.1, 1996, pp. 86-89.

[74] Peter T. Gough, "A Fast spectral estimation algorithm based on the FFT"*, IEEE Trans. Signal Process.*, Vol. 42, No. 6, June 1994.

[75] Peter T. Gough, "Side-looking sonar or radar using phasedifference monopulse techniques coherent and noncoherent applications"*,* IEEE Proc. Comm, Radar, Sig process., Vol 130, No5, August 1983, pp. 392 -398.

[76] HD Griffiths, TA Rafik, Z. Meng, C.F.N. Cowan, H. Shafeeu, D.K. Anthony, "Interferometric Synthetic Aperture Sonar for high-resolution 3-D mapping of the seabed", *IEE Proc-Radar, Sonar Navig*, vol. 144 no. 2, April 1997.

[77]Johannnes Groen, Roy Edgar Hansen, Hayden John Callow, Jan Cees Sabel and Torstein Olsmo Saebo, "Shadow Enhancement in Synthetic Aperture Sonar Using Fixed Focusing", *IEEE J. Ocean Eng*., vol. 34, no. 3, JULY 2009, pp. 269-284.

[78] Johannnes Groen, "Adaptive motion compensation in sonar array processing", PhD Thesis Technical University of Delft, Netherlands , June 2006.

[79] Didier Gueriot, Christophe Sintes, and Rene Garello, "Sonar Data Simulation based on Tube Tracing"*, Oceans 2007 Europe*, Aberdeen Scotland, 2007, pp. 1-6.

[80] Laurent Guillon, Xavier Lurton, "Backscattering from buried sediment layers: The equivalent input backscattering strength model"*, J. Acoust. Soc. Am.*, vol. 109 no. 1, January 2001, pp. 122-131.

[81] Per Espen Hagen and Roy E. Hansen, "Robust Synthetic Aperture Sonar Operations for AUV's", *Oceans 2009*, Biloxi, MS, USA, October 2009.

[82] Per Espen Hagen Terje G. Fossum and Roy E. Hansen, "Applications of AUV's with SAS", *Oceans 2008*, Quebec City, Quebec Canada, October 2008.

[83] Per Espen Hagen and Roy E. Hansen, "Area Coverage Rate of Synthetic Aperture Sonars", *Oceans 2007*, Vancouver, British Columbia, Canada, September 2007.

[84] Per Espen Hagen, Roy E. Hansen, Bjorn Lagnli, "Interferometric Synthetic Aperture Sonar for the HUGIN 1000-MR AUV", *UDT Pacific 2006*, San Diego, CA, 2006.

[85] Per Espen Hagen Nils Storkersen, Bjorn-Erik Marthinsen, Geir Sten, Karstein Vestgard, "Military Operations with HUGIN AUV's Lessons Learned and the way ahead", *Oceans 2005*, Washington, D.C., 2005.

[86] Per Espen Hagen, Kenneth Grade, Ove Kent Hagen, "A toolbox of aiding techniques for the Hugin AUV Integrated Inertial Navigation System", *Oceans 2003*, San Diego, CA, September 2003.

[87] Per Espen Hagen, Roy E. Hansen, Kenneth Grade, Erik Hammerstad, "Interferometric Synthetic Aperture Sonar for AUV based Mine Hunting, The SENSOTEK project", *Unmanned Sytems 2001*, Baltimore, MD, USA, July-August 2001.

[88] Roy E. Hansen, Torstien Olsom Saebo, Hayden John Callow and Per Espen Hagen, "Synthetic Aperture Sonar in Pipeline Inspections", *IEEE Proc. Oceans 2010,* Sydney, Australia 2010, pp. 1-10.

[89] Roy E. Hansen, Per Espen Hagen and Helge S Telle " Synthetic Aperture Sonar: A Tool In Underwater Archaeology", *UAM Conf. 2009*, Naplion, Greece, June 2009.

[90] Roy E. Hansen, Torstien Olsom Saebo, Hayden John Callow and Per Espen Hagen, "Synthetic Aperture Sonar for the Hugin AUV", *IEEE Proc. Oceans 2005 Europe*, Brest, France, vol. 2, 2005.

[91] Roy E. Hansen, Torstien Olsom Saebo, Kenneth Grade, Sean Chapman, "Signal processing for AUV based Interferometric Synthetic Aperture Sonar", *IEEE Proc. Oceans 2003*, San Diego, CA, vol. 5, 2003, pp. 2438 -2444.

[92] Alfred Hanssen, Jonas Kongsli, Roy E. Hansen, Sean Chapman, "Statistics Synthetic Aperture Sonar Images", *IEEE Proc. Oceans 2003*, San Diego, CA, vol. 5, 2003, pp. 2635 -2440.

[93] J. Kent Harbaugh, Daniel D. Sternlicht, Angela Putney, Mark D. Tinkle, "Acoustic Modeling for Sea-Mine CAD/CAC Development", *Oceans 2005,* Washington, D.C., 2005.

[94] David W. Hawkins, Peter T. Gough, "An accelerated chirp scaling algorithm for synthetic aperture Imaging", IGARSS 1997, vol.1, pp. 471 – 473, 1997.

[95] David W. Hawkins, "Synthetic Aperture Imaging Algorithms with application to wide bandwidth sonar", Ph.D. thesis University of Canterbury Christchurch, New Zealand October 1996.

[96] Michael P. Hayes, Peter T. Gough, "Synthetic Aperture Sonar: A Review of Current Status", *IEEE J. Ocean Eng.,* vol. 34, no. 3, July 2009.

[97] Michael P. Hayes, Peter T. Gough, "Interferometric synthetic aperture processing a comparison of sonar and radar", *Acoustics 08 Paris*, Paris, 2008.

[98] Michael P. Hayes, "Volumetric InSAS reconstruction using belief propogation", *IVCNZ 2008,* New Zealand, 2008.

[99] Michael P. Hayes, A. J. Hunter, P.J. Barclay, Peter T. Gough, "Estimating layover in Synthetic Aperture Sonar Bathymetry", *Oceans Europe 2005,* Brest, France 2005.

[100] Michael P. Hayes, Peter T. Gough, "Synthetic aperture sonar a mature discipline", *Proc 7th ECUA 2004*, Delft, The Netherlands, 5-8 July, 2004.

[101] Michael P. Hayes, "Multipath reduction with a three element interferometric Synthetic aperture sonar", *Proc 7th ECUA 2004*, Delft, The Netherlands, 5-8 July, 2004.

[102] Michael P. Hayes and Philip Barclay, "The effects of multipath on a bathymetric synthetic aperture sonar using belief propagation", *IVCNZ 2003, Palmerston North,* New Zealand, 2003.

[103] Michael P. Hayes, P.J. Barclay, Peter T. Gough and H. J. Callow, "Test results from a Multi-Frequency Bathymetric Synthetic Aperture Sonar", *Oceans 2001 ,* Honolulu, HI 2001.

[104] Michael P. Hayes, Peter T. Gough, *Broadband Synthetic Aperture Sonar*, IEEE J. Ocean Eng., vol 17, no 1, January 1992, pp.80-94.

[105] Simon Haykin, "Adaptive Filter Theory (4th Edition)", Upper Saddle River, N.J.: Prentice Hall 2002.

[106] Oyvind Hegrenaes, Torstien Olsom Saebo, Per Espen Hagen, Bjorn Jalving, "Horizonatl Mapping Accuracy in Hydrographic AUV Surveys", IEEE/OES *AUV*, 2010.

[107] Laurent Hellequin, Jean-Marc Boucher, and Xavier Lurton, "Processing of High-Frequency Multibeam Echo Sounder Data for Seafloor Characterization" IEEE J. Ocean Eng., vol. 28, no. 1, January 2003.

[108] R. Heremans, A. Bellettini, M. Pinto. (2006 September 28). *Milestone Displaced Phase Center Array*, [Online], http://www.sic.rma.ac.be/~rhereman/milestones/dpca.pdf , 2006.

[109] Roel Heremans, Marc Acheroy, Yves Dupont, "Motion compensation of synthetic aperture sonar images" *in Advances in Sonar Technology, Book edited by: Sergio Rui Silva,* I-Tech, Vienna, Austria, February 2000.

[110] Jasper M. Horrell, "*Range-Doppler Synthetic Aperture Radar"*, Ph.D. thesis University of Cape Town, South Africa, May 1999.

[111] Wen-Hsin Hsiao, "*Aspects of Fourier Imaging"*, Ph.D. thesis University of Canterbury Christchurch, New Zealand May 2008.

[112]Alan J. Hunter, "*Underwater Acoustic Modelling for Synthetic Aperture Sonar"*, Ph.D. thesis University of Canterbury Christchurch, New Zealand June 2006.

[113] Alan J. Hunter, Michael P. Hayes, "Towards more accurate shadow models for Simulating SAS Imagery", *Oceans Europe 2005,* Brest, France, 2005, pp. 713 -718.

[114] Alan J. Hunter, Michael P. Hayes, Peter T. Gough, "Simulations of multiple receiver Broadband Interferometric SAS Imagery", *Proc. Oceans 2003*, vol. 5, 2003, pp. 2629-2634.

[115] Alan J. Hunter, Michael P. Hayes, Peter T. Gough, "Using a faceted rough surface environmental model to simulate shallow-water SAS imagery", University of Canterbury ChristChurch New Zealand, 2002.

[116] Finn B. Jensen, William A Kuperman, Michael B. Porter, Henrick Schmidt, *Computational Underwater Acoustics*, Woodbury, NY: AIP Press, 1994.

[117] Yun Jun, Zhi-nong Zou, Jin-song Tang, Ai-Qing Wang,"Experiment of Phase Unwrapping Algorithm in Interferometric Synthetic Aperture Sonar", *Proc. IEEE 8th ACIS, 2007*. vol. 3, Qingdao, China, 2007, pp. 937-942.

[118] J.H. Justice N. L. Owsley, J.L. Yen, A.C. Kak , *Array Signal Processing*, Englewood Cliffs, NJ: Prentice Hall 1985.

[119] Sam T. Kaplan, Tadeusz J. Ulrych," Phase Unwrapping: A Review of Methods and a Novel Technique", *2007 CSPG CSEG conv*., Calgary, Alberta Canada , 2007, pp. 534-537.

[120] Vladimir Katkovnik and Jos´e Bioucas-Dias, "Multi-frequency Phase Unwrap from Noisy

Data: Adaptive Least Squares Approach"*, AIP Proc. Int. Conf. adv phase meas. Methods optic and imaging,* vol. 1236, Monte Verita Locarno, Switzerland, May 2010, pp. 472-478.

[121] Lawrence E. Kinsler, Austin R. Frey, Alan B.Coppens, James V. Sanders, *Fundamentals of Acoustics Third Edition*, New York, NY: John Wiley & Sons Inc., 1982.

[122] Ivars P. Kirsteins, "Blind Separation of Signal and Multipath Interference for Synthetic Aperture Sonar", NUWC, Newport RI, September 2003.

[123] E. Krajnik, "A simple and reliable phase unwrapping algorithm," in J. Vandewalle et al. (eds.), *Signal Processing VI: Theories and Applications,* Elsevier, Amsterdam 1992, pp. 917-919.

[124] Rainer Kramer and Otmar Loffeld, "Presentation of an improved Phase Unwrapping Algorithm based on Kalman filters combined with local slope estimation", *Fringe 96 workshop*, [Online] http://earth.esa.int/workshops/fringe_1996/kraemer/, 1996.

[125] N. Liu L.-R. Zhang X. Liu Y. Zhou, "Multibaseline InSAR height estimation through joint covariance matrix fitting", IET Radar Sonar Navig., vol. 3, iss. 5, 2009, pp. 474–483.

[126] Gerard Llort-Pujol, Christophe Sintes, Didier Gueriot, "Vernier interferometer performance analysis", *presented at Oceans 2011, Kona Hawaii, 2011.*

[127] Gerard Llort-Pujol, Christophe Sintes, "Interferometric angle estimation for bathymetry performance analysis", *presented at Oceans 2011, Santander Spain*, *2011,* doi: 10.1109/Oceans-Spain.2011.6003387 pp 1-8.

[128] Gerard Llort-Pujol, Christophe Sintes, Thierry Chonavel, Didier Gueriot, Rene Garello, "Simulations on large scale of acoustic signals for array processing", hal-00488717, version 1 – 2 June 2010.

[129] Gerard Llort-Pujol, Christophe Sintes, Didier Gueriot, "Statistical modeling of interferometric signals in underwater applications", hal-00485297, version 1 – 20 May 2010.

[130] Gerard Llort-Pujol, Christophe Sintes, Didier Gueriot, "Analysis of Vernier Interferometers for sonar bathymetry", *presented at Oceans 2008, Quebec city ,2008, QC*, *pp 1-5,* doi: 10.1109/OCEANS.2008.5151958.

[131] Gerard Llort-Pujol, Christophe Sintes, X. Lurton, "Improving spatial resolution, of interferometric bathymetry in multibeam echosounders", *presented at* www.acoustics08-paris.org, Paris France, June 2008.

[132] Gerard Llort-Pujol, "Amelioration de la resolution spatiale des sondeurs multifaisceaux (improvements of the spatial resolution of multibeam sonars)", PhD Thesis, L'Ecole Nationale Superieure des Telecommunications de Bretagne France, 14 December 2007.

[133] Gerard Llort-Pujol, Christophe Sintes, X. Lurton, "A new approach for fast and high resolution interferometric bathymetry", *presented at Oceans 2006 – Asia Pacific, Singapore*, May 2006, doi: 10.1109/OCEANSAP.2006.4393899.

[134] Gerard Llort-Pujol, Christophe Sintes, X. Lurton, "High resolution interferometry for multibeam echosounder", *presented at Oceans 2005- Europe*, Brest, France, Doi: 10.1109/OCEANSE.2005.1511738, pp 345-349.

[135] Otmar Loffeld, Rainer Kramer, "Phase Unwrapping for SAR Interferometry", IGARSS 1994,,vol. 4, Pasedena, CA, 1994, pp. 2282-2284.

[136] Xavier Lurton, *An Introduction to Underwater Acoustics Principles and Applications Second Edition*, Chichester, UK: Springer – Praxis, 2010.

[137] Xavier Lurton, "Swath Bathymetry Using Phase Difference: Theoretical Analysis of Acousitcal Measurement Precision", *IEEE J. Ocean Eng.,* vol. 25, no. 3, July 2000.

[138] Juan J. Martinez-Espla, Tomas Martinez-Marin, Juan M. Lopez-Sanchez, "An Optimized Algorithm for InSAR Phase Unwrapping Based on Particle Filtering, Matrix Pencil, and Region Growing Techniques", *IEEE Geosci. And Remote Sens. Lett.*, vol. 6, no. 4, October 2009

[139] J uan J. Martinez-Espla, Tomas Martinez-Marin, Juan M. Lopez-Sanchez,and J. David Ballester-Berman, "InSAS Phase Unwrapping by Means of a Particle Filter", *IGARSS 08*, Boston MA, July 2008.

[140] D Marx, M Nelson, E Chang, W Gillespie, A Putney, K Warman (2000): "An Introduction to Synthetic Aperture Sonar", *IEEE Signal Proc. Workshop on Statistical Signal and Array Processing*, 2000, pp. 717-721.

[141] S. Lawrence Marple, Jr., *Digital Spectral Analysis with Applications*, Englewood Cliffs NJ: Prentice Hall, 1987.

[142] Goncalo Ramiro Valadao Matias, "Radar Interferometry: 2D Phase Unwrapping Via Graph Cuts", M.S. thesis, Universidade Tecnica De Lisboa Instituto Superior Tecnico, Lisbon, Portugal, July 2006.

[143] Oivind Midtgaard, Torstein 0. Saebo and Hayden J. Callow, "Detection of Short-Tethered Objects with Interferometric Synthetic Aperture Sonar", *presented at Oceans 2007*, Vancouver, British Columbia Canada, 2007.

[144] O. Monserrat, M. Crosetto, R. Iglesias, G. Rossi, L. Calcagni, B. Crippa, "A TOOL FOR 2+1D PHASE UNWRAPPING: APPLICATION EXAMPLES", *Proc. Fringe 2009 Workshop*, Franscati, Italy , December 2009.

[145] Christian de Moustier, "Empirical Uncertainty in angle of arrival estimation for bathymetric sidescan sonars", *presented at Oceans 2011*, Kona Hawaii, 2011.

[146] Christian de Moustier, "Time and angle of arrival uncertainties in echo sounding", *presented at Oceans 2011*, Kona Hawaii, 2011.

[147] Christian de Moustier, "Autonomous Swath Bathymetry Surveys with a Hybrid Sonar", HLS Research La Jolla, Ca, SBIR Topic N091-088 Phase II, 2011.

[148] Christian de Moustier, "Sidescan Sonar Methods (single & Multi-row)", C. de Moustier 2011.

[149] G. Nico1, J. Fortuny-Guasch1, J. M. Lopez-Sanchez2, L. Sagues3 and A.J. Sieber, "Coherence Optimization by Polarimetric Interferometry for Phase Unwrapping", *Proc. IGARSS 2000*, vol. 1, Honolulu, HI, July 2000, pp. 135-137.

[150] Mark Noonchester, "A Broadband Approach to Measuring Acoustic Impedance and Roughness using Spherical Hydrophones", Ph.D. thesis University of Canterbury Christchurch, New Zealand, August 2010.

[151] Batuhan Osmanoglu, Shimon Wdowinski, Timothy H. Dixon, Juliet Biggs, "InSAR Phase Unwrapping based on Extended Kalman Filtering", *IEEE Radar Conf. 2009*, Pasedena, CA, May 2009.

[152] Alan V. Oppenheim and Ronald W. Schafer, *Discrete-Time Signal Processing*, Englewood Cliffs NJ: Prentice Hall, 1989.

[153] Mounira Ouarzeddine, Aichouche Belhadj-Aissa, Mutapha Rbihi & Farid Tabarout, "Filtering of InSAR interferograms", *25th EARSel Symposium*, Porto, Portugal, June 2005.

[154] Yan Pailhas, Yvan Petillot, Chris Capus, "High-Resolution Sonars: What Resolution Do We need for Target Recognition", *EURASIP J. Adv Signal Proc*, vol. 2010 art. Id 205095, 2010.

[155] Yvan Petillot, Yan Pailhas, J. Sawas, N. Valeyrie, J. Bell, "Target Recognition in Synthetic Aperture and High Resolution Side-Scan Sonar", *High Resolution Imaging and Target Classification 2006,* The Inst. Of Eng. And Tech. Seminar, 12 March 2007.

[156] Edward N. Pilbrow, "Synthetic Aperture Sonar Micronavigation Using an Active Acoustic Beacon", Ph.D. thesis University of Canterbury Christchurch, New Zealand, January 2007.

[157] Marc Pinto, Andrea Bellettini, "Shallow water synthetic aperture sonar: an enabling technology for NATO MCM forces", NATO Undersea Research Center NURC-PR-2007-010, June 2007.

[158] Marc Pinto, "Design of synthetic aperture sonar systems for high-resolution seabed imaging (tutorial slides)", NATO Undersea Research Center NURC-PR-2006-029, October 2006.

[159] Marc Pinto, Andrea Bellettini, Lian Sheng Wang, Peter Munk, Vincent, Myers, and Lucie Pautet, "A New Synthetic Aperture Sonar Design with Multipath Mitigation", *AIP Conf. Proc. High Frequency Ocean Acoustics,* vol. 728, November 2004.

[160] M. Pinto, "High Reseolution Seafloor Imaging with Synthetic Aperture Sonar", *OES Newsletter,* 2002.

[161] M. Pinto, R. Hollett, A. Bellettini, S. Chapman, "Bathymetric imaging with wideband interferometric synthetic aperture sonar", *Submitted IEEE J. Ocean Eng., 2001*.

[162] M. Pinto, R. Hollett, A. Bellettini, J. Edwards, "Results of wideband interferometric synthetic aperture sonar experiments", 5-iemes Journees d'Etudes Acoustique Sous-Marine 30/11-1/12 2000, Brest, France, 2000.

[163] M. A. Pinto, A. Bellettini, S. Fioravanti', S.Chapman, D.R Bugle, Y. Perrot, A. Hetet, "Experimental Investigations Into High Resolution Sonar Systems", *Proc. Oceans 99,* vol. 2, Seattle, WA, 1999, pp. 916-922.

[164] A. Potsis, A. Reigber, E. Alivizatos, A. Moreira and N. Uzunoglu, "Comparison Of Chirp Scaling and wavenumber Domain Algorithms For Airborne Low frequency SAR Data Processing"*, Proc. SPIE, vol. 4883, 2003, pp. 11-19.*

[165] John G. Proakis, Charles M. Rader, Fuyun Ling, Chrysostomos L. Nikias*, Advanced Signal Processing* (Macmillan Publishing Comparny NY 1992)

[166] A. Putney, E. Chang, R. Chatham, D. Mark, M. Nelson, L. K. Warman, , "Synthetic Aperture Sonar- The Modern Method of Underwater Remote Sensing*, IEEE Proc. 2001 Aerospace Conf.,* March 2001.

[167] Xu Qing, Jin Guowang, Zhu Caiying, Wang Zhengde, He Yu , Yang Peizhang, "The Filtering and Phase Unwrapping of Interferogram", *Proc. ISPRS XXXV Comm V1/WG4***,** Istanbul, Turkey, 2004.

[168] I. Quidu, J. Ph. Malkasse, G. Burel, P. Vilbé, "A 2-D Filter Specification For Sonar Image Thresholding", ACIVS 2001, HAL: hal-00504839, version 1, Baden-Baden, Germany, July 2001.

[169] A. Reigber, E. Alivizatos, A. Potsis and A. Moreira*,* " Extended wavenumber-domain synthetic aperture radar focusing with integrated motion compensation"*,* IEE Proc.-Radar Sonar Navig., Vol. 153, No. 3, June 2006.

[170] A. Reigber, A. Potsis, E. Alivizatos, N. Uzunoglu, and A. Moreira*,* " Wavenumber Domain SAR Focusing with Integrated Motion Compensation"*, IGARSS 2003*, Toulouse, France, July 2003, pp.1465-1467.

[171] Mark A. Richards*,* " A Beginner's Guide to Interferometric SAR Concepts and Signal Processing"*,* IEEE A&E Systems Magazine, vol. 22, no. 9, September 2007.

[172] K.D. Rolt, "Ocean, platform, and signal processing effects on synthetic aperture sonar performance", PhD Dissertation, Department of Ocean Engineering, Massachusetts Institute of Technology, Cambridge, MA 02139, February 1991.

[173] Paul A. Rosen, Scott Hensley, Ian R. Joughin, Fuk K. Li, Søren N. Madsen, , Ernesto Rodríguez, And Richard M. Goldstein, " Synthetic Aperture Radar Interferometry", PROC. IEEE, vol. 88, no. 3, March 2000.

[174] Torstein Olsom Saebo, "Seafloor Depth Estimation by means of Interferometric Synthetic Aperture Sonar", Ph.D. Dissertation, Univeristy of Tromso, Norway, September 2010.

[175] Torstein Olsmo Sæbø, Roy Edgar Hansen and O. Midtgaard , "Filtering of High Resolution Interferometric Synthetic Aperture Sonar Data", *IACM 4th UAM 2009*, Promitheas, Greece, June 2009.

[176] Torstein Olsmo Sæbø, Roy Edgar Hansen and Alfred Hanssen, "Relative Height Estimation by Cross-Correlating Ground-Range Synthetic Aperture Sonar Images", IEEE J.Ocean Eng., vol. 32, no. 4, October 2007.

[177] Torstein Olsmo Sæbø, Hayden John Callow, and Roy Edgar Hansen , Bjomar Langli and Erik O. Hammerstad, "Bathymetric Capabilities of the HISAS Interferometric Synthetic Aperture Sonar, *Oceans 2007*, Vancouver, British Columbia, Canada, September 2007, pp. 1-10.

[178] Torstein Olsmo Sæbø, Hayden John Callow, and Roy Edgar Hansen , "Synthetic Aperture Sonar Interferometry: Experimental Results From Sensotek", *Proc. 8th ECUA*, Carvoeiro, Portugal, June 2006.

[179] Torstein Olsmo Sæbø, Roy Edgar Hansen and Hayden John Callow, "Height Estimation on Wideband Synthetic Aperture Sonar: Experimental Results from InSAS-2000", *Oceans 2005*, Washington, D.C. , September 2005.

[180] Alan V. Oppenheim, Ronald W. Schafer, " Discrete Time Signal Processing", Englewood Cliffs, NJ: Prentice Hall, 1989.

[181] T.O. Saebo, R. E. Hansen, "Bathymetric Imaging Using Synthetic Aperture Sonar", *Proc. 7th ECUA 2004*, Delft, The Netherlands, 5-8 July 2004.

[182] Charlotte Sanchis, "Signal Processing Techniques for the Enhancement of Marine Seismic Data ", Ph.D. Dissertation, Univeristy of Tromso, Norway, September 2010.

[183] Sergio Rui Silva, Sergio Cunha, Anibal Matos, Nuno Cruz, "Synthetic Aperture Techniques for Sonar System" in *Advances in Sonar Technology*, [Online] http://www.intechopen.com/books/show/title/advances_in_sonar_technology, February 2009.

[184] Sergio Rui Silva, Sergio Cunha, Anibal Matos, Nuno Cruz, "Shallow Water Surveying Using Experimental Interferometric Synthetic Aperture Sonar", *MTS J. Student papers*, vol. 43, No. 1, 2009.

[185] Sergio Rui Silva, Sergio Cunha, Anibal Matos, Nuno Cruz, "Sub-Band Processing Synthetic Aperture Sonar System", *IEEE Oceans 2008,* Quebec City, QC, pp. 1-8.

[186] Sergio Rui Silva, Sergio Cunha, Anibal Matos, Nuno Cruz, "Shallow Water Height Mapping with Interferometric Synthetic Aperture Sonar", *Oceans 2008*,Quebec City, Quebec, Canada, September 2008, pp. 1-7.

[187] Sergio Rui Silva, Sergio Cunha, Anibal Matos, Nuno Cruz, "An Algebraic Approach to Synthetic Aperture Sonar Image Reconstruction", *Oceans 2008*,Quebec City, Quebec, Canada, September 2008, pp. 1-7.

[188] Christophe Sintes, Gerard Llort-Pujol, Jean-Marc Le Caillec, "Interferometer design for the Vernier method-Part I: phase unwrapping", *Subm. IEEE J. Inst. Meas.*, May 2011.

[189] Christophe Sintes, Gerard Llort-Pujol, Jean-Marc Le Caillec, "Vernier Interferometry performance analysis", *Subm. IEEE J. Ocean Eng*, September 2011.

[190] Christophe Sintes, Gerard Llort-Pujol, Didier Gueriot, "Coherent probabilistic Error Model for Interferometric Sidescan Sonar", *IEEE J. Ocean Eng*, vol. 35, no. 2, April 2010.

[191] Christophe Sintes, R. Garello, D. Guerio, "Interferometric signal denoised by wavelets", presented at Oceans 2006 – Asia Pacific, Singapore 2006, doi: 10.1109/OCEANS.2006.306986, pp 1-6.

[192] Christophe Sintes, *Deconvolution bathymetrique d'images sonar lateral par des methodes interferometriques et de traitement de l'image (Deconvolution of bathymetric sidescan sonar and interferometric methods of processing the image),* PhD Dissertation, Universite de Rennes I, France, November 2002.

[193] Christophe Sintes, "Interferometric Side Scan Sonar: A Tool For High Resolution Sea Floor Exploration", *Technical lessons learnt from the Ericka incident and other oil spills*, Brest 13-16 March 2002.

[194] Christophe Sintes, Bassel Solaiman, "Strategies for unwrapping multisensors interferometric side scan sonar phase", *Oceans 2000*, Providence RI, 2000, vol. 3, pp 2059-2065. doi: 10.1109/OCEANS.2000.882242.

[195] Christophe Sintes, Bassel Solaiman, "Side Scan Sonar and Interferometric Noise", *Oceans 1999*, Seattle, WA, September 1999.

[196] Kenneth Steiglitz, Bradley Dickinson, "Phase Unwrapping by Factorization", *IEEE Trans. Acoust. Speech Signal Proc.,* vol. ASSP-30, no. 6, December 1982.

[197] Laurence C. Smith, "Emerging Applications of Interferometric Synthetic Aperture Radar (InSAR) in Geomorphology and Hydrology", *Annals Assoc. Amer. Geographers*, vol. 93 (3), 2002, pp. 385-398.

[198] Bernard D. Steinberg, *Principles of Aperture and Array System Design Including Random and Adaptive Arrays* , New York: John Wiley &Sons Inc. 1976.

[199] Petra Stoica and Randolph Moses, " Spectral Analysis of Signals", Upper Saddle River, New Jersey: Pearson Prentice Hall 2005.

[200] Jinsong Tang, Chunhua Zhang, Shuqiu Li, Baoshen Sun, Jiyuan Liu, Jiang Xu, Yong Huang, Tao Lin, Shanhua Xue, Liying Li, Tianhao Cui, Haining Huang, Yu Li and Qihu Li, "Progress of Synthetic aperture sonar in China", *Acoustic Science & Technology*, vol. 25, no. 1, Japan, 2004, pp. 95 -99."

[201] Mitsuharu Tokunaga, "DTM Accuracy derived from interferometry SAR", *ACRS 1997*, Japan, 1997."

[202] Le Van Trung, Ho Tong Minh Dinh, Van Cong Quoc Anh, "Dem Generation Using Sar Interferometry Technique Based On Ers Sar Images", *26th ACRS 2005*, Hanoi, Vietnam , November 2005.

[203] Robert J. Urick , *Principles of Underwater Sound* (3rd Edition), Los Altos, CA: Peninsula Publishing 1983.

[204] R. van Vossen, B.A.J. Quesson, J.C. Sabel, "SAS Interferometry for Detection and classification", TNO report | TNO-DV 2008 A176 3 October 2008.

[205] L. Wang, A. Bellettini, R. Hollett, A. Tesei, M. Pinto, " InSAS'00: Interferometric SAS and INS aided SAS imaging", *Oceans 2001,* Honolulu, Hawaii, vol.1, 2001, pp. 179-187.

[206] Stephan Weiss, Robert W. Stewart, Wei Liu, "A Broadband Adaptive Beamformer in Subbands with Scaled Aperture", Proc. 36th ACSSC 2002, vol. 2, Monterey, California, November 2002, pp.1298-1302.

[207] Gorm Wendelboe, "Acoustical Identification of Sea-Mines (A Coherent Very High Frequency Sonar Model)", Ph.D. Dissertation, Technical University of Denmark, 29th March 2007.

[208] Wei Xu, Ian Cumming, "A Region-Growing Algorithm for InSAR Phase Unwrapping", *IEEE Trans. Geosci. Remote Sens.,* vol. 37, no. 1, January 1999, pp. 124-134.

[209] Wei Xu, Ee Chien Chang, Leong Keong Kwoh, Hock Lim Wang Cheng Alice Heng, "Phase unwrapping of SAR Interferogram with Multi-frequency or Multi-baseline"*, IEEE IGARSS 1994*, Aug 1994, vol. 2, February 2003, pp. 730-732.

[210] Wen Xu, "Signal Direction of arrival and amplitude estimation for multiple row bathymetric sidescan sonars", MSc. Dissertation, Woods Hole Oceanographic Institute, Woods Hole, MA, February 1998.

[211] Hailiang Yang, Jinsong Tang, Qihu Li, Xiaodong liu "A robust multiple-receiver Range-Doppler algorithm for synthetic aperture sonar imagery" *, Oceans 2007 Europe* , Aberdeen, Scotland, June 2007.

[212] Bryan A. Yocom "Optimum Passive Beamforming in Relation to Active-Passive Data Fusion"*,* ARLUT EE381K-14, Austin, TX, May 09, 2008

[213] Sang-Ho Yun, Howard Zebker, Paul Segall, Andrew Hooper, Michael Poland, "Interferogram formation in the presence of complex and large deformation" *,* Geophysical Research Lett., vol. 34, iss. 12, citeid 12305, June 2007.

[214] Howard A. Zebker and Yanping Lu, "Phase unwrapping algorithms for radar interferometry: residue-cut, least-squares, and synthesis algorithms", *J. Opt. Soc. Am. A*, vol. 15, no. 3, March 1998.

[215] Sen ZHANG, Jinsong TANG, Chen Ming, Sanwen ZHU, Hailiang Yang, "Image Autocoregistration and Interferogram Estimation Using Extended COMET-EXIP Method"*,* IEEE Trans. Geosci. Remote Sens., vol. 48, no. 12, December 2010, pp. 4204-4218.

[216] Sen ZHANG, Jinsong TANG, "A Robust Estimation Method of Interferometric Phase Based on Weighted Subspace Fitting"*, Proc. 2nd Int. CISP 2009,* vol. 1, Tianjin, China, October 2009, pp. 1-5.

[217] Sen ZHANG, Jinsong TANG, ZHU Sanwen, "Image Autocoregistration and Interferogram Estimation Using Matrix Fitting"*, Proc. 2008 ISCSCT,* vol. 1, Shanghi, China, December 2008, pp. 104-108.

Appendix

Appendix 1 Chen-Millero-Li Equation

The Speed of Sound in seawater.

$$c(S,T,P) = Cw(T,P) + A(T,P)S + B(T,P)S3/2 + D(T,P)S2 \quad (A.1.1)$$

Cw is the sound speed of pure water, A, B and D are the salinity related terms

$$\begin{aligned} Cw(T,P) = {} & (C_{00} + C_{01}T + C_{02}T^2 + C_{03}T^3 + C_{04}T^4 + C_{05}T^5) + \\ & (C_{10} + C_{11}T + C_{12}T^2 + C13T^3 + C14T^4)P + \\ & (C_{20} + C_{21}T + C_{22}T^2 + C23T^3 + C24T^4)P^2 + \\ & (C_{30} + C_{31}T + C_{32}T^2)P^3 \end{aligned} \quad (A.1.2)$$

$$\begin{aligned} A(T,P) = {} & (A_{00} + A_{01}T + A_{02}T^2 + A_{03}T^3 + A_{04}T^4) + \\ & (A_{10} + A_{11}T + A_{12}T^2 + A_{13}T^3 + A_{14}T^4)P + \\ & (A_{20} + A_{21}T + A_{22}T^2 + A_{23}T^3)P^2 + \\ & (A_{30} + A_{31}T + A_{32}T^2)P^3 \end{aligned} \quad (A.1.3)$$

$$B(T,P) = B_{00} + B_{01}T + (B_{10} + B_{11}T)P \quad (A.1.4)$$

$$D(T,P) = D_{00} + D_{10}P \quad (A.1.5)$$

T = temperature in degrees Celsius, S = salinity in Practical Salinity Units parts per thousand (ppt), P = pressure in bar kPa

Range of validity: temperature 0 to 40 °C, salinity 0 to 40 parts per thousand (ppt), pressure 0 to 1000 bar (Wong and Zhu, 1995).

Table 1.1 Chen-Millero-Li Equation Coefficients

Coefficients	Numerical values	Coefficients	Numerical values
C_{00}	1402.388	A_{02}	7.166E-5
C_{01}	5.03830	A_{03}	2.008E-6
C_{02}	-5.81090E-2	A_{04}	-3.21E-8
C_{03}	3.3432E-4	A_{10}	9.4742E-5
C_{04}	-1.47797E-6	A_{11}	-1.2583E-5
C_{05}	3.1419E-9	A_{12}	-6.4928E-8
C_{10}	0.153563	A_{13}	1.0515E-8
C_{11}	6.8999E-4	A_{14}	-2.0142E-10
C_{12}	-8.1829E-6	A_{20}	-3.9064E-7
C_{13}	1.3632E-7	A_{21}	9.1061E-9
C_{14}	-6.1260E-10	A_{22}	-1.6009E-10
C_{20}	3.1260E-5	A_{23}	7.994E-12
C_{21}	-1.7111E-6	A_{30}	1.100E-10
C_{22}	2.5986E-8	A_{31}	6.651E-12
C_{23}	-2.5353E-10	A_{32}	-3.391E-13
C_{24}	1.0415E-12	B_{00}	-1.922E-2
C_{30}	-9.7729E-9	B_{01}	-4.42E-5

C_{31}	3.8513E-10	B_{10}	7.3637E-5
C_{32}	-2.3654E-12	B_{11}	1.7950E-7
A_{00}	1.389	D_{00}	1.727E-3
A_{01}	-1.262E-2	D_{10}	-7.9836E-6

Attenuation The attenuation rate is usually expressed in decibels, but it is usually provided in nepers/m, so to convert to dB/km

$$\alpha_{(\mathrm{dB/km})} = [10^3 \times 10 \log \mathrm{e}]\alpha_{(\mathrm{nepers/m})} \quad \text{(A.1.6)}$$

$$\mathrm{dB\ loss} = 20\log \mathrm{e}^{\alpha_e R} = 8.686\alpha_e R \quad \text{(A.1.7)}$$

20log (*e*) = 8.686 is the conversion from nepers to dB where *e* is Napier's constant napier ≈ nepers**,** equal to (*e* = 2.718, ln *e* = 1), but it obtains the *e* from Euler. The attenuation loss per unit of range is

$$\alpha = \frac{\mathrm{dB\ loss}}{\mathrm{distance}} = \frac{8.686\alpha_e R}{R} = 8.686\alpha_e\ \mathrm{dB/m} \quad \text{(A.1.8)}$$

Appendix 2 Windowing

Here is a collection of common weighting function used throughout signal processing. The functions are then compared in the time domain and the frequency domain.

Boxcar
(rectangular)

$$W(n) = \frac{1}{\sqrt{N}} \tag{A.2.1}$$

The boxcar uses uniform weighting that drops off immediately causing very strong ripples at the edges known as Gibbs phenomenon.

Gaussian

$$W(n) = e^{-\frac{1}{2}\left(\frac{n-(N-1)/2}{\sigma(N-1)/2}\right)^2} \tag{A.2.2}$$

Hamming

$$W(n) = .54 - .46\cos\left(\frac{2\pi n}{N-1}\right) \tag{A.2.3}$$

In the frequency domain the Boxcar (blue) has a narrow main beam with very high uniform sidelobes. The Gaussian (green) has a wider main beam with uniform sidelobes that are down by –30 dB. The Hamming (red) is very close to the Gaussian with a slightly narrower main beam and slightly stronger sidelobes.

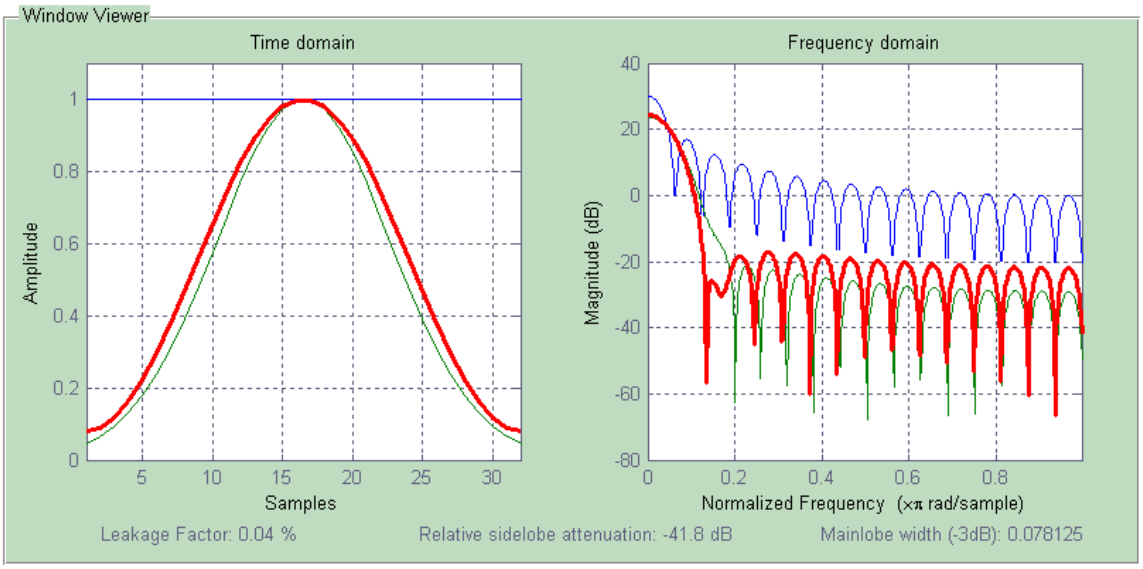

Figure A.2.1 Boxcar (blue), Gaussian (green), and Hamming (red).

Tukey

$$W(n) = \begin{pmatrix} 1 & 0 \le |n| \le \alpha\frac{N}{2} \\ \frac{1}{2}\left(1 + cos\left(\pi\frac{n - \alpha\frac{N}{2}}{2(1-\alpha)\frac{N}{2}}\right)\right) & \alpha\frac{N}{2} \le |n| \le N \end{pmatrix} \quad \text{(A.2.4)}$$

Blackman

$$W(n) = .42 - .5\cos\left(\frac{2\pi n}{N-1}\right) + .08cos\left(\frac{4\pi n}{N-1}\right) \quad \text{(A.2.5)}$$

Hann

$$W(n) = .5\cos\left(1 - cos\left(\frac{2\pi n}{N-1}\right)\right) \quad \text{(A.2.6)}$$

These three windows sidelobes are tappered. The Tukey (blue) window has inconsistant width sidelobes. The Blackman(green) windows has a wider central lobe with a loss in magnitude of the sidelobes. The Hann (red) window has a medium main lobes and even width sidelobes.

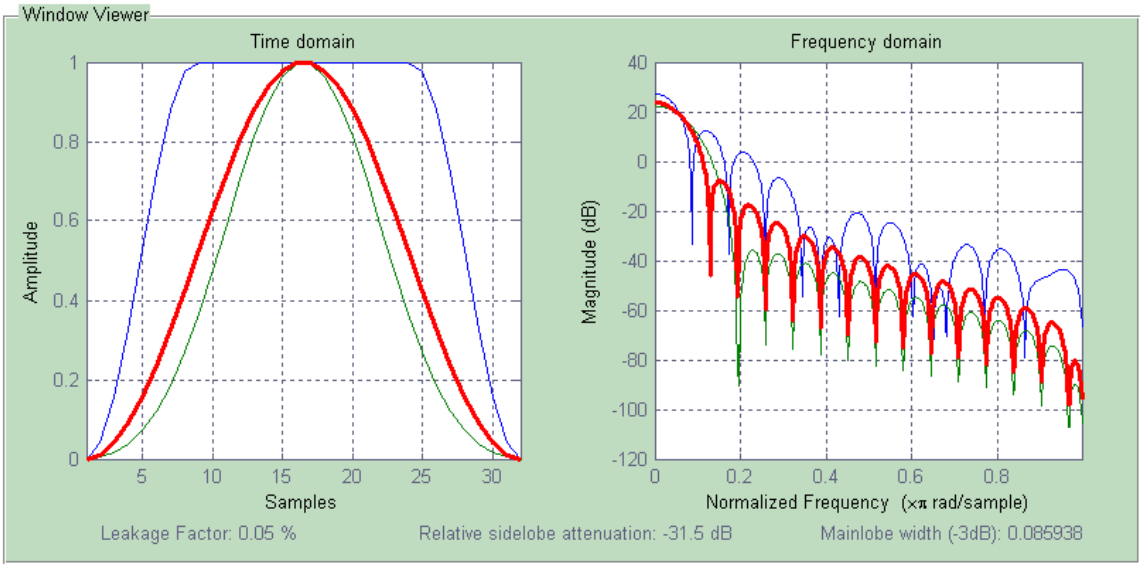

Figure A. 2.2 Tukey (blue), Blackman (green) , and Hann (red).

Dolph-Chebychev

$$W(k) = (-1)^k \left(\frac{cos\left[N\ cos^{-1}\left[\beta\ cos\left(\frac{\pi k}{N}\right)\right]\right]}{cosh[N\ cos^{-1}(\beta)]} \right) \tag{A.2.7}$$

Dolph-Chebychev is constructed in the frequency domain. It allows for the selection of the sidelobe magnitude for a given mainbeam width.

$$\beta = cos\left[\frac{1}{N\ cosh^{-1}(10^{\alpha})}\right] \tag{A.2.8}$$

α determines the sidelobe attenuation.

Kaiser

$$W(n) = \frac{I_0\left(\pi\alpha\sqrt{1-\left(\frac{2n}{N-1}-1\right)^2}\right)}{I_0\pi\alpha} \tag{A.2.9}$$

Kaiser uses Bessel functions I_0 is the zeroth order Bessel function, α determines the sidelobe attenuation .

Bartlett The coefficients for a Bartlett window are :

For N Odd

$$W(n) = \begin{cases} \frac{2n}{N} & 0 \le \mathrm{n} \le \frac{\mathrm{N}}{2} \\ 2 - \frac{2n}{N} & \frac{\mathrm{N}}{2} \le \mathrm{n} \le \mathrm{N} \end{cases} \tag{A.2.10}$$

For N even, L is the length of the window L=N+1

$$W(n) = \begin{cases} \frac{2n}{N} & 0 \le \mathrm{n} \le \frac{\mathrm{L}}{2} - 1 \\ 2 - \frac{2(N-n)}{N} & \frac{\mathrm{L}}{2} \le \mathrm{n} \le \mathrm{N} \end{cases} \tag{A.2.11}$$

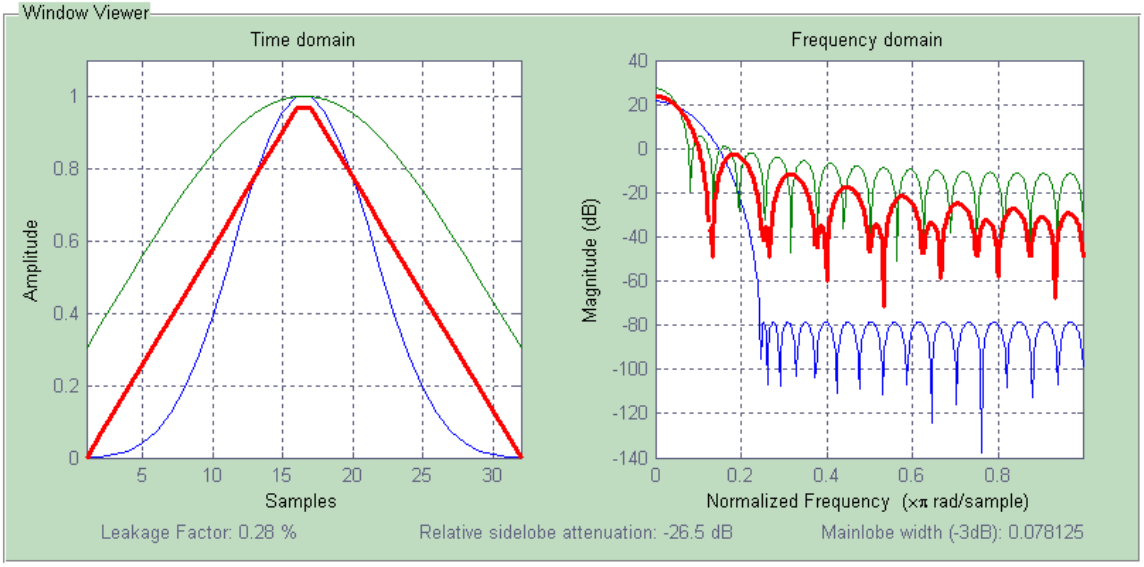

Figure A. 2.3 Chebychev (blue), Kaiser(green) , and Bartlet (red).

Butterworth

$$G(\omega) = \sqrt{\frac{1}{1+\omega^{2n}}} \tag{A.2.12}$$

Butterworth filters are used as high and low pass filters. They have the maximum flat top frequency response with a gentle roll off. ω is the normalized cutoff frequency at which the magnitude response of the filter is equal to $\frac{1}{\sqrt{2}}$ (approx. -3 dB), and n is the number of poles in the filter.

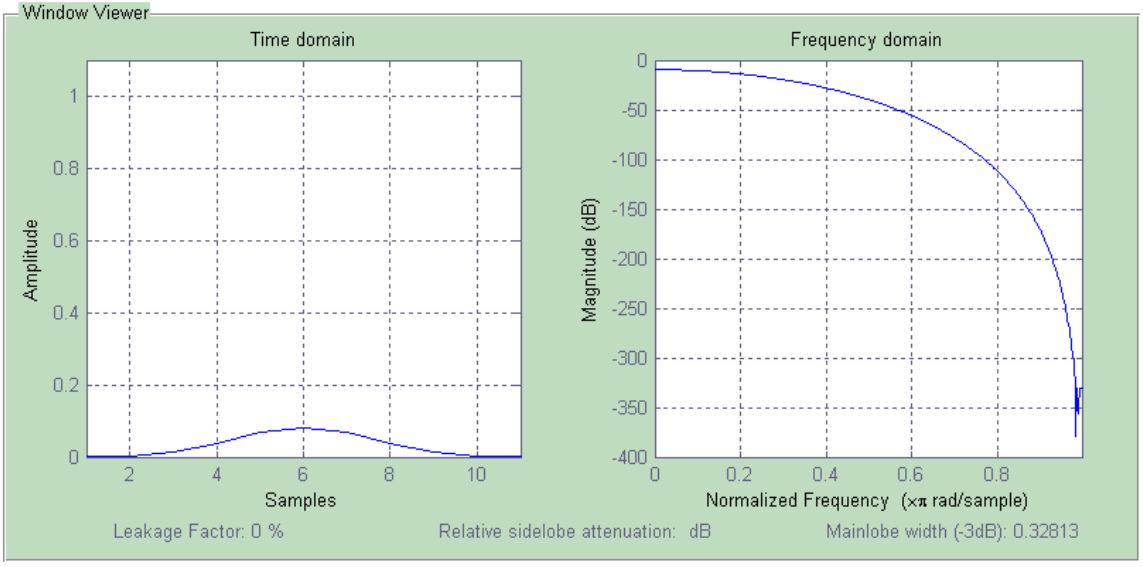

Figure A.2.4 Butterworth filter

Appendix 3 Basic Math

Total Derivatives

Consider a four-dimensional function

$$f(t,x,y,z) \tag{A.3.1}$$

The total derivative with respect to *t* is

$$\frac{df}{dt} = \frac{\partial f}{\partial t}\frac{dt}{dt} + \frac{\partial f}{\partial x}\frac{dx}{dt} + \frac{\partial f}{\partial y}\frac{dy}{dt} + \frac{\partial f}{\partial z}\frac{dz}{dt} \tag{A.3.2}$$

Multiply through by the time derivative

$$df = \frac{\partial f}{\partial t}dt + \frac{\partial f}{\partial x}dx + \frac{\partial f}{\partial y}dy + \frac{\partial f}{\partial z}dz \tag{A.3.3}$$

Integrate to get back to the original function

$$\int df = \int \frac{\partial f}{\partial t}dt + \int \frac{\partial f}{\partial x}dx + \int \frac{\partial f}{\partial y}dy + \int \frac{\partial f}{\partial z}dz \tag{A.3.4}$$

$$f = \int \frac{\partial f}{\partial t}dt + \int \frac{\partial f}{\partial x}dx + \int \frac{\partial f}{\partial y}dy + \int \frac{\partial f}{\partial z}dz \tag{A.3.5}$$

Taylor series expansion for square roots

$$\sqrt{1+x} \approx \sum_{n=0}^{\infty} \frac{-1^n 2n!}{(1-2n)n!^2\, 4^n} x^n = 1 + \frac{x}{2} - \frac{x^2}{8} + \frac{x^3}{16} + \cdots \tag{A.3.6}$$

Geometric series

$$\sum_{n=0}^{\infty} x^n = (1-x)^{-1} \qquad x < 1 \tag{A.3.7}$$

Maclaurin series for $(1- x)^{-n}$ for $|x| < 1$ which is the geometric series $1+x+x^2+x^3+\ldots..$ That can be approximated as

$$\sum_{n=0}^{n-1} x^n \approx \frac{1-x^n}{1-x} \tag{A.3.8}$$

Euler identity

$$\frac{e^{ix} - e^{-ix}}{i2} = sin(x) \tag{A.3.9}$$

$$sinc(x) = \frac{sin(\pi x)}{\pi x} \tag{A.3.10}$$

Appendix 4 Green's Theorem & H-K Integral

The development of the H-K integral is as follows. The source ensonifies the surface and each incremental area becomes a source of a Huygen's wavelet. The wavelets expand spherically and reach the point Q [Clay & Medwin 1977].

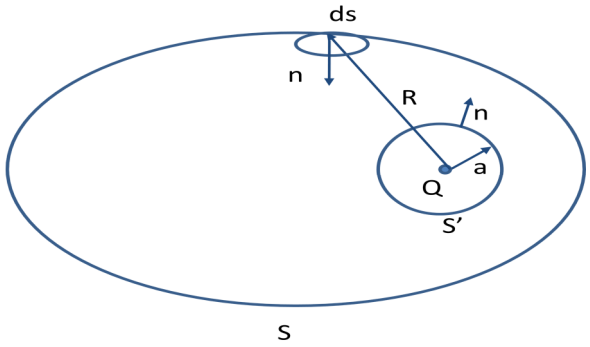

Figure A.4.5 The surface of the H-K integral: relates the wave field *U* on the scattering surface to the field *U(Q)* at a singularity at point *Q* for a surface enclosed by *S*, *S'* is a unit surface area that has a radius of *a* [Clay & Medwin 1977] .

The sound pressure at *Q* is the integral over all the wavelets.

$$\int_V \nabla \cdot F dv = \int_s F \cdot ds \tag{A.4.1}$$

F is the field vector and the divergence of the field is the net outward flux of energy from a source. *dv* is the incremental volume, and *ds* is the incremental area. Let *F* be the field and the field gradient

$$F_1 = U_1 \nabla U_2 \text{ and } F_2 = U_2 \nabla U_1 \tag{A.4.2}$$

U_1 and U_2 are arbitrary field vectors that are solutions to the wave equation. Replace *U* by its normal component

$$\nabla U \cdot ds = -\frac{\partial U}{\partial n}\left(\frac{x}{n}\cos\alpha + \frac{y}{n}\cos\beta + \frac{z}{n}\cos\gamma\right) ds = -\frac{\partial U}{\partial n}\left(\frac{x^2}{n^2} + \frac{y^2}{n^2} + \frac{z^2}{n^2}\right) = -\frac{\partial U}{\partial n} ds \tag{A.4.3}$$

Normal component

$$-\int_s U_1 \frac{\partial U_2}{\partial n} - U_2 \frac{\partial U_1}{\partial n} ds = \int_V (U_1 \nabla^2 U_2 - U_2 \nabla^2 U_1)\, dv \tag{A.4.4}$$

Consider the wave equation

$$\nabla^2 U(x,y,z) + \frac{\omega^2}{c^2}(x,y,z) = 0 \tag{A.4.5}$$

$$U_2 \nabla^2 U_1 = \frac{\omega^2}{c^2} U_2 U_1 \text{ and } U_1 \nabla^2 U_2 = \frac{\omega^2}{c^2} U_1 U_2 \tag{A.4.6}$$

Therefore

$$\int_V (U_1 \nabla^2 U_2 - U_2 \nabla^2 U_1)\, dv = 0 \tag{A.4.7}$$

$$-\int_s U_1 \frac{\partial U_2}{\partial n} - U_2 \frac{\partial U_1}{\partial n} ds = 0 \tag{A.4.8}$$

Let $U_2 = \frac{e^{-ikR}}{R}$

$$-\int_s U_1 \frac{\partial}{\partial n}\frac{e^{-ikR}}{R} - \frac{e^{-ikR}}{R}\frac{\partial U_1}{\partial n} ds = -\int_{s'} U_1 \frac{\partial}{\partial n}\frac{e^{-ika}}{a} - \frac{e^{-ika}}{a}\frac{\partial U_1}{\partial n} ds' \tag{A.4.9}$$

Evaluate the RHS by taking the limit at point Q as *a* goes to zero.

$$\lim_{a\to 0}\left\{-\int_0^{4\pi}\left[U_1 \frac{e^{-ika}}{a}\left(-ik - \frac{1}{a}\right) - \frac{e^{-ika}}{a}\frac{\partial U_1}{\partial a}\right] a^2 d\Omega\right\} = U(Q)\int_0^{4\pi} d\Omega = U(Q)4\pi \tag{A.4.10}$$

Therefore

$$U(Q) = \frac{1}{4\pi}\int_s U_1 \frac{\partial}{\partial n}\frac{e^{-ikR}}{R} - \frac{e^{-ikR}}{R}\frac{\partial U_1}{\partial n} ds \tag{A.4.11}$$

Appendix 5 Scattering Function

Given the pressure

$$P = \frac{R_{12} P_0 R_0}{R_1 + R_2} \tag{A.5.1}$$

P is pressure, R_{12} is the coherent reflection coefficient and is frequency dependent, $P_0 R_0$ is the pressure at 1 meter from the source. Root Mean Square (RMS) average coherent reflection coefficient is

$$\langle R_{12} \rangle = \langle P \rangle \frac{R_1 + R_2}{P_0 R_0} \tag{A.5.2}$$

The probability of occurrence of an elevation between ξ and $(\xi + \partial \xi)$ is $(w_a(\xi) \partial \xi)$ where $w_a(\xi)$ is the probability distribution function of the rough surface. The effect of ξ on the signal is to alter the phase by $(-2k \xi \cos \theta)$. The mean value of the coherent reflection coefficient is

$$\langle R_{12} \rangle = R_{12} \int_{-\infty}^{\infty} e^{-i2k\xi\cos\theta} w_a(\xi) d\xi \tag{A.5.3}$$

The equation is similar to the Fourier transform. The inverse of the transform is the probability distribution function. Therefore the distribution function can be calculated by taking a measurement of $\langle R_{12} \rangle$ over a wide range of frequencies.

$$[R_{12} w_a(\xi)] = \int_{-\infty}^{\infty} \langle R_{12} \rangle e^{-i2k\xi\cos\theta} d\left(\frac{2k\xi\cos\theta}{2\pi}\right) \tag{A.5.4}$$

$$w_a(\xi) = \frac{1}{\pi R_{12}} \int_{-\infty}^{\infty} \langle R_{12} \rangle e^{i2k\xi\cos\theta} dk\cos\theta \tag{A.5.5}$$

Assume the bottom has a Gaussian distribution and σ is the RMS roughness.

$$w_a(\xi) = \frac{1}{\sqrt{2\pi}\sigma} e^{-\frac{\xi^2}{2\sigma^2}} \tag{A.5.6}$$

The Coherent reflection coefficient for a surface having a Gaussian probability density function is

$$\langle R_{12} \rangle = R_{12} \frac{1}{\sqrt{2\pi}\sigma} \int_{-\infty}^{\infty} e^{-\frac{\xi^2}{2\sigma^2}} e^{-i2k\xi\cos\theta} d\xi \tag{A.5.7}$$

$$\langle R_{12} \rangle = R_{12} \frac{1}{\sqrt{2\pi}\sigma} \left\{ \int_{-\infty}^{\infty} e^{-\frac{\xi^2}{2\sigma^2}} \cos(2k\xi\cos\theta)\, d\xi - i \int_{-\infty}^{\infty} e^{-\frac{\xi^2}{2\sigma^2}} \sin(2k\xi\cos\theta)\, d\xi \right\} \tag{A.5.8}$$

This is an even function so the equation simplifies to

$$\langle R_{12} \rangle = R_{12} \frac{2}{\sqrt{2\pi}\sigma} \int_{0}^{\infty} e^{-\frac{\xi^2}{2\sigma^2}} \cos(2k\xi\cos\theta)\, d\xi \tag{A.5.9}$$

$$\langle R_{12} \rangle = R_{12} e^{-2k^2\sigma^2\cos^2\theta} \tag{A.5.10}$$

The scattering function *S* is a function of size shape orientation and frequency (see appendix) [Clay & Medwin 1977].

$$S(\theta_1, \phi_1, \theta_2, \phi_2, f) \tag{A.5.11}$$

The scattered pressure *P* is equal to the incident pressure P_i on the Area *A* times the scattering functions *S* divided by the range R_2 from the object to the receiver.

$$P^2 = P_i^2 \frac{A(\theta_1, \phi_1)}{R_2^2} S(\theta_1, \phi_1, \theta_2, \phi_2, f) \tag{A.5.12}$$

The incident pressure is the RMS pressure at range.

$$P_i^2 = \frac{R_0^2 P_0^2}{R_1^2} \tag{A.5.13}$$

R_1 is the range from the source to the scatter, and P_0 R_0 is the pressure at 1 meter from the source. Integrate over the duration of the signal pulse.

$$\int_{T_2} P^2\,dt = R_0^2 \int_{T_1} P_0^2\,dt \frac{A(\theta_1,\phi_1)}{R_1^2 R_2^2} S(\theta_1,\phi_1,\theta_2,\phi_2,f) \tag{A.5.14}$$

T_1 is the duration of the incident signal, and T_2 is the duration of all arrivals from area A.

$$A = \frac{\pi \Delta x \Delta \varphi R_1^2}{\cos\theta} \tag{A.5.15}$$

Area A is an ellipse with axis a = $R_1\Delta x$ and axis b = $R_1\Delta\varphi$, R1 is range, and θ is the angle of incidents. For backscatter $R_1 = R_2 = R$

$$\int_{T_2} P^2\,dt = R_0^2 \int_{T_1} P_0^2\,dt \frac{A}{R^4} S(\theta_1,\phi_1,\theta_2,\phi_2,f) \tag{A.5.16}$$

Solve for the scattering function

$$S(\theta_1,\phi_1,\theta_2,\phi_2,f) = \frac{\int_{T_2} P^2\,dt}{R_0^2 \int_{T_1} P_0^2\,dt} \frac{R^4}{A} \tag{A.5.17}$$

P incident pressure, R is range, P_0R_0 is the reference pressure at 1 meter range, and A is the area.

Appendix 6 Principle of Stationary Phase

$$\varphi_{(u)} = -2k\sqrt{x^2 + (y-u)^2} - k_u u \tag{A.6.1}$$

The first derivative of the phase is

$$\varphi'_{(u)} = \frac{2k(y-u)}{\sqrt{x^2 + (y-u)^2}} - k_u \tag{A.6.2}$$

Solve for the stationary point where the first derivative is equal to zero $\varphi'_{(u^*)} = 0$.

$$u^* = y - \frac{k_u^2 x^2}{\sqrt{4k^2 - k_u^2 x}} \tag{A.6.3}$$

Substitute u^* into $\varphi_{(u^*)}$ to obtain the phase transform

$$\varphi_{(u^*)} = -2k\sqrt{x^2 + (y-u^*)^2} - k_u u^* \tag{A.6.4}$$

$$\varphi_{(u^*)} = -\sqrt{4k^2 - k_u^2}x - k_u y \tag{A.6.5}$$

Use the quotient rule to obtain the second derivative of the phase

$$\varphi''_{(u)} = -\frac{2kx^2}{(x^2 + (y-u)^2)^{\frac{3}{2}}} \tag{A.6.6}$$

The second derivative is used to scale the amplitude to k space

$$A = \sqrt{-\frac{i2\pi}{\varphi''_{(u^*)}}} \tag{A.6.7}$$

$$A = \sqrt{-\frac{8\pi k^2 x}{i(4k^2 - k_u^2)^{\frac{3}{2}}}} \tag{A.6.8}$$

$$A \approx \sqrt{\frac{\pi x}{ik}} \tag{A.6.9}$$

Appendix 7 Matrix Inversion Lemma

Let **A** and **B** be two positive *m x m* matrices related by

$$\boldsymbol{A} = \boldsymbol{B}^{-1} + \boldsymbol{C}\boldsymbol{D}^{-1}\boldsymbol{C}^{H} \tag{A.7.1}$$

Where **D** is a positive definite *n x m* matrix and **C** is an *m x n* matrix. According to the matrix inversion lemma, if there is a matrix **A**, its inverse is

$$\boldsymbol{A}^{-1} = \boldsymbol{B} - \boldsymbol{B}\boldsymbol{C}(\boldsymbol{D}+\boldsymbol{C}^{H}\boldsymbol{B}\boldsymbol{C})^{-1}\boldsymbol{C}^{H}\boldsymbol{B} \tag{A.7.2}$$

It applies to the equations above as follows

$$\boldsymbol{A} = \boldsymbol{\Phi}_{n} \tag{A.7.3}$$

$$\boldsymbol{B}^{-1} = \lambda\boldsymbol{\Phi}_{n-1} \tag{A.7.4}$$

$$\boldsymbol{C} = x_{n} \tag{A.7.5}$$

$$\boldsymbol{D} = 1 \tag{A.7.6}$$

$$\boldsymbol{\Phi}_{\mathrm{n}}^{-1} = \lambda\boldsymbol{\Phi}_{\mathrm{n-1}}^{-1} - \frac{\lambda^{-2}\boldsymbol{\Phi}_{\mathrm{n-1}}^{-1}x_{n}x_{\mathrm{n}}^{\mathrm{H}}\boldsymbol{\Phi}_{\mathrm{n-1}}^{-1}}{1+\lambda^{-1}x_{\mathrm{n}}^{\mathrm{H}}\boldsymbol{\Phi}_{\mathrm{n-1}}^{-1}x_{n}} \tag{A.7.7}$$

Appendix 8 Range-Doppler Algorithm

Developed by J. MacDonald and W. Dettwiler in 1978 and expanded on by C. Wu in 1982 at Joint Propulsion Laboratory (JPL) for spaceborn SAR. A basebanded, range compressed signal is transformed to the range-Doppler domain by an azimuth FFT. A range cell migration correction is applied. Azimuth filtering or secondary range compression followed by an IFFT to form the image [Soumekh 1999].

Range-Doppler inversion scheme

$$fF(x,k_y) = W(k_y)qQ(x,k_y)\,\mathcal{F}_u\{\,sS_b(t,k_u)\} \tag{A.8.1}$$

$W(k_y)$ is the window function (see appendix A2), $qQ(x, k_y)$ is the along-track compression, F_u is the coordinate transformation into the spatial Doppler wavenumber domain.

$$sS_b(t,k_u) = \mathcal{F}_u\{ss_b(t,u)\}$$

$$sS_b(t,k_u) = \mathcal{F}_u\{ss_b(t,u)\} \tag{A.8.2}$$

The coordinate transform is

$$x(t,k_u) \equiv \frac{c}{2}t[1 - C(k_u)] \tag{A.8.3}$$

$$k_y(t,k_u) \equiv k_u \tag{A.8.4}$$

The curvature factor is

$$C_s(k_u) = \frac{1}{\sqrt{1-\left(\frac{k_u}{2k_0}\right)^2}} - 1 \tag{A.8.5}$$

$$C_s(k_u) \approx \frac{1}{2}\left(\frac{k_u}{2k_0}\right)^2 \tag{A.8.6}$$

two-dimensional along-track compression phase only

$$qQ(x,k_y)=\sqrt{4k_0^2-k_y^2}\,e^{-i\left(\sqrt{4k_0^2-k_y^2}-2k_0\right)x_0}\approx\sqrt{4k_0^2-k_y^2}\,e^{-i\frac{k_y^2}{4k_0}x_0} \tag{A.8.7}$$

The PSF necessary for focusing

$$pp(t,k_u,x)=\delta\left[t-\frac{2}{c}\Delta R(u,x_0)\right]e^{-i\left(\sqrt{4k_0^2-k_u^2}x-2k\right)x_0} \tag{A.8.8}$$

$$pp(t,k_u,x_0)\approx\delta\left[t-\frac{x_0}{c}\left(\frac{k_u}{2k_0}\right)^2\right]e^{-i\frac{k_u^2}{4k_0}x_0} \tag{A.8.9}$$

Range migration locus in the range-Doppler domain for a target at x_0

$$\Delta R(k_u,x_0)=x_0C_s(k_u) \tag{A.8.10}$$

The target at range x_0 scribes out a locus in the time Doppler matrix given by

$$t(k_u,x_0)=\frac{2}{c}x_0[1+C_s(k_u)] \tag{A.8.11}$$

The final image estimate is

$$\left|ff_b(x,k_y)\right|=\left|F_{ky}^{-1}\{fF_b(x,k_y)\}\right| \tag{A.8.12}$$

$$\left|ff_b(x,k_y)\right|=\left|sinc\left(\frac{2B_c}{c}x\right)sinc\left(\frac{2}{D}y\right)ff(x,y)\right| \tag{A.8.13}$$

Appendix 9 Raney's Range-Doppler signal

Raney showed that it was possible to obtain the required range-Doppler signal without using Stolt mapping or pulse compression. The basebanded return signal from a point target at x_0 and K_c is the chirp rate [Hawkins 1996].

$$ee_{\delta}(t,u)$$
$$= a\left(t-\frac{2}{c}\sqrt{x_0^2+u^2},x_0,-u\right)rect\left(\frac{t-\frac{2}{c}\sqrt{x_0^2+u^2}}{\tau_c}\right)e^{i\pi K_c\left(t-\frac{2}{c}\sqrt{x_0^2+u^2}\right)^2}e^{-i2k_0\sqrt{x_0^2+u^2}} \quad \text{(A.9.1)}$$

The Phase is

$$\varphi(t)=\pi K_c\left(t-\frac{2}{c}\sqrt{x_0^2+u^2}\right)^2-\omega_b t \quad \text{(A.9.2)}$$

The first derivative of the phase

$$\varphi'(t)=2\pi K_c\left(t-\frac{2}{c}\sqrt{x_0^2+u^2}\right)-\omega_b \quad \text{(A.9.3)}$$

The second derivative of the phase

$$\varphi''(t)=2\pi K_c \quad \text{(A.9.4)}$$

The stationary point is

$$t^*=\frac{\omega_b}{2\pi K_c}+\frac{2}{c}\sqrt{x_0^2+u^2} \quad \text{(A.9.5)}$$

The complex constant

$$A_1=\sqrt{\frac{i}{K_c}} \quad \text{(A.9.6)}$$

The transform phase is

$$\psi(\omega_b) \equiv \varphi(t^*) = \frac{\omega_b^2}{4\pi K_c} - 2k_b\sqrt{x_0^2 + u^2} \tag{A.9.7}$$

The temporal transform of the returned echo is

$$Ee_\delta(\omega_b) = \sqrt{\frac{i}{K_c}} A(\omega, x, -u) rect\left(\frac{\omega_b}{2\pi K_c \tau_c}\right) e^{i\frac{\omega_b{}^2}{4\pi K_c} - i2k\sqrt{x_0^2+u^2}} \tag{A.9.8}$$

Transform into the spatial domain

$$EE_\delta(\omega_b, k_u) = \sqrt{\frac{x\pi}{kK_c}} A(k_u) rect\left(\frac{\omega_b}{2\pi K_c \tau_c}\right) e^{i\frac{\omega_b{}^2}{4\pi K_c} - i\sqrt{4k^2-k_u^2}x_0} \tag{A.9.9}$$

Expansion of the phase term

$$\sqrt{4k^2 - k_u^2} = \sqrt{4(k_0^2 + 2k_0k_b + k_b^2) - k_u^2} \tag{A.9.10}$$

$$\sqrt{4k^2 - k_u^2} = 2k_0\sqrt{\left[\left(1 - \frac{k_u^2}{4k_0^2}\right) + \left(\frac{2k_b}{k_0} + \frac{k_b^2}{k_0^2}\right)\right]} \tag{A.9.11}$$

$$\sqrt{4k^2 - k_u^2} = 2k_0\left(1 - \frac{k_u^2}{4k_0^2}\right)^{\frac{1}{2}}\left[1 + \frac{\left(\frac{2k_b}{k_0} + \frac{k_b^2}{k_0^2}\right)}{\left(1 - \frac{k_u^2}{4k_0^2}\right)}\right]^{\frac{1}{2}} \tag{A.9.12}$$

$$\beta = \sqrt{1 - \frac{k_u^2}{4k_0^2}} \tag{A.9.13}$$

Using a Taylor Series Approximation the equation becomes

$$\sqrt{4k^2 - k_u^2} \approx 2k_0\beta\left[1 + \frac{1}{2\beta^2}\left(\frac{2k_b}{k_0} + \frac{k_b^2}{k_0^2}\right) - \frac{1}{8\beta^4}\left(\frac{2k_b}{k_0}\right)^2\right] \tag{A.9.14}$$

$$\sqrt{4k^2 - k_u^2} = 2k_0\beta + \frac{2k_0\beta}{2\beta^2}\left(\frac{2k_b}{k_0} + \frac{k_b^2}{k_0^2}\right) - \frac{2k_0\beta}{8\beta^4}\frac{4k_b^2}{k_0^2} \tag{A.9.15}$$

$$\sqrt{4k^2 - k_u^2} = 2k_0\beta + \frac{2k_b}{\beta} + \frac{k_b^2}{k_0\beta} - \frac{k_b^2}{k_0\beta^3} \tag{A.9.16}$$

$$\sqrt{4k^2 - k_u^2} = \frac{2\omega_0\beta}{c} + \frac{2\omega_b}{c\beta} + \frac{\omega_b^2}{\omega_0 c\beta} - \frac{\omega_b^2}{\omega_0 c\beta^3} \tag{A.9.17}$$

The phase function is

$$\varphi(\omega_b) = -\frac{\omega_b^2}{4\pi K_c} - \sqrt{4k^2 - k_u^2}x + \omega_b t \tag{A.9. 18}$$

$$\varphi(\omega_b) = -\frac{\omega_b^2}{4\pi K_c} - x\left(\frac{2\omega_0\beta}{c} + \frac{2\omega_b}{c\beta} + \frac{\omega_b^2}{\omega_0 c\beta} - \frac{\omega_b^2}{\omega_0 c\beta^3}\right) + \omega_b t \tag{A.9.19}$$

$$\varphi(\omega_b) = \omega_b^2\left(-\frac{1}{4\pi K_c} - \frac{x}{\omega_0 c\beta} + \frac{x}{\omega_0 c\beta^3}\right) + \omega_b\left(t - \frac{2x}{c\beta}\right) - \frac{2\omega_0 x\beta}{c} \tag{A.9.20}$$

This is a quadratic approximation to Stolt mapping of the wavenumber algorithm.

The stationary point of the phase function is

$$\omega_b^* = \frac{\left(t - \frac{2x}{c\beta}\right)}{\left[\frac{1}{4\pi K_c} + \frac{x}{\omega_0 c}\left(\frac{\beta^2 - 1}{\beta^3}\right)\right]} \tag{A.9.21}$$

Range-Doppler phase is

$$\psi(\omega_b) \equiv \varphi(c) = \frac{1}{4\left[\frac{1}{4\pi K_c} + \frac{x}{\omega_0 c}\left(\frac{\beta^2-1}{\beta^3}\right)\right]}\left(t - \frac{2x}{c\beta}\right)^2 - \frac{2\omega_0 x\beta}{c} \tag{A.9.22}$$

$$\psi(\omega_b) = \pi K_s(k_u; x)\left[t - \frac{2}{c}R_s(k_u; x)\right]^2 - \sqrt{\left(4k_0^2 - {k_u}^2\right)}\, x \tag{A.9.23}$$

$$R_s(k_u; x) = \frac{x}{\sqrt{1 - \left(\frac{k_u}{2k_0}\right)^2}} = x[1 + C_s(k_u)] \tag{A.9.24}$$

The Curvature factor is

$$C_s(k_u) = \frac{1}{\sqrt{1 - \left(\frac{k_u}{2k_0}\right)^2}} - 1 \tag{A.9.25}$$

The new k_u dependent chirp

$$K_s(k_u; x) = \frac{1}{\frac{1}{K_c - K_{src}(k_u; x)}} \tag{A.9.26}$$

Range dependent chirp term

$$K_{src}(k_u; x) = \frac{8\pi x}{c^2}\frac{k_u^2}{(4k_0^2 - k_u^2)^{\frac{3}{2}}} \tag{A.9.27}$$

$$\varphi''(\omega_b^*) = -2\left(\frac{1}{4\pi K_c} + \frac{x}{\omega_0 c\beta} - \frac{x}{\omega_0 c\beta^3}\right) \tag{A.9.28}$$

$$A_3 = \frac{1}{2\pi}\sqrt{\frac{-i2\pi}{2\left(\frac{1}{4\pi K_c} + \frac{x}{\omega_0 c\beta} - \frac{x}{\omega_0 c\beta^3}\right)}} \approx \sqrt{\frac{K_c}{i}} \tag{A.9.29}$$

Raney Range-Doppler signal

$$eE_{\delta}(t,k_u) = \sqrt{\frac{x\pi}{ik_0}} A(k_u)\, rect\left[t - \frac{2}{c} R_s(k_u;x)\right] e^{i\pi K_s(k_u;x)\left[t-\frac{2}{c}R_s(k_u;x)\right]^2} e^{-i\sqrt{4k_0^2-k_u^2}x_0} \qquad \text{(A.9.30)}$$

Vita

Patricia Giardina (Rosser-Stiede) was born on Long Island New York in 1965. In 1985 she joined the United States Navy as an Ocean systems Technician with duty stations in Adak Alaska, Dam Neck Virginia and Norfolk Virginia. In 1993 she went to work at NASA Langley in the Fluid Mechanics and Acoustics Division in Hampton Virginia. In 1995 she graduated with a B.S. in Physics from Old Dominion University in Norfolk, Virginia. In 1996 went to work for the Naval Oceanographic Office, at Stennis Space Center Mississippi. In 2001 obtained her Masters Degree in Hydrography from the University of Southern Mississippi. In 2008 went to work for Naval Sea Systems Command in Panama City, Florida to conduct her dissertation research. In 2012 received her second Masters degree in Physics. In 2012 she received her Doctorate of Philosophy from the University of New Orleans in Engineering and Applied Science with a concentration in Underwater Acoustics.